PADERBORN UNIVERSITY
Faculty of Science
Department of Physics
Theoretical Quantum Optics
J.-Prof. Dr. Polina Sharapova

MACQUARIE University
Faculty of Science and Engineering
Department of Physics and Astronomy
Integrated Nonlinear Quantum Photonics
Prof. Dr. Michael Steel

Orbital Angular Momentum of Counterpropagating Photon Pairs in Periodic Waveguides

Master's Thesis

by

Elisabeth Wagner

Submitted to:

J.-Prof. Dr. Polina Sharapova and Prof. Dr. Torsten Meier

Paderborn, November 12, 2018

Contents

1 Motivation

Quantum information science has seen an explosion of interest worldwide [1]. Encompassing recent scientific achievements in quantum communication [2], quantum cryptography [3], quantum teleportation [4, 5], quantum computation [6] and other areas, a future of new information technology may be predicted.

To date, nearly all realisations and experiments in the fields just mentioned have been performed with two-level quantum systems (qubits). However, notwithstanding technological challenges [7], discrete higher-dimensional quantum systems (qudits) arouse attention because the associated information content a single quantum carrier can transmit is enlarged in comparison to qubits. In addition to the higher information capacity, qudits benefit from an increased error threshold in quantum (optimal) cloning: it is more difficult for an eavesdropper to hack a high-dimensional key distribution scheme than a key in two dimensions [8–10]. Another active field of research is high-dimensional quantum computation where the distillation of magic states [11, 12] and the circuit structure of the Shor algorithm [13] are improved in comparison to the two-dimensional case.

A promising possibility to store high-dimensional quantum information are photons that are entangled in their orbital angular momenta (OAM). They can transmit a theoretically unlimited amount of information at the same time since the OAM offers an unbounded basis in quantum mechanics [14–18]. Of particular interest are waveguided modes regarding a possible implementation in the present fibre-optic communication system [19]. They take advantage over modes in free-space as they are characterised by spatial confinement and higher power handling capacity [20].

In this thesis, we study the creation of higher-order OAM modes using a helical grating structure in a cylindrical core-cladding waveguide; the generation of entangled counterpropagating OAM modes is described by a four-wave-mixing process. Sec. 3.1 expounds the mode-coupling process in the waveguide: the coupled mode equations are derived for transmission and reflection gratings and the corresponding transmission and reflection spectra are shown. To estimate the modal coupling strength the coupling constants are investigated analytically and numerically. In Sec. 3.2 we describe the non-linear four-wave-mixing process in a periodic waveguide leading to the generation of counterpropagating photon pairs that are entangled in OAM *and* the direction of propagation. The entangled state is derived in the quantum-mechanical approach and the difference between the central frequencies of the generated and the pump photons is estimated. We present the two-photon amplitude for different output modes and discuss the influence of the grating's modulation strength. The last calculation reveals the average number of generated photon pairs per pump pulse. Under the assumption of non-degenerate pumps the signal and idler modes are phase matched by the use of two helical grating structures with different periodic lengths.

The first part of the thesis has grown out of a collaboration with the research group of Prof. Dr. Michael Steel at the Macquarie University in Sydney/Australia where I have had a research stay for five months. During the second part of the research project I have been supervised by J.-Prof. Polina Sharapova at the University of Paderborn in Germany.

2 Fundamentals

To theoretically investigate the waveguided OAM modes, the underlying mathematical and physical essentials are expounded. We start with the description of the waveguide geometry and a brief derivation of the corresponding electromagnetic modes in Sec. 2.1. How these modes can be transformed into OAM modes is described in Sec. 2.2. Subsequently in Sec. 2.3, grating structures are introduced into the waveguide leading to the conversion of co- and counterpropagating modes. For the production of entangled modes, the non-linear four-wave-mixing process is expounded in Sec. 2.4.

2.1 Cylindrical dielectric waveguides

We mainly focus on the presented in Fig. 2.1 cylindrical-shaped waveguide without any losses. It consists of a guiding *core* and a surrounding *cladding* with respective dielectric constants $\varepsilon_{\mathrm{co}}$ and $\varepsilon_{\mathrm{cl}}$.

Waveguiding is only possible in regions where the dielectric constant is higher than the surrounding. Therefore $\varepsilon_{\mathrm{co}} > \varepsilon_{\mathrm{cl}}$ is chosen. The core has radius a while the cladding is assumed to have infinite extent because the fields decay near-exponentially in the cladding [21]. The rotational symmetry of the geometrical object suggests the use of cylindrical coordinates $\mathbf{r} = (r, \phi, z)$.

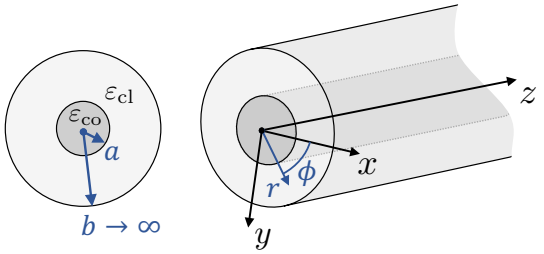

Fig. 2.1 Sketch of a step-index waveguide. Left: transverse profile. Right: three-dimensional structure in a Cartesian and a cylindrical coordinate system

The electric field $\mathbf{E}$ and the magnetic field $\mathbf{H}$ in the waveguide can be derived from Maxwell's equations. The latter yield the scalar wave equation[1]

$$\left[\boldsymbol{\nabla}^2 - \frac{\bar{\varepsilon}(r)}{c^2}\frac{\partial^2}{\partial t^2}\right]\mathbf{E}(\mathbf{r}, t) = 0, \tag{2.1}$$

[1] It holds under the assumption of a linear dielectric, nonmagnetic medium without free charges or currents and only small variations of the dielectric constant $\varepsilon(\mathbf{r})$, such that $\boldsymbol{\nabla} \cdot (\varepsilon(\mathbf{r})\,\mathbf{E}(\mathbf{r}, t)) \approx \varepsilon(\mathbf{r})\,\boldsymbol{\nabla} \cdot \mathbf{E}(\mathbf{r}, t)$, where $\boldsymbol{\nabla}\cdot$ is the divergence operator. However, as discussed by [22], the factor $\boldsymbol{\nabla}\varepsilon(\mathbf{r})$ is actually not negligible. To obtain accurate solutions, one would require to use the full vector wave equation

$$\boldsymbol{\nabla} \times (\boldsymbol{\nabla} \times \mathbf{E}(\mathbf{r}, t)) - \frac{\bar{\varepsilon}(r)}{c^2}\frac{\partial^2}{\partial t^2}\mathbf{E}(\mathbf{r}, t) = 0,$$

where $\boldsymbol{\nabla}\times$ denotes the curl operator. That leads to additional terms $\boldsymbol{\nabla}\ln(\bar{\varepsilon}(r))$ which are not zero at the core-cladding interface. In a step-index waveguide it is nevertheless possible to solve the wave equation in each constant part of the cross-section separately, without directly confronting the inhomogeneity. The solutions are then connected with boundary conditions at the core-cladding transition. The exact solutions are obtained. (Equivalent equations hold for the magnetic field $\mathbf{H}$.) [23]

where $\boldsymbol{\nabla}^2$ is the Laplacian operator in cylindrical coordinates and $\frac{\partial}{\partial \xi}$ denotes a partial derivation with respect to variable ξ, i.e. time t in this case. c is the speed of light in vacuum and $\bar{\varepsilon}(r)$ represents the radial step-index profile of the dielectric constant:

$$\bar{\varepsilon}(r) = \begin{cases} \varepsilon_{\mathrm{co}} = n_{\mathrm{co}}^2 & \text{, if } r \leq a \\ \varepsilon_{\mathrm{cl}} = n_{\mathrm{cl}}^2 & \text{, if } r > a \end{cases}. \tag{2.2}$$

n_{co} and n_{cl} are the corresponding refractive indices in the core or the cladding of the waveguide.

The field solution is separable into a (vectorial) transverse profile $\mathbf{f}(r, \phi)$ that propagates in z-direction with propagation constant $\beta \in \mathbb{R}$ and oscillates in time with angular frequency ω:

$$\mathbf{E}(\mathbf{r}, t) = \mathbf{f}(r, \phi)\, e^{i(\beta z - \omega t)} + \text{c.c.}. \tag{2.3}$$

c.c. labels the complex conjugated field. $\mathbf{f}(r, \phi)$ satisfies according to Eq. (2.1) the condition

$$\left[\frac{\partial^2}{\partial r^2} + \frac{1}{r}\frac{\partial}{\partial r} + \frac{1}{r^2}\frac{\partial^2}{\partial \phi^2} + \left(k^2 \bar{\varepsilon}(r) - \beta^2 \right) \right] \mathbf{f}(r, \phi) = 0, \tag{2.4}$$

with the wavenumber in vacuum $k = \frac{\omega}{c}$. To solve this differential equation, $\mathbf{f}(r, \phi)$ is separated into a radial factor $\mathbf{e}(r)$ and an oscillating angular factor $\mathbf{g}(\phi)$. We write

$$\mathbf{f}(r, \phi) = \mathbf{e}(r) \circ \mathbf{g}(\phi), \tag{2.5}$$

where $\circ$ denotes the Hadamard product, i.e. componentwise vector multiplication.[2] Following this path, Bessel's differential equation is recovered with argument $(\sqrt{k^2 \bar{\varepsilon}(r) - \beta^2}\, r)$, where $k^2 \varepsilon_{\mathrm{cl}} < \beta^2 < k^2 \varepsilon_{\mathrm{co}}$ must hold for guided waves [24]. The resultant arguments are real in the waveguide core and imaginary in the cladding:

$$u\, r = \sqrt{k^2 \varepsilon_{\mathrm{co}} - \beta^2}\; r \quad \text{for } r < a, \tag{2.6a}$$

$$i\, w\, r = i \sqrt{\beta^2 - k^2 \varepsilon_{\mathrm{cl}}}\; r \quad \text{for } r > a. \tag{2.6b}$$

u is the lateral wavenumber and w the lateral attenuation constant, where both $u, w \in \mathbb{R}$ [25]. The geometrical sum of the normalised parameters $U = ua$ and $W = wa$,

$$V = \sqrt{U^2 + W^2} = ka \sqrt{\varepsilon_{\mathrm{co}} - \varepsilon_{\mathrm{cl}}} = \frac{2\pi a}{\lambda} \sqrt{\varepsilon_{\mathrm{co}} - \varepsilon_{\mathrm{cl}}}, \tag{2.7}$$

is the normalised frequency.[3] It depends only on the vacuum wavelength $\lambda = \frac{2\pi c}{\omega}$ and waveguide parameters $\varepsilon_{\mathrm{co}}$, $\varepsilon_{\mathrm{cl}}$ and a. The physical field solution of Bessel's differential equation (with the arguments in Eq. (2.6)) has to be constructed of Bessel functions of the first kind, $J_m(ur)$, and modified Bessel functions of the second kind, $K_m(wr)$, both of order $m \in \mathbb{N}_0$, in the waveguide core or its cladding, respectively.[4]

[2] In practice, Eq. (2.4) needs to be solved for merely one field component. The other elements are connected via Maxwell's equations.

[3] Though V is unitless, the notation of "normalised frequency" is commonly used to highlight the proportionality of V on the angular frequency $\omega = \frac{2\pi c}{\lambda}$.

[4] The ordinary Bessel function of the second kind, $Y_m(ur)$, is no part of the field solution since it diverges at the origin. Analogously, the modified Bessel functions of the first kind, $I_m(wr)$, diverges for $r \to \infty$, which would be an unphysical solution in a waveguide cladding with the supposed infinite extent.

Using this ansatz boundary conditions lead to the equation

$$\varepsilon_{\mathrm{co}}\frac{J_m'(U)}{UJ_m(U)}+\frac{\varepsilon_{\mathrm{co}}+\varepsilon_{\mathrm{cl}}}{2}\frac{K_m'(W)}{WK_m(W)} = \pm\left[\left(\frac{\varepsilon_{\mathrm{co}}+\varepsilon_{\mathrm{cl}}}{2}\frac{K_m'(W)}{WK_m(W)}\right)^2+m^2\,\varepsilon_{\mathrm{co}}\left(\frac{1}{U^2}+\frac{1}{W^2}\right)\left(\frac{\varepsilon_{\mathrm{co}}}{U^2}+\frac{\varepsilon_{\mathrm{cl}}}{W^2}\right)\right]^{\frac{1}{2}} \tag{2.8}$$

which is analytically not solvable [21]. Recognising the arising "±" sign one could predict the existence of at least two possible solutions at first glance. The upper prime signs $'$ of the Bessel functions denote a derivation, unitlessly given by

$$J_m'(U)=J_m'(ua)=\frac{\partial J_m(ur)}{\partial(ur)}\bigg|_{r=a}=\frac{1}{u}\frac{\partial J_m(ur)}{\partial r}\bigg|_{r=a}, \tag{2.9a}$$

$$K_m'(W)=K_m'(wa)=\frac{\partial K_m(wr)}{\partial(wr)}\bigg|_{r=a}=\frac{1}{w}\frac{\partial K_m(wr)}{\partial r}\bigg|_{r=a}. \tag{2.9b}$$

The interpretation is as follows: Waveguiding is possible if the eigenvalue equation (2.8) and the auxiliary condition in Eq. (2.7) are fulfilled simultaneously; i.e. inserting the rearranged Eq. (2.7) into (2.8) would leave only one unknown, for instance U. Hence, a numerical solution yields U, then W. The wavenumber β and the effective refractive index $n_{\mathrm{eff}}=\frac{\beta}{k}$ of the mode are found from the rearranged Eqs. in (2.6), where $u=\frac{U}{a}$ and $w=\frac{W}{a}$. This is the reason why the eigenvalue equation (2.8) is called a dispersion relation: Together with (2.7) it connects the optical wavelength λ (and $\omega=\frac{2\pi c}{\lambda}$) with the effective refractive index n_{eff} (and $\beta=kn_{\mathrm{eff}}$).

In general, Eq. (2.8) has a finite number of solutions for each azimuthal index $m=0,1,2,...$ The number is fixed by the normalised frequency V, i.e. by the waveguide characteristics and notably by the optical wavelength λ. The corresponding solutions of the field profiles $\mathbf{f}(r,\phi)$ from the ansatz in Eq. (2.3) are discussed next.

For $m=0$, paired transverse electric (TE) and transverse magnetic (TM) modes are recovered. They are distinguished by vanishing electric or magnetic field components in longitudinal direction, $E_z=0$ or $H_z=0$, respectively. The electric mode profiles are denoted as $\mathbf{TE}_{0,n}$ and $\mathbf{TM}_{0,n}$, where the first index signifies the corresponding $m=0$, and the second index $n=1,2,...$ represents the solution number, ordered by decreasing effective refractive index n_{eff}.

For $m\neq 0$, the dispersion relation leads to hybrid modes that exhibit all six field components. Selecting the minus sign of Eq. (2.8), modes with dominant E_z field components are obtained; they are historically denoted as HE modes. Analogously, the plus sign of Eq. (2.8) leads to modes with dominant H_z field components; these are the EH modes.

Both field solutions, HE and EH modes, arise in pairs (for every m and n), where each mode pair consists of two modes of the same kind and the same wavenumber β. They merely differ by a $\frac{\pi}{2}$-rotation around the propagation axis z. Hence, they are orthogonally polarised and are here named *even* and *odd* modes. The solutions of the angular field

ansatz in Eq. (2.5) are set to

$$\mathbf{g}_m^{(\mathrm{e})}(\phi) = \begin{pmatrix} \cos(m\phi) \\ \sin(m\phi) \\ \cos(m\phi) \end{pmatrix}, \tag{2.10a}$$

$$\mathbf{g}_m^{(\mathrm{o})}(\phi) = \begin{pmatrix} \sin(m\phi) \\ -\cos(m\phi) \\ \sin(m\phi) \end{pmatrix}, \tag{2.10b}$$

where the upper indices (e) and (o) represent even and odd polarisation, respectively. The lower index m is the azimuthal index. The overlap of an even and an odd mode with the same index is thus vanishing, i.e.

$$\int_0^{2\pi} \mathrm{d}\phi \left(\mathbf{g}_m^{(\mathrm{e})}(\phi)\right)^\dagger \cdot \mathbf{g}_m^{(\mathrm{o})}(\phi) = 0. \tag{2.11}$$

$\dagger$ takes the adjoint and $\cdot$ denotes a scalar multiplication.

The physical solution of the mutual radial vector part is [26]:

$$\mathbf{e}_{m,n}^{\mathrm{HE/EH}}(r) = \begin{cases} \begin{pmatrix} \frac{i\beta}{u^2}\left[s\frac{m}{r}\bar{J}_m(r) - u\bar{J}'_m(r)\right] \\ \frac{i\beta}{u^2}\left[\frac{m}{r}\bar{J}_m(r) - su\bar{J}'_m(r)\right] \\ \bar{J}_m(r) \end{pmatrix} & , \text{if } r \le a \\ \begin{pmatrix} -\frac{i\beta}{w^2}\left[s\frac{m}{r}\bar{K}_m(r) - w\bar{K}'_m(r)\right] \\ -\frac{i\beta}{w^2}\left[\frac{m}{r}\bar{K}_m(r) - su\bar{K}'_m(r)\right] \\ \bar{K}_m(r) \end{pmatrix} & , \text{if } r > a \end{cases}. \tag{2.12}$$

The superscript represents the hybrid-mode category, HE or EH respectively. The additional subscript n $\left(\text{in comparison to } \mathbf{g}_m^{(\mathrm{e/o})}\right)$ is the mode's radial index. Moreover, normalised Bessel functions

$$\bar{J}_m(r) = \frac{J_m(ur)}{J_m(ua)}, \tag{2.13a}$$

$$\bar{J}'_m(r) = \frac{J'_m(ur)}{J_m(ua)}, \tag{2.13b}$$

$$\bar{K}_m(r) = \frac{K_m(wr)}{K_m(wa)}, \tag{2.13c}$$

$$\bar{K}'_m(r) = \frac{K'_m(wr)}{K_m(wa)} \tag{2.13d}$$

and the parameter

$$s = \frac{m\left(\frac{1}{U^2} + \frac{1}{W^2}\right)}{\frac{J'_m(U)}{UJ_m(U)} + \frac{K'_m(W)}{WK_m(W)}} \tag{2.14}$$

are defined. As explained above, the dispersion relation in Eq. (2.8) yields numerical (U, W) pairs that determine the unknowns $(u, w, n_{\mathrm{eff}}, \beta, s)$. Since the dispersion relation represents the difference between the two categories of hybrid modes, the parameters differ for HE or EH modes. If we wanted to be more precise, an extended notation with additional indices $(u_{m,n}^{\mathrm{HE/EH}}, w_{m,n}^{\mathrm{HE/EH}}, n_{\mathrm{eff}_{m,n}}^{\mathrm{HE/EH}}, \beta_{m,n}^{\mathrm{HE/EH}}, s_{m,n}^{\mathrm{HE/EH}})$ would be necessary, but is

omitted for clarity. Here, only the indices of the radial vector part $\mathbf{e}_{m,n}^{\mathrm{HE/EH}}(r)$ indicate the modal solution.

A componentwise multiplication of the radial vector part in Eq. (2.12) and the angular vector part in Eq. (2.10) leads to the total transverse mode profiles $\mathbf{f}(r,\phi)$ of the HE and EH modes:

$$\mathbf{HE}_{m,n}^{(\mathrm{e/o})}(r,\phi) = \mathbf{e}_{m,n}^{\mathrm{HE}}(r) \circ \mathbf{g}_{m}^{(\mathrm{e/o})}(\phi), \tag{2.15a}$$

$$\mathbf{EH}_{m,n}^{(\mathrm{e/o})}(r,\phi) = \mathbf{e}_{m,n}^{\mathrm{EH}}(r) \circ \mathbf{g}_{m}^{(\mathrm{e/o})}(\phi). \tag{2.15b}$$

This concludes the explanation of the mathematical background. We proceed by illustrating the mode profiles: On the left side of Fig. 2.2, the first modal solutions of the dispersion relation are shown. They are qualitatively ordered by their wavenumbers β and effective refractive indices $n_{\mathrm{eff}} = \frac{\beta}{k}$. The description ensues from left to right - from top to bottom.

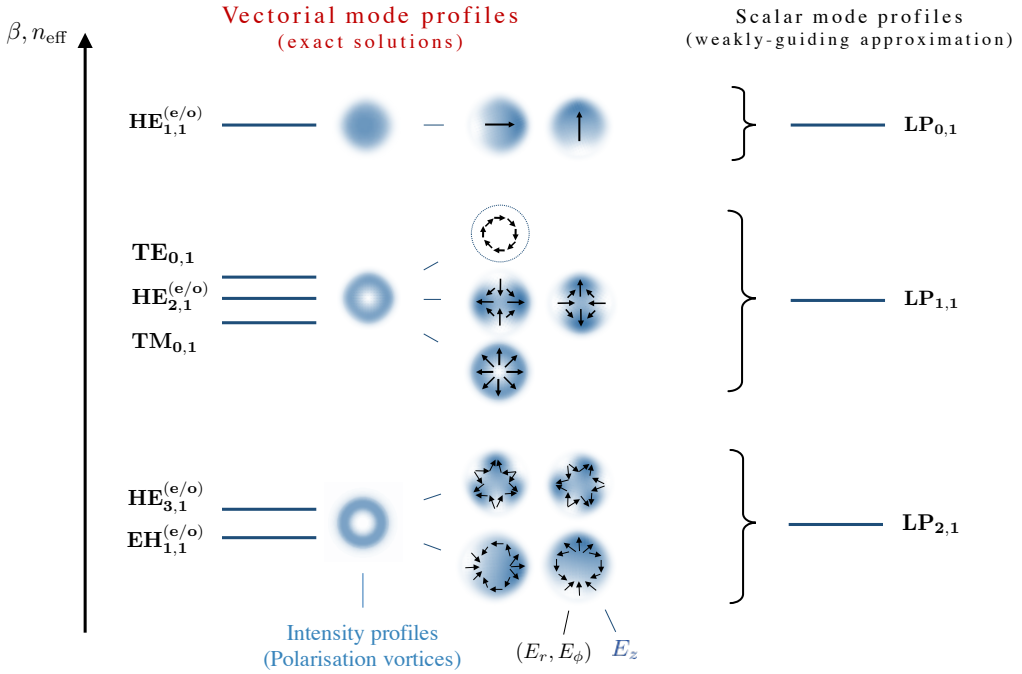

Fig. 2.2 Transverse modes in a cylindrical core-cladding waveguide according the exact derivation and in the weakly-guiding approximation $\varepsilon_{\mathrm{co}} \approx \varepsilon_{\mathrm{cl}}$, where $n = 1$. Blue lines denote qualitatively the modal succession according to wavenumbers β and effective refractive indices n_{eff}. Contour plots (on the left) illustrate intensity profiles of the corresponding electromagnetic fields, given by the associated power flow (the time-averaged Poynting vector in longitudinal direction) [27]. Contour plots (in the middle) show the electric field components in z-direction. Overlying black arrows represent the polarisation of the modes; that is to say a very rough vector plot of the electric field components (E_r, E_ϕ). The bracerights show which exact mode-profile solutions are transformed into one degenerate LP mode in the weakly-guiding approximation.

The two first solutions are the fundamental $\mathbf{HE}_{1,1}^{(\mathrm{e})}$ and $\mathbf{HE}_{1,1}^{(\mathrm{o})}$ modes. Their (even or odd) polarisation does not influence the wavenumber β of the mode and we see only one line representing both modes' β (n_{eff}) values. They are therefore called degenerate. The same holds for all higher-order hybrid modes. Next, the $\mathbf{TE}_{0,1}$, $\mathbf{HE}_{2,1}^{(\mathrm{e/o})}$ and $\mathbf{TM}_{0,1}$

modes represent the first higher-order solutions and feature a near-degeneracy for small differences between $\varepsilon_{\mathrm{co}}$ and $\varepsilon_{\mathrm{cl}}$ (the three lines would be closer in a quantitative plot). All other higher-order solutions are grouped into near-degenerate $\mathbf{HE}^{(\mathrm{e/o})}_{m+1,1}$ and $\mathbf{EH}^{(\mathrm{e/o})}_{m-1,1}$ mode pairs. Fig. 2.2 shows only the first group with $m = 2$.

Furthermore, the intensity patterns are the same for all grouped modes. The fundamental modes exhibit a Gaussian shape. Higher-order solutions are featured by so-called polarisation vortices: the dark central spots (or bright in Fig. 2.2) are associated with an undefined phase of the electromagnetic field. The size of the vortices is increasing with order.

The modes differ in their individual field components.[5] The depicted contour plots indicate E_z - the mode's orientation in longitudinal direction. For TE modes we have $E_z = 0$. For HE and EH modes of the same azimuthal order, for instance $\mathbf{HE}^{(\mathrm{e/o})}_{1,1}$ and $\mathbf{EH}^{(\mathrm{e/o})}_{1,1}$, the distribution of E_z is similar; but remark that E_z of HE modes is weaker than E_z of EH modes (which is not visible in this qualitative plot). Arrows display the modes' polarisation (E_r, E_ϕ): The orthogonal $\mathbf{HE}^{(\mathrm{e})}_{1,1}$ and $\mathbf{HE}^{(\mathrm{o})}_{1,1}$ modes are here chosen to be horizontally ($\rightarrow$) and vertically ($\uparrow$) polarised. The TE mode possesses azimuthal polarisation whereas the TM mode is radially polarised. Higher-order hybrid modes are marked by a state-of-polarisation at each particular point in the transverse plane. However, in total they are unpolarised since averaging over the whole transverse mode leads to no preferred direction of the electric field. They are azimuthally $\frac{2\pi}{m}$-periodic, see Eq. (2.10).

These polarisation properties of the exact vector solutions are lost when the scalar, weakly-guiding approximation $\varepsilon_{\mathrm{co}} \approx \varepsilon_{\mathrm{cl}}$ is assumed. As illustrated on the right side in Fig. 2.2, all modes of each upper named "group" are transformed into the same linearly polarised $\mathbf{LP}_{m,n}$ mode, thus are degenerate. Besides, the dispersion relation in Eq. (2.8) is (in the approximation) simplified to

$$\frac{J'_m(U)}{UJ_m(U)} + \frac{K'_m(W)}{WK_m(W)} = \pm m \left(\frac{1}{U^2} + \frac{1}{W^2}\right) \tag{2.16}$$

and the parameter s in Eq. (2.14) adopts the specific values

$$s = \begin{cases} -1 \text{ for HE modes} \\ +1 \text{ for EH modes} \end{cases} . \tag{2.17}$$

This will be exploited later to make analytic calculations possible. [28, 29]

In the next subsection we will see how the above mentioned polarisation vortices of higher-order hybrid modes can be converted into another, special vortex type.

[5] Only the electric field components are shown. The magnetic field patterns of hybrid modes exhibit the same shape as those of the electric field. Mainly the strengths of their longitudinal components differ. They manifest a phase difference of $\frac{\pi}{m}$, where m is their first modal index.

2.2 Orbital angular momentum of waveguide modes

Electromagnetic modes that carry non-zero orbital angular momentum (or short "OAM modes") are also featured by an intensity profile with a dark central spot. The difference to polarisation vortices is that the electromagnetic phase fronts are intertwined, i.e. helically structured. Experimentally that beam property can be achieved by using spiral phase plates [30], computer-generated fork holograms [31], and more recently free-space mode sorters [32].

Obtaining the helical phase-front structure of modes inside a waveguide theoretically is the topic of this subsection. In free-space the OAM modes are often described by Laguerre–Gaussian (LG) modes because of their circular symmetry and phase vortex in the centre [33]. In the explored cylindrical core-cladding waveguides though, they must be composed of the modal solutions discussed in the previous subsection 2.1.

In fact, the unpolarised higher-order vector modes already found in Sec. 2.1 are not far away from carrying OAM in the sense that the waveguided OAM modes are also a solution of the initial eigenvalue equation - only in another coordinate system [28]. The angular vector parts $\mathbf{g}_m^{(\mathrm{e/o})}(\phi)$ in Eq. (2.10) were chosen to be composed of cosine and sine functions. But we could also select another orthonormal basis that represents a solution to the initial wave equation: The key point is to linear combine $\mathbf{g}_m^{(\mathrm{e})}(\phi)$ and $\mathbf{g}_m^{(\mathrm{o})}(\phi)$ with a phase shift of $\pm\frac{\pi}{2}$:

$$\mathbf{g}_m^{(\pm)}(\phi) = \mathbf{g}_m^{(\mathrm{e})}(\phi) \pm i\,\mathbf{g}_m^{(\mathrm{o})}(\phi) = \begin{pmatrix}\cos(m\,\phi)\\ \sin(m\,\phi)\\ \cos(m\,\phi)\end{pmatrix} \pm i \begin{pmatrix}\sin(m\,\phi)\\ -\cos(m\,\phi)\\ \sin(m\,\phi)\end{pmatrix} = \begin{pmatrix}1\\ \mp i\\ 1\end{pmatrix} e^{\pm im\phi}, \quad (2.18)$$

such that the electric field components are aligned with the same azimuthal dependency $e^{\pm im\phi}$.

Fig. 2.3 illustrates the resulting modal structures, exemplary for additive linear combinations of the first five waveguide modes; they are ordered according to their corresponding LP groups as discussed in Sec. 2.1.

Looking at the Gaussian shape of the fundamental hybrid modes $\mathbf{HE}_{1,1}^{(\mathrm{e/o})}$, that means nothing else than converting linearly polarised modes into circularly polarised ones. With Eq. (2.18) and the hybrid-mode definition in Eq. (2.15) they are described by

$$\mathbf{\Sigma}^{\pm} = \mathbf{HE}_{1,1}^{(\mathrm{e})} \pm i\,\mathbf{HE}_{1,1}^{(\mathrm{o})} = \mathbf{e}_{1,1}^{\mathrm{HE}}(r) \circ \mathbf{g}_m^{(\pm)}(\phi) = \mathbf{e}_{1,1}^{\mathrm{HE}}(r) \circ \begin{pmatrix}1\\ \mp i\\ 1\end{pmatrix} e^{\pm i\phi}, \quad (2.19)$$

where the upper index represents left (+) or right (−) handed circular polarisation, respectively. This can be seen as an intrinsic rotation, associated with a spin angular momentum (SAM) of the beam per photon of $\sigma = \pm 1$, in units of the reduced Planck constant $\hbar$. The phase fronts are unchanged disconnected surfaces, i.e. in-plane.[6]

[6] Note that the electric field vector of a circularly polarised beam describes a helix along the direction of propagation. Its phase, though — a measure of where the electric field is in its oscillation between peak and trough — is uniform at every point in the beam's cross section.

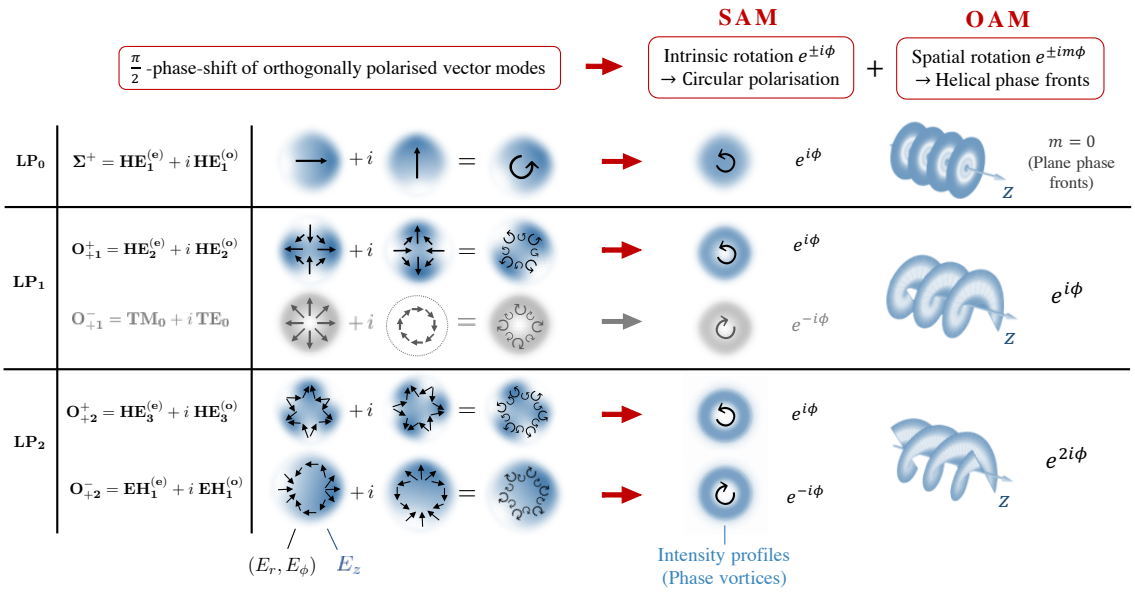

Fig. 2.3 Pictorial representation of the mode transformation, exemplarily shown for additive linear combinations of the optical modes in the first three LP groups. The polarisation patterns in the transverse plane (black arrows) are converted into circular and spatial rotation, associated with spin angular momentum (SAM) and orbital angular momentum (OAM). The transformation of TE and TM modes into OAM modes is depicted in gray since it only exists in theory. The radial indices $n = 1$ are dropped for simplicity. Helical phase fronts from [34].

Higher-order waveguide modes are more interesting: The $\frac{\pi}{2}$-phase shift causes, roughly speaking, the electric field to rotate in the same direction at each particular point in the depicted transverse plane. Altogether, this transforms unpolarised modes into circularly polarised modes. Additionally, we obtain a continuous spatial phase shift in longitudinal direction across the transverse profiles. The phase fronts are consequently helically structured and the modes carry OAM. They are characterised by the topological charge[7] $\pm m$: Its sign determines the rotation direction of the beam's phase front and the positive integer m identifies the number of intertwined helices of the beam. The OAM per photon of the beam is then $m\hbar$. It is defined by the order of the LP group to which the basis modes belong to. That means, each near-degenerate hybrid-mode pair, consisting of $\mathbf{HE}_{m+1,n}^{(e/o)}$ and $\mathbf{EH}_{m-1,n}^{(e/o)}$ modes, yield both OAM modes with topological charges $+m$ or $-m$, referring to an additive or subtractive linear combination, respectively.

The difference of the two hybrid-mode classes is the following: The $\mathbf{HE}_{m+1,n}^{(e/o)}$ modes lead to OAM modes whose corresponding handednesses of its intrinsic circular polarisation and its spatial phase-front structure are the same; or simply speaking, whose associated SAM and OAM are co-rotating. Analogously, OAM modes with contra-rotating SAM and OAM are made up of $\mathbf{EH}_{m-1,n}^{(e/o)}$ modes. The reason for this can be directly seen in their following mathematical notation: Using the definitions of the angular vector parts in Eq. (2.18) and

[7] The notation of topology comes from the different topological structure of beams with unequal OAM. Under the strict mathematical definition, beams with different OAM cannot be smoothly deformed into each other, and are therefore distinct topological entities. [35]

of the hybrid modes in (2.15) they are described by [33]:

$$\mathbf{O}^{+}_{+m,n} = \mathbf{HE}^{(\mathrm{e})}_{m+1,n} + i\,\mathbf{HE}^{(\mathrm{o})}_{m+1,n} = \mathbf{e}^{\mathrm{HE}}_{m+1,n}(r) \circ \mathbf{g}^{(+)}_{m+1}(\phi) = \mathbf{e}^{\mathrm{HE}}_{m+1,n}(r) \circ \begin{pmatrix} 1 \\ -i \\ 1 \end{pmatrix} e^{i\phi}\, e^{im\phi}\,,$$

$$\mathbf{O}^{-}_{-m,n} = \mathbf{HE}^{(\mathrm{e})}_{m+1,n} - i\,\mathbf{HE}^{(\mathrm{o})}_{m+1,n} = \mathbf{e}^{\mathrm{HE}}_{m+1,n}(r) \circ \mathbf{g}^{(-)}_{m+1}(\phi) = \mathbf{e}^{\mathrm{HE}}_{m+1,n}(r) \circ \begin{pmatrix} 1 \\ i \\ 1 \end{pmatrix} e^{-i\phi}\, e^{-im\phi}\,, \tag{2.20a}$$

$$\mathbf{O}^{-}_{+m,n} = \mathbf{EH}^{(\mathrm{e})}_{m-1,n} + i\,\mathbf{EH}^{(\mathrm{o})}_{m-1,n} = \mathbf{e}^{\mathrm{EH}}_{m-1,n}(r) \circ \mathbf{g}^{(+)}_{m-1}(\phi) = \mathbf{e}^{\mathrm{EH}}_{m-1,n}(r) \circ \begin{pmatrix} 1 \\ -i \\ 1 \end{pmatrix} e^{-i\phi}\, e^{im\phi}\,,$$

$$\mathbf{O}^{+}_{-m,n} = \mathbf{EH}^{(\mathrm{e})}_{m-1,n} - i\,\mathbf{EH}^{(\mathrm{o})}_{m-1,n} = \mathbf{e}^{\mathrm{EH}}_{m-1,n}(r) \circ \mathbf{g}^{(-)}_{m-1}(\phi) = \mathbf{e}^{\mathrm{EH}}_{m-1,n}(r) \circ \begin{pmatrix} 1 \\ i \\ 1 \end{pmatrix} e^{i\phi}\, e^{-im\phi}\,, \tag{2.20b}$$

where $m \geq 1$ for $\mathbf{O}^{\pm}_{\pm m,n}$ in Eq. (2.20a) and $m \geq 2$ for $\mathbf{O}^{\mp}_{\pm m,n}$ in Eq. (2.20b). The superscripts represent the mode's SAM (or polarisation handednesses as in Eq. (2.19)) while the subscripts specify the mode's topological charge. With focus on the last expressions on right, we identify the first exponential functions $e^{\pm i\phi}$ as an indicator for left- or right-handed circular polarisation and the second ones $e^{\pm im\phi}$ as the key oscillating term that describes left- or right-handed helical wavefronts, respectively. If the arguments of the exponential functions have the same signs, then the angular momenta of the mode are co-rotating, if different then contra-rotating.

Note that OAM modes with topological charge $m = 1$ and contra-rotating angular momenta can not be described with hybrid modes because the first-order EH mode is in the second-order LP group. However, they could be theoretically composed of the orthogonal TE and TM modes in the $\mathrm{LP}_{1,n}$ group:

$$\mathbf{O}^{\mp}_{\pm 1,n} = \mathbf{TM}_{0,n} \pm i\,\mathbf{TE}_{0,n}. \tag{2.21}$$

In practice, those modes are unstable because of the difference in their propagation constants β, as depicted in Fig. 2.2 [36]. On that account, the $\mathrm{O}^{\mp}_{\pm 1,n}$ modes will not be dealt with further in this thesis.

Moreover, we only work with modes with fixed radial index $n = 1$ since they are mostly the only guided modes in a very narrow core we are looking at [33]. The second indices are thus dropped for simplicity.

Summarising, we have $\mathbf{HE}^{(\mathrm{e/o})}_{m}$, $\mathbf{EH}^{(\mathrm{e/o})}_{m}$, $\mathbf{O}^{\pm}_{\pm m}$, $\mathbf{O}^{\mp}_{\pm m}$ and $\mathbf{\Sigma}^{\pm}$ modes. The basic description of the transverse mode profiles is completed. How these modes modify with changing direction of propagation, i.e. from forwards propagation in $(+z)$-direction to backwards propagation in $(-z)$-direction and vice versa, is explained in the following.

To get a first intuition, we could imagine a forwards travelling mode, say the circularly polarised $\mathbf{\Sigma}^{+}$ mode, which is reflected by a conventional mirror. The mode is thus returning with view in $(-z)$-direction. That means that the z-, and particularly the ϕ-axis is inverted in the inertial frame of reference of the mode. The ϕ-inversion leads to a change of the mode's circular polarisation: the forwards propagating $\mathbf{\Sigma}^{+}$ mode turns into a backwards propagating $\mathbf{\Sigma}^{-}$ mode. Note that the spin is unchanged in the laboratory frame of reference. [37]

In a waveguide the theory is more profound: The initial point is to assume a waveguide material that is

a) lossless with real dielectric constant $\varepsilon(\omega) = \varepsilon^*(\omega)$ and

b) cylindrically symmetric with $\varepsilon(z) = \varepsilon(-z)$.

From a) follows a time-reversal symmetry ($t \to -t$) and from b) a z-inversion symmetry ($z \to -z$) in the linear Maxwell's equations. We are interested in its effect on the mode profiles. For this, we define a general waveguide mode M as

$$\mathbf{M}_m(r, \phi, \beta) = \mathbf{e}_m(r, \beta) \circ \mathbf{g}_m(\phi), \tag{2.22}$$

i.e. separated into its radial and its azimuthal part, where the dependency of the radial parts on the propagation constant β of the mode is additionally listed; see Eq. (2.12) for comparison. From the symmetry properties (time-reversal and z-inversion) in the linear Maxwell's equations follows that if the propagation direction of the mode is reversed, then M undergoes a complex conjugation and the sign of β is changed:

$$\mathbf{M}_m(\beta) \to (\mathbf{M}_m(-\beta))^* \tag{2.23a}$$
$$\mathbf{e}_m(\beta) \to (\mathbf{e}_m(-\beta))^* \tag{2.23b}$$
$$\mathbf{g}_m \to (\mathbf{g}_m)^* \tag{2.23c}$$
$$\beta \to -\beta. \tag{2.23d}$$

Since $\mathbf{e}_m^{\mathrm{HE/EH}}(\beta) = \left(\mathbf{e}_m^{\mathrm{HE/EH}}(-\beta)\right)^*$ with Eq. (2.12), the radial parts of the hybrid modes and OAM modes remain unchanged. The same holds for the azimuthal parts of even and odd modes: $\mathbf{g}_m^{(\mathrm{e/o})} = \left(\mathbf{g}_m^{(\mathrm{e/o})}\right)^*$ with Eq. (2.10). The transverse profiles of forwards and backwards propagating hybrid modes of the same kind are therefore the same. In the case of circularly polarised modes the angular field parts change because

$$\mathbf{g}_m^{(+)} \to \left(\mathbf{g}_m^{(+)}\right)^* = \left(\begin{pmatrix} 1 \\ -i \\ 1 \end{pmatrix} e^{im\phi}\right)^* = \begin{pmatrix} 1 \\ i \\ 1 \end{pmatrix} e^{-im\phi} = \mathbf{g}_m^{(-)} \tag{2.24}$$

and vice versa for opposite signs. Consequently, based on the mode definitions in Eqs. (2.19) and (2.20), the angular momenta of the modes are reversed with changing $\mathbf{g}_m^{(\pm)}$. SAM and OAM change signs.

In summary, the direction of propagation reversal leads to the modal transformations

$$\mathbf{HE}_m^{(\mathrm{e/o})} \to \mathbf{HE}_m^{(\mathrm{e/o})} \tag{2.25a}$$
$$\mathbf{EH}_m^{(\mathrm{e/o})} \to \mathbf{EH}_m^{(\mathrm{e/o})} \tag{2.25b}$$
$$\mathbf{\Sigma}^+ \to \mathbf{\Sigma}^- \tag{2.25c}$$
$$\mathbf{O}_{+m}^+ \to \mathbf{O}_{-m}^- \tag{2.25d}$$
$$\mathbf{O}_{+m}^- \to \mathbf{O}_{-m}^+ \tag{2.25e}$$

and vice versa [38, 39]. They can be experimentally observed by using phase-conjugated mirrors [37] or reflection gratings [40]. Here, both transmission and reflection grating-structures in waveguides are used. They are explained in the next subsection.

2.3 Grating structures in waveguides

So far we have only dealt with the most basic step-index waveguide with constant dielectric constants $\varepsilon_{\mathrm{co}}$ and $\varepsilon_{\mathrm{cl}}$ in the waveguide core or cladding respectively, see Fig. 2.1. Now we introduce a periodically changing dielectric constant in the waveguide core, i.e. a grating structure in longitudinal direction. It can be experimentally created by exposing the core to a periodic pattern of intense ultraviolet light which changes the dielectric constant according to the exposure pattern [41].

As depicted in Fig. 2.4 a), the gratings are broadly classified into two types: transmission gratings with long periodic lengths Λ_{t} and reflection gratings with short periodic lengths Λ_{r}. The gratings lead to a conversion between co- or counterpropagating modes, respectively.

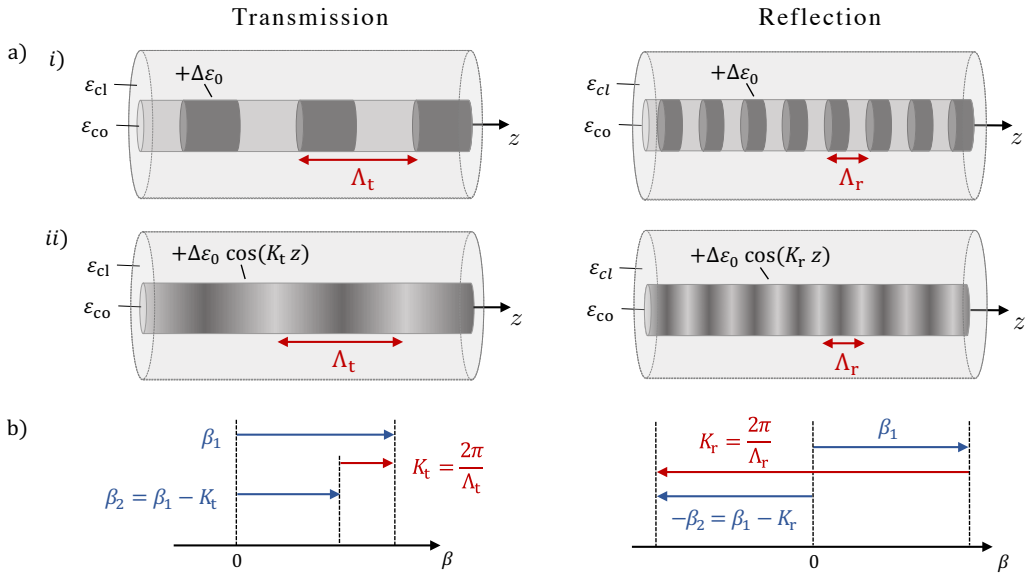

Fig. 2.4 *a*) Uniform transmission and reflection gratings with *i*) discrete and *ii*) continuous periodic-change of the dielectric constant in the waveguide core. *b*) Illustration of the corresponding phase-matching processes in the first-order approximation (losses neglected)

Fig. 2.4 a) *i*) shows discrete-periodic gratings with constant dielectric-constant changes. *ii*) displays grating structures with continuous dielectric-constant distributions. Their total dielectric constant is in the first-order approximation described by

$$\varepsilon(r, z) = \bar{\varepsilon}(r) + \Delta\varepsilon_0 \cos(Kz)\, \Theta(a - r), \tag{2.26}$$

where $\bar{\varepsilon}(r)$ is the mean dielectric constant as in Eq. (2.2) and $\Delta\varepsilon_0$ is the modulation strength, i.e. the maximal change of $\varepsilon_{\mathrm{co}}$. K represents the periodicity of the waveguide, connected with the periodic length Λ via $K = \frac{2\pi}{\Lambda}$. $\Theta(a - r) = \{\, 1, \text{ if } r < a, \vee\ 0, \text{ if } r > a \,\}$ is the Heaviside step-function. It signifies that the grating is only in the waveguide core.

The physical background can be qualitatively described based on simple electromagnetic waves in the waveguide: At each periodic change of the waveguide the waves are partially transmitted and reflected. All the transmitted (or reflected) waves interfere constructively if the waves are in phase.

A simplified version of this phase-matching process is shown in Fig. 2.4 b). We assume a perfect coupling between two modes in the waveguide: an input mode with wavenumber β_1 converts into an output mode with wavenumber β_2. Then, the grating compensates the wavenumber difference with

$$K = \begin{cases} K_\mathrm{t} = \frac{2\pi}{\Lambda_\mathrm{t}} = \beta_1 - \beta_2 & \text{, for transmission gratings} \\ K_\mathrm{r} = \frac{2\pi}{\Lambda_\mathrm{r}} = \beta_1 + \beta_2 & \text{, for reflection gratings} \end{cases} \tag{2.27}$$

where the subscripts t and r label the grating category, i.e. transmission or reflection respectively. Corresponding transmission and reflection spectra are derived by the usage of coupled-mode theory in Sec. 3.1.1. [42]

In summary, the waveguide's grating period determines the propagation direction of the output mode. If the grating is made up of a material with a non-negligible higher-order susceptibility, nonlinear effects are brought into play: entangled photons are generated. The considered process is outlined next.

2.4 Four-wave mixing

The four-wave-mixing (FWM) process is - along with the effect of spontaneous parametric down-conversion (SPDC) - one of the most common sources of photon pairs. It describes the interaction of four modes due to the third-order susceptibility $\chi^{(3)}$ of a material; for example in SiO_2 or GaAs. New modes with sum and difference frequencies are generated.

In detail, we assume two pump fields at single frequencies ω_1 and ω_2 that generate entangled signal and idler modes at frequencies ω_s and ω_i, respectively. The frequencies are correlated via

$$\omega_1 + \omega_2 = \omega_s + \omega_i \tag{2.28}$$

due to energy conservation. Fig. 2.5 a) shows a possible distribution of the frequencies; non-degenerate pumps with $\omega_1 \neq \omega_2$ are considered. In the more general case, a spectral distribution of the modes must be taken into account: The associated wavepackets of the signal (idler) modes overlap with the pump frequencies and a spectral filtering of the generated photons from the pump beam is necessary. In typical quantum optics experiments the spectral separation is larger than $\Delta\omega = 1\,\mathrm{THz}$ such that a 1 nm bandpass-filter can be used for example. [43]

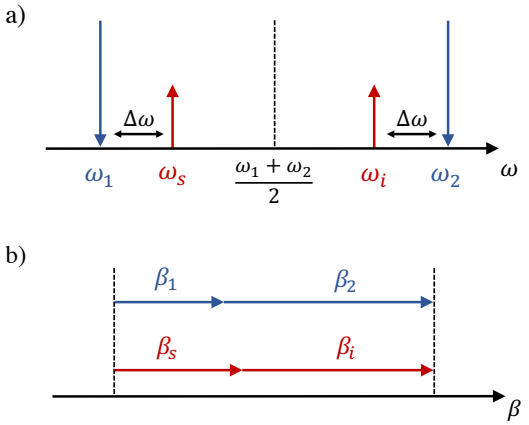

Fig. 2.5 a) Uniform frequency distribution of the interacting modes around the central frequency $(\omega_1 + \omega_2)/2$. b) Illustration of the corresponding propagation constants. Forwards propagating modes of the same class and order are considered. (Blue-coloured symbols denote the pumps; the generated signal and idler fields are marked in red.)

Furthermore, the momentum conservation is inspected. The associated wavenumber mismatch is displayed in Fig. 2.5 b); copropagating modes in transmission gratings are assumed. For perfect phase matching, the summed propagation constants of the two pumps, β_1 and β_2, and of the signal/idler modes, β_s and β_i, are equal. That means

$$\beta_1 + \beta_2 = \beta_s + \beta_i + \Delta\beta_{\mathrm{co}} \tag{2.29}$$

with $\Delta\beta_{\mathrm{co}} = 0$; otherwise the phase matching is imperfect. Note that the wavenumbers are correlated with the angular frequencies according to the dispersion relation of the modes. [44, 45]

In short, the FWM process describes the generation of signal and idler modes and is subject to energy and momentum conservation. In this thesis the FWM process is exploited with respect to cylindrical step-index waveguides. The results are shown in the next chapter.

3 Results

We propose a novel FWM process in periodic waveguides to describe counterpropagating photon pairs that are entangled in their OAM. As sketched in Fig. 3.1, a helical grating structure is considered which leads to the conversion of a fundamental waveguide mode to an OAM mode [46].

Such a grating can be fabricated by homogenously twisting the waveguide under indirect beam irradiation. They are typically written point-by-point by pulsed femtosecond lasers. [47–50]

In theory, the change of the waveguide's dielectric constant is in the first-order approximation described by

$$\Delta\varepsilon(r,\phi,z) = \Delta\varepsilon_0 \cos(Kz - m_g\phi)\,\Theta(a-r) \quad (3.1)$$

where $\Delta\varepsilon_0$ is the modulation strength and K is related to the grating period Λ by $K = \frac{2\pi}{\Lambda}$, as in Eq. (2.26). The additional term $m_g\phi$ leads to a continuous azimuthal variation in the longitudinal direction. $m_g \in \mathbb{Z}$ determines the number of index modulations in the transverse plane. If m_g is positive, then the inscribed helicoids are right-handed; if negative, then left-handed. App. B gives more details on the grating's periodicity.

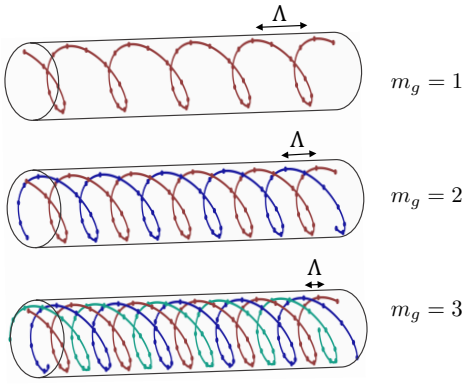

Fig. 3.1 Spiral-shaped grating structure in the cores of cylindrical waveguides, exemplary for one, two and three spirals (from top to bottom). Little dots indicate the experimental laser-writing process. (Colours are just for differentiation.)

First, in Sec. 3.1, the linear mode-coupling process in the waveguide is examined: the transformation of an input mode with transverse profile $\mathbf{f_1}(r,\phi)$ into an output mode with profile $\mathbf{f_2}(r,\phi)$. Both a transmission as well as a reflection grating are assumed. With the acquired results the FWM process is expounded in Sec. 3.2.

3.1 Mode coupling in periodic waveguides

We start with the derivation of the coupled mode equations in Sec. 3.1.1. Transmission and reflection spectra are shown. To estimate the coupling strength, the coupling constants between two modes are deduced analytically, see Sec. 3.1.2. Numerical results are presented in Sec. 3.1.3. In Sec. 3.1.4, a Gedankenexperiment rounds off the topic in an illustrative manner.

3.1.1 Coupled mode equations

The coupled mode equations are derived in the scalar limit. The starting point is the scalar wave equation

$$\left[\boldsymbol{\nabla}^2 - \frac{\varepsilon(r,\phi,z)}{c^2}\frac{\partial^2}{\partial t^2}\right]\mathbf{E}(\mathbf{r},t) = 0, \tag{3.2}$$

similar to Eq. (2.1) which was initially used to derive the electric field in a uniform step-index waveguide. But now the helical grating structure (3.1) in Eq. (3.2) is assumed.

In general, the dielectric-constant distribution is described as a weak perturbation $\Delta\varepsilon(r,\phi,z)$ to the mean dielectric constant $\bar{\varepsilon}(r)$, see Eq. (3.3a). We suppose that the dielectric constant changes periodically in z-direction with grating period Λ: $\Delta\varepsilon(r,\phi,z) = \Delta\varepsilon(r,\phi,z+\Lambda)$. Hence, the perturbation can be represented in a Fourier series, see Eq. (3.3b), where $c_j(r,\phi)$ with $j \in \mathbb{Z}$ are the Fourier coefficients. Since a first-order diffraction grating is assumed, all c_j vanish $\forall\, j \neq \pm 1$, see Eq. (3.3c).

$$\varepsilon(r,\phi,z) = \bar{\varepsilon}(r) + \Delta\varepsilon(r,\phi,z) \tag{3.3a}$$

$$= \bar{\varepsilon}(r) + \sum_{j=-\infty}^{\infty} c_j(r,\phi)\, e^{ijKz} \tag{3.3b}$$

$$= \bar{\varepsilon}(r) + c_1(r,\phi)\, e^{iKz} + c_{-1}(r,\phi)\, e^{-iKz} \tag{3.3c}$$

Then, the Fourier coefficients can be determined via Fourier transformation,

$$c_{\pm1}(r,\phi) = \frac{1}{\Lambda}\int_0^{\Lambda} dz\, \Delta\varepsilon(r,\phi,z)\, e^{\mp iKz}. \tag{3.4}$$

Expressing $\varepsilon(r,\phi,z)$ as the squared refractive index $n(r,\phi,z)$ yields the connection between $\Delta\varepsilon(r,\phi,z)$ and $\Delta n(r,\phi,z)$:

$$\varepsilon(r,\phi,z) = n^2(r,\phi,z) \tag{3.5a}$$

$$= [\,\bar{n}(r) + \Delta n(r,\phi,z)\,]^2 \tag{3.5b}$$

$$= \underbrace{[\,\bar{n}(r)\,]^2}_{=\bar{\varepsilon}(r)} + \underbrace{[\,2\,\bar{n}(r)\Delta n(r,\phi,z)\,]}_{=\Delta\varepsilon(r,\phi,z)} + \underbrace{[\,\Delta n(r,\phi,z)\,]^2}_{\approx 0}, \tag{3.5c}$$

where higher-order perturbations of the refractive index are neglected, $[\Delta n(r,\phi,z)]^2 \approx 0$. Hence,

$$\Delta\varepsilon_0 = 2 n_{\mathrm{co}} \Delta n_0 \tag{3.6}$$

by virtue of Eqs. (2.2) and (3.1). Δn_0 is the perturbation of the waveguide's refractive index.

Our dielectric-constant distribution in Eq. (3.1) has with Eq. (3.4) the first-order Fourier coefficients[1]

$$c_{\pm1}(r,\phi) = \frac{\Delta\varepsilon_0}{2}\, e^{\mp i m_g \phi}\, \Theta(a-r). \tag{3.7}$$

[1] Since $\Delta\varepsilon(r,\phi)$ in Eq. (3.1) is already in the first-order approximation, no Fourier series would be required at this point. It is merely denoted for generality.

Furthermore, the Hermitian electric field $\mathbf{E}$ can be represented as a sum of $\mathbf{E}^{(+)}$ (referring to the "positive" frequency part) and its complex conjugate $\mathbf{E}^{(-)}$ (the "negative" frequency part):

$$\mathbf{E} = \mathbf{E}^{(+)} + \mathbf{E}^{(-)}. \tag{3.8}$$

In the rotating wave approximation (RWA), $\mathbf{E}^{(+)}$ and $\mathbf{E}^{(-)}$ can be treated separately. We thus solve the wave equation (3.2) only for $\mathbf{E}^{(+)}$. The ansatz for the electric field solution is

$$\mathbf{E}^{(+)}(\mathbf{r}, t) = \left(\sum_j a_j(z,t)\, \mathbf{f_j}(r,\phi)\, e^{\pm i\beta_j z} \right) e^{-i\omega t}, \tag{3.9}$$

where the bracketed term is a superposition of electric modes that vary harmonically in time with the same angular frequency ω. Each mode is labelled with a positive integer $j \in \mathbb{N}$ and consists of a vectorial mode profile $\mathbf{f_j}(r,\phi)$ which oscillates in longitudinal direction with propagation constant $\beta_j > 0$. If the argument of the phase term is positive $(+)$, then the mode is forwards propagating; if negative $(-)$, then backwards propagating. $a_j(z,t)$ denotes the mode amplitude that varies in time and z-direction.

In general, many modes must be taken into account since the perturbation couples one mode into lots of other (bound and radiation) modes. However, in the weak mode-coupling regime (small perturbation of uncoupled modes) we suppose that the coupling is mainly restricted to two modes [51]. For simplicity, we start by setting both modes to be forwards propagating:

$$\mathbf{E}^{(+)}(\mathbf{r}, t) = \left(a_1(z,t)\, \mathbf{f_1}(r,\phi)\, e^{i\beta_1 z} + a_2(z,t)\, \mathbf{f_2}(r,\phi)\, e^{i\beta_2 z} \right) e^{-i\omega t}. \tag{3.10}$$

This electric field ansatz, as well as the ansatz for the dielectric constant distribution in Eq. (3.3c), are used to solve the wave equation (3.2). While doing so, the slowly-varying envelope approximation $\frac{\partial^2 a_j}{\partial z^2} \ll \beta_j \frac{\partial a_j}{\partial z}$ is assumed, where $j \in \{1, 2\}$. The substitutions lead to:

$$\begin{aligned}
&\left(2i\beta_1 \frac{\partial a_1}{\partial z} + 2i\omega \frac{\bar{\varepsilon}(r)}{c^2} \frac{\partial a_1}{\partial t} \right) \mathbf{f_1}\, e^{i\beta_1 z} \\
&+ \left(2i\beta_2 \frac{\partial a_2}{\partial z} + 2i\omega \frac{\bar{\varepsilon}(r)}{c^2} \frac{\partial a_2}{\partial t} \right) \mathbf{f_2}\, e^{i\beta_2 z} \\
&+ \frac{\omega^2}{c^2} \left(\frac{\Delta\varepsilon_0}{2}\, e^{-im_g\phi}\, \Theta(a-r) \right) \left(a_1\, \mathbf{f_1}\, e^{i(\beta_1+K)z} + a_2\, \mathbf{f_2}\, e^{i(\beta_2+K)z} \right) \\
&+ \frac{\omega^2}{c^2} \left(\frac{\Delta\varepsilon_0}{2}\, e^{im_g\phi}\, \Theta(a-r) \right) \left(a_1\, \mathbf{f_1}\, e^{i(\beta_1-K)z} + a_2\, \mathbf{f_2}\, e^{i(\beta_2-K)z} \right) = 0.
\end{aligned} \tag{3.11}$$

Six different wavenumbers arise, here marked in blue. The upper two terms with β_1 and β_2 represent the unperturbed part of the electric field. The effect of the grating is shown by the latter four expressions with $\beta_1 \pm K$ and $\beta_2 \pm K$: the shift of the initial propagation constants β_1 and β_2 by the wavenumber analogue K of the grating.

To phase match the modes the first mode with wavenumber β_1 is chosen to be the input mode which shall be converted into the second mode with wavenumber β_2; according to the ansatz of the electric field in Eq. (3.10). Since both modes are forwards propagating, a transmission grating is used. $K = K_\mathrm{t}$ in Eq. (2.27) compensates the wavenumber

difference. The latter four wavenumbers in Eq. (3.11) are rewritten in terms of β_1 and β_2,

$$\begin{aligned}\beta_1 + K &\rightarrow 2\beta_1 - \beta_2\\ \beta_1 - K &\rightarrow \beta_2\\ \beta_2 + K &\rightarrow \beta_1\\ \beta_2 - K &\rightarrow -\beta_1 + 2\beta_2.\end{aligned}$$

The second and third lines show how the grating phase matches the two modes as K shifts β_1 to β_2 and vice versa. The electric field modes with the firstly and the fourthly listed propagation constants are fast oscillating, thus negligible. Eq. (3.11) is reduced to

$$\begin{aligned}&\left(2i\beta_1\frac{\partial a_1}{\partial z}\,\mathbf{f_1} + \frac{2i\omega}{c^2}\bar{\varepsilon}(r)\frac{\partial a_1}{\partial t}\,\mathbf{f_1} + \frac{\Delta\varepsilon_0\,\omega^2}{2c^2}\,a_2\,\mathbf{f_2}\,e^{-im_g\phi}\,\Theta(a-r)\right)e^{i\beta_1 z}\\ &+\left(2i\beta_2\frac{\partial a_2}{\partial z}\,\mathbf{f_2} + \frac{2i\omega}{c^2}\bar{\varepsilon}(r)\frac{\partial a_2}{\partial t}\,\mathbf{f_2} + \frac{\Delta\varepsilon_0\,\omega^2}{2c^2}\,a_1\,\mathbf{f_1}\,e^{im_g\phi}\,\Theta(a-r)\right)e^{i\beta_2 z} = 0.\end{aligned} \tag{3.12}$$

For this equation to hold true, each excluded term must vanish identically such that the equations

$$2i\beta_1\frac{\partial a_1}{\partial z}\,\mathbf{f_1} + \frac{2i\omega}{c^2}\bar{\varepsilon}(r)\frac{\partial a_1}{\partial t}\,\mathbf{f_1} + \frac{\Delta\varepsilon_0\,\omega^2}{2c^2}\,a_2\,\mathbf{f_2}\,e^{-im_g\phi}\,\Theta(a-r) = 0, \tag{3.13a}$$

$$2i\beta_2\frac{\partial a_2}{\partial z}\,\mathbf{f_2} + \frac{2i\omega}{c^2}\bar{\varepsilon}(r)\frac{\partial a_2}{\partial t}\,\mathbf{f_2} + \frac{\Delta\varepsilon_0\,\omega^2}{2c^2}\,a_1\,\mathbf{f_1}\,e^{im_g\phi}\,\Theta(a-r) = 0 \tag{3.13b}$$

represent a coupling between two modes with profiles $\mathbf{f_{1,2}}(r,\phi)$ and amplitudes $a_{1,2}(z,t)$. For further simplification, the equations are modified in the following way: Eq. (3.13a) (Eq. (3.13b)) is multiplied with $\frac{\mathbf{f_1}^\dagger}{2\beta_1}$ $\left(\frac{\mathbf{f_2}^\dagger}{2\beta_2}\right)$ from the left. The terms are then integrated over the whole transverse plane; the integration is denoted as in the bracket notation via $\langle\mathbf{x}|\eta|\mathbf{y}\rangle \equiv \int_0^\infty dr\,r\int_0^{2\pi}d\phi\;\mathbf{x}^\dagger\cdot(\eta\,\mathbf{y})$. We apply the normalisation $\mathbf{f_j} \rightarrow \frac{\mathbf{f_j}}{\sqrt{\langle\mathbf{f_j}|\bar{\varepsilon}(r)|\mathbf{f_j}\rangle}}$ where $j \in \{1,2\}$ and multiply the first (second) equation with $\frac{\langle\mathbf{f_1}|\bar{\varepsilon}(r)|\mathbf{f_1}\rangle}{\langle\mathbf{f_1}|\mathbf{f_1}\rangle}$ $\left(\frac{\langle\mathbf{f_2}|\bar{\varepsilon}(r)|\mathbf{f_2}\rangle}{\langle\mathbf{f_2}|\mathbf{f_2}\rangle}\right)$. The result is the following:

$$i\frac{\partial a_1}{\partial z} + \underbrace{i\,\frac{\omega}{\beta_1 c^2}\frac{\langle\mathbf{f_1}|\bar{\varepsilon}(r)|\mathbf{f_1}\rangle}{\langle\mathbf{f_1}|\mathbf{f_1}\rangle}}_{1/v_{G1}}\frac{\partial a_1}{\partial t} + \underbrace{\frac{\Delta\varepsilon_0\,\omega^2}{4\beta_1 c^2}\sqrt{\frac{\langle\mathbf{f_1}|\bar{\varepsilon}(r)|\mathbf{f_1}\rangle}{\langle\mathbf{f_2}|\bar{\varepsilon}(r)|\mathbf{f_2}\rangle}}\,\frac{\langle\mathbf{f_1}|e^{-im_g\phi}\,\Theta(a-r)|\mathbf{f_2}\rangle}{\langle\mathbf{f_1}|\mathbf{f_1}\rangle}}_{\kappa_1}\,a_2 = 0, \tag{3.14a}$$

$$i\frac{\partial a_2}{\partial z} + \underbrace{i\,\frac{\omega}{\beta_2 c^2}\frac{\langle\mathbf{f_2}|\bar{\varepsilon}(r)|\mathbf{f_2}\rangle}{\langle\mathbf{f_2}|\mathbf{f_2}\rangle}}_{1/v_{G2}}\frac{\partial a_2}{\partial t} + \underbrace{\frac{\Delta\varepsilon_0\,\omega^2}{4\beta_2 c^2}\sqrt{\frac{\langle\mathbf{f_2}|\bar{\varepsilon}(r)|\mathbf{f_2}\rangle}{\langle\mathbf{f_1}|\bar{\varepsilon}(r)|\mathbf{f_1}\rangle}}\,\frac{\langle\mathbf{f_2}|e^{im_g\phi}\,\Theta(a-r)|\mathbf{f_1}\rangle}{\langle\mathbf{f_2}|\mathbf{f_2}\rangle}}_{\kappa_2}\,a_1 = 0. \tag{3.14b}$$

As highlighted, the group velocities of the modes are identified with

$$v_{G_j} = |\mathbf{v}_{G_j}| = c\,n_{\mathrm{eff}_j}\frac{\langle\mathbf{f_j}|\mathbf{f_j}\rangle}{\langle\mathbf{f_j}|\bar{\varepsilon}(r)|\mathbf{f_j}\rangle}, \tag{3.15}$$

where $n_{\mathrm{eff}_j} = \frac{c\,\beta_j}{\omega}$ is the effective refractive index of mode j. A derivation is offered by

App. A. Furthermore,

$$\kappa_1 = \frac{\Delta\varepsilon_0\,\omega^2}{4\beta_1 c^2}\sqrt{\frac{\langle \mathbf{f_1}|\bar{\varepsilon}(r)|\mathbf{f_1}\rangle}{\langle \mathbf{f_2}|\bar{\varepsilon}(r)|\mathbf{f_2}\rangle}}\,\frac{\langle \mathbf{f_1}|e^{-im_g\phi}\,\Theta(a-r)|\mathbf{f_2}\rangle}{\langle \mathbf{f_1}|\mathbf{f_1}\rangle}, \tag{3.16a}$$

$$\kappa_2 = \frac{\Delta\varepsilon_0\,\omega^2}{4\beta_2 c^2}\sqrt{\frac{\langle \mathbf{f_2}|\bar{\varepsilon}(r)|\mathbf{f_2}\rangle}{\langle \mathbf{f_1}|\bar{\varepsilon}(r)|\mathbf{f_1}\rangle}}\,\frac{\langle \mathbf{f_2}|e^{im_g\phi}\,\Theta(a-r)|\mathbf{f_1}\rangle}{\langle \mathbf{f_2}|\mathbf{f_2}\rangle} \tag{3.16b}$$

are the so-called coupling constants. The coupled mode equations become

$$i\frac{\partial a_1}{\partial z} + i\frac{1}{v_{G1}}\frac{\partial a_1}{\partial t} + \kappa_1\, a_2 = 0, \tag{3.17a}$$

$$(-)\; i\frac{\partial a_2}{\partial z} + i\frac{1}{v_{G2}}\frac{\partial a_2}{\partial t} + \kappa_2\, a_1 = 0 \tag{3.17b}$$

for copropagating modes in a transmission grating. In case of reflection gratings the equations can be derived in an analogous way. The solution is the same except for the additional (red-coloured) minus sign in front of the first term in the second equation.

These differential equations represent the coupling between the (slowly-varying) mode amplitudes $a_1(z,t)$ and $a_2(z,t)$. The strength of the coupling depends on the coupling constants $\kappa_{1,2} \propto \langle\, \mathbf{f_{1,2}}\,|\,e^{\mp im_g\phi}\,\Theta(a-r)\,|\,\mathbf{f_{2,1}}\,\rangle$. They provide information about the overlap of the mode profiles $\mathbf{f_1}(r,\phi)$ and $\mathbf{f_2}(r,\phi)$ in the grating with azimuthal modulation $e^{\mp im_g\phi}$. Their calculation is postponed to the next subsection.

Here, we study the effect of an imperfect phase-matching process. We investigate what happens if the frequency of the incoming light ω does not exactly match the resonant frequency ω_g of the grating. The frequency detuning is assumed to be small - for example $\omega - \omega_g = 1\,\mathrm{THz} \ll \omega_g$. The mode amplitudes are in this case described by a slow oscillation:

$$a_j(z,t) = \tilde{a}_j(z)\; e^{i\alpha z}\, e^{-i(\omega-\omega_g)t}. \tag{3.18}$$

The first phase factor with

$$\alpha = \frac{\omega - \omega_g}{\bar{v}_G} \tag{3.19}$$

represents a shift of the coordinate system to the average group velocity $\bar{v}_G = \frac{1}{2}(v_{G1} + v_{G2})$ of the modes. Considering the wavevector decomposition around ω_g,

$$\beta_j(\omega) = \beta_j(\omega_g) + \left.\frac{\partial\beta_j}{\partial\omega}\right|_{\omega_g}(\omega-\omega_g) + \dots\,, \tag{3.20}$$

the wavenumber difference between input and output mode is obtained:

$$\beta_1(\omega) - \beta_2(\omega) = \underbrace{\beta_1(\omega_g) - \beta_2(\omega_g)}_{K_\mathrm{t}} + \underbrace{\left(\frac{1}{v_{G1}} - \frac{1}{v_{G2}}\right)(\omega-\omega_g)}_{2d}. \tag{3.21}$$

We recover the (resonant) phase-matching condition from Eq. (2.27). $2d$ represents the first-order wavenumber detuning.

Substituting (3.18), the coupled mode equations (3.17) become:

$$i\frac{\partial\tilde{a}_1}{\partial z} + d\,\tilde{a}_1 + \kappa_1\,\tilde{a}_2 = 0, \tag{3.22a}$$

$$i\frac{\partial\tilde{a}_2}{\partial z} - d\,\tilde{a}_2 + \kappa_2\,\tilde{a}_1 = 0. \tag{3.22b}$$

Analogous equations can be derived for reflection gratings with the substitution (3.18) without $e^{i\alpha z}$. The wavenumber detuning $2d$ is then proportional to the summed (not subtracted) reciprocal group velocities; using Eqs. (2.27) and (3.21).

By varying d we are able to understand how a given grating behaves for light at different frequencies. The effect can be seen in the solutions of the coupled mode equations. Their derivation is based on the assumption that the coupling constants are complex conjugated to each other:

$$\kappa_2 = \frac{\beta_1}{\beta_2}\frac{\langle\mathbf{f_1}|\mathbf{f_1}\rangle}{\langle\mathbf{f_2}|\mathbf{f_2}\rangle}\frac{\langle\mathbf{f_2}|\bar{\varepsilon}(r)|\mathbf{f_2}\rangle}{\langle\mathbf{f_1}|\bar{\varepsilon}(r)|\mathbf{f_1}\rangle}\,\kappa_1^* \approx \kappa_1^*. \tag{3.23a}$$

We thus drop the subscript with $\kappa := \kappa_1 = \kappa_2^*$. The boundary conditions $\tilde{a}_1(0) = 1$ and $\tilde{a}_2(0) = 0$ are supposed for a transmission grating; i.e. in the beginning of the waveguide, $z = 0$, only the input mode with normalised amplitude 1 shall be present. For a reflection grating, the boundaries $\tilde{a}_1(0) = 1$ and $\tilde{a}_2(L) = 0$ are applied in a similar way, where L is the length of the waveguide. The solutions are listed in the table below.

	Transmission	Reflection
$\tilde{a}_1(z)$	$\left(\cos(\gamma_t z) - \frac{d}{\gamma_t}\sin(\gamma_t z)\right) e^{idz}$	$\frac{\gamma_r\,\cosh(\gamma_r(L-z)) - id\sinh(\gamma_r(L-z))}{\gamma_r\cosh(\gamma_r L) - i\delta\sinh(\alpha L)}\,e^{idz}$
$\tilde{a}_2(z)$	$\frac{\kappa}{\gamma_t}\sin(\gamma_t z)\,e^{-idz}$	$\frac{i\kappa\sinh(\gamma_r(L-z))}{\gamma_r\cosh(\gamma_t L) - id\sinh(\gamma_r L)}\,e^{-idz}$

Tab. 3.1 Solutions of the coupled mode equations (3.17) for both transmission and reflection gratings with $\gamma_t = \sqrt{|\kappa|^2 + d^2}$ and $\gamma_r = \sqrt{|\kappa|^2 - d^2}$, respectively.

In transmission gratings, the mode amplitudes are made up of Cosine and Sine functions representing travelling waves. In reflection gratings, hyperbolic functions are obtained that indicate an exponential decay of the amplitudes with distance.

Associated transmission and reflection spectra show the behaviour of the coupling efficiency with increasing $d \propto (\omega - \omega_g)$, see solid lines in Fig. 3.2. Broadly speaking, the spectra exhibit sinc-shaped pattern. If the frequency of the incoming light matches the grating frequency, $d = 0$, the maximum transmission and reflectivity are obtained. They are given by $T_{\max} = \sin^2(|\kappa|L)$ and $R_{\max} = \tanh^2(|\kappa|L)$, respectively. Therefore it is reasonable to define the coupling-length product $|\kappa|L$ as the "coupling parameter" determining the efficiency of the process [52]. For a perfect transmission grating with $T_{\max} = 1$, the minimum waveguide length is defined by $L_{\min} = \frac{\pi}{2|\kappa|}$. This case is shown in the depicted transmission spectrum. Note that the reflection spectrum is based on a presumably large coupling parameter of $|\kappa|L = 6$. That leads to strong reflections in the photonic band-gap region $|d| < \kappa = 2\,\frac{1}{\mathrm{cm}}$.

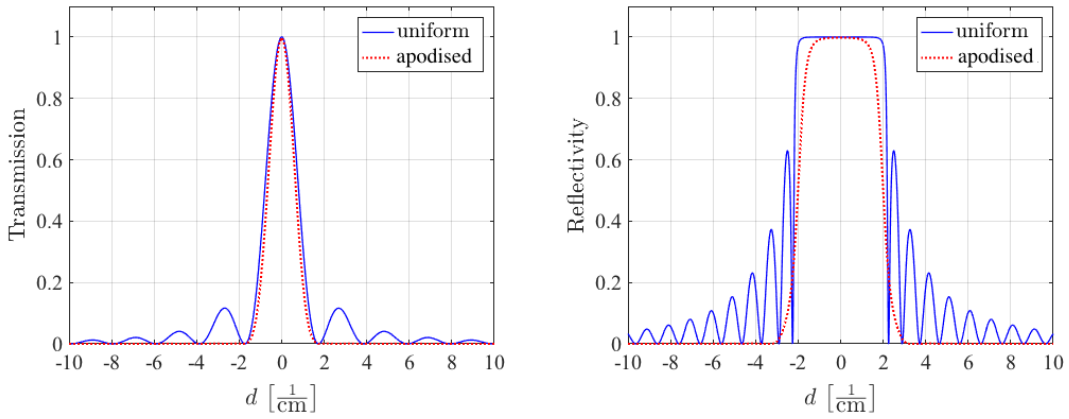

Fig. 3.2 Left: Cross transmission $|\tilde{a}_2(L)|^2$ for a transmission grating with $\kappa = 1\,\frac{1}{\mathrm{cm}}$ and $L = \frac{\pi}{2}\,\mathrm{cm}$. Right: Reflectivity $|\tilde{a}_2(0)|^2$ for a reflection grating with $\kappa = 2\,\frac{1}{\mathrm{cm}}$ and $L = 3\,\mathrm{cm}$. In the case of apodised gratings (see dashed lines), the coupling constant is modulated: it is described by a Gaussian profile $\kappa \to \kappa\, e^{-\frac{(z-L/2)^2}{\Omega^2}}$ with bandwidth $\Omega = \frac{L}{3}$ for both spectra. For the transmission grating the grating length is changed to $L = 0.48\pi\,\mathrm{cm}$ to maintain maximum transmission at $d = 0$.

Furthermore, both spectra (especially the reflectivity) show a series of fringes or "sidelobes" of decreasing strength. The zeroes between the sidelobes can be considered to represent Fabry-Perot resonances of the cavity formed by the ends of the grating. More precisely, the impedance mismatch between the surrounding medium and the grating creates an effective cavity of length L which supports resonant Fabry-Perot modes. These modes manifest as zeroes in the transmission/reflection spectra.

Apodised gratings can suppress the unwanted sidelobes, see dashed lines in Fig. 3.2. Here a modulation of the grating is assumed with a smooth start and stop at the edges of the waveguide. Consequently, the coupling constants $\kappa \propto \Delta\varepsilon_0$ vary with z and the analytical solutions of the coupled mode equations in Tab. 3.1 do not hold any more. The differential equations (3.17) must be solved numerically: the grating is divided into tiny pieces in which the coupling constant is approximately constant. We obtain smoother spectra with vanishing sidelobes. [42]

3.1.2 Coupling constants

In this section, the coupling constants in Eq. (3.16) are calculated for two modes coupled in the helical grating structure defined in Eq. (3.1). The arising overlap integrals are simplified as far as possible and first results are discussed. In short, the calculation is based on the separation of the transverse integrals: the angular integrals can be solved analytically while the radial integrals are left for numerical integration. The derivation is first shown in an exemplary way for a coupling between two even polarised HE modes with different azimuthal indices. Subsequently, the procedure is generalised for all possible mode combinations. Note that only the coupling integrals $\langle \mathbf{f_1} | e^{im_g\phi}\,\Theta(a-r) | \mathbf{f_2} \rangle$ are discussed in the following; the normalisation terms ($\langle \mathbf{f_j} | \mathbf{f_j} \rangle$ and $\langle \mathbf{f_j} | \bar{\varepsilon}(r) | \mathbf{f_j} \rangle$ with $j \in \{1, 2\}$) are shown in App. C.2.

Example: Coupling between two $\mathbf{HE}_m^{(e)}$ modes The azimuthal and radial integrals are separated according to the hybrid mode separation in Eq. (2.15a). That means explicitly:

$$\begin{aligned}
&\langle \mathbf{HE}_m^{(e)} | e^{-im_g\phi}\,\Theta(a-r) | \mathbf{HE}_{\tilde{m}}^{(e)} \rangle \\
&\quad = \int_0^a dr\, r \int_0^{2\pi} d\phi \left(\left[\mathbf{e}_m^{\mathrm{HE}}(r) \circ \mathbf{g}_m^{(e)}(\phi) \right]^\dagger \cdot \left[\mathbf{e}_{\tilde{m}}^{\mathrm{HE}}(r) \circ \mathbf{g}_{\tilde{m}}^{(e)}(\phi)\, e^{-im_g\phi} \right] \right) \\
&\quad = \left[\int_0^a dr\, r\, \left(\mathbf{e}_m^{\mathrm{HE}}(r) \right)^* \circ \mathbf{e}_{\tilde{m}}^{\mathrm{HE}}(r) \right]^T \cdot \left[\int_0^{2\pi} d\phi\, \mathbf{g}_m^{(e)}(\phi) \circ \mathbf{g}_{\tilde{m}}^{(e)}(\phi)\, e^{-im_g\phi} \right],
\end{aligned} \tag{3.24}$$

where † indicates the conjugate transpose and T the (non-conjugated) transpose of the bracketed vector. Since the azimuthal parts of the hybrid modes are real, no conjunction is required for $\mathbf{g}_m^{(e)}(\phi)$. The colours distinguish the input mode (marked in blue) from the output mode (marked in green) including their related azimuthal indices $m, \tilde{m} \geq 1$, which are not equal in general.

The two separated integrals are examined one after another. At first, the integral over azimuthal angle ϕ is solved analytically as follows:

$$\int_0^{2\pi} d\phi\, \mathbf{g}_m^{(e)}(\phi) \circ \mathbf{g}_{\tilde{m}}^{(e)}(\phi)\, e^{-im_g\phi} \tag{3.25a}$$

$$= \int_0^{2\pi} d\phi \begin{pmatrix} \cos(m\phi) \\ \sin(m\phi) \\ \cos(m\phi) \end{pmatrix} \circ \begin{pmatrix} \cos(\tilde{m}\phi) \\ \sin(\tilde{m}\phi) \\ \cos(\tilde{m}\phi) \end{pmatrix} e^{-im_g\phi} \tag{3.25b}$$

$$= \frac{1}{4} \int_0^{2\pi} d\phi \begin{pmatrix} e^{i(m+\tilde{m})\phi} + e^{i(m-\tilde{m})\phi} + e^{-i(m-\tilde{m})\phi} + e^{-i(m+\tilde{m})\phi} \\ -e^{i(m+\tilde{m})\phi} + e^{i(m-\tilde{m})\phi} + e^{-i(m-\tilde{m})\phi} - e^{-i(m+\tilde{m})\phi} \\ e^{i(m+\tilde{m})\phi} + e^{i(m-\tilde{m})\phi} + e^{-i(m-\tilde{m})\phi} + e^{-i(m+\tilde{m})\phi} \end{pmatrix} e^{-im_g\phi} \tag{3.25c}$$

$$= \frac{\pi}{2} \begin{cases} \begin{pmatrix} 1 \\ \pm 1 \\ 1 \end{pmatrix} & \text{, if } \tilde{m} = \pm m_g \pm m \\ 0 & \text{, otherwise} \end{cases}. \tag{3.25d}$$

In the first step, the definition of the vectorial hybrid mode part $\mathbf{g}_m^{(e)}$ in Eq. (2.10a) is applied, see Eq. (3.25b). Then, the cosine and sine functions are rewritten via Euler's identity leading to Eq. (3.25c). The resulting integral is only non-zero if one of the arguments of the exponential functions is vanishing, see Eq. (3.25d), where the red-marked $\pm$ signs are treated independently from the non-coloured one. Hence, the coupling probabil-

ity is non-vanishing only if there is a certain dependency between the azimuthal indices m and $\tilde{m}$ of the coupled hybrid modes and the integer number m_g that determines the grating structure. These dependencies are called "azimuthal phase-matching conditions". That means in practice: The grating structure specifies through m_g which mode combinations can be coupled in the waveguide. If the modes are not phase matched, coupling can not occur and the coupling constants vanish. Therefore, the azimuthal index of the output mode is fixed to one of the four possible summation possibilities of m and m_g. Note that the final expression is independent of the $\pm$ sign in front of m_g; it depends exclusively on $\pm$. Consequently, the handedness of the helical grating does not influence the coupling efficiency; however, it defines the azimuthal order of the output mode.

The solution of the azimuthal integral in Eq. (3.25d) is plugged into the initial coupling integral in Eq. (3.24), see Eq. (3.26a).

$$\begin{aligned}
&\langle \mathbf{HE}_{m}^{(\mathrm{e})} | e^{-im_g\phi}\,\Theta(a-r) | \mathbf{HE}_{\tilde{m}=\pm m_g \pm m}^{(\mathrm{e})} \rangle \\
&\qquad = \frac{\pi}{2}\left[\int_0^a dr\, r\, \left(\mathbf{e}_{m}^{\mathrm{HE}}(r)\right)^{*} \circ \mathbf{e}_{\tilde{m}}^{\mathrm{HE}}(r)\right]^{T} \cdot \begin{pmatrix} 1 \\ \pm 1 \\ 1 \end{pmatrix} && (3.26a) \\
&\qquad = \frac{\pi}{2}\int_0^a dr\, r \left(e_{m_r}^{\mathrm{HE}^*} e_{\tilde{m}_r}^{\mathrm{HE}} \pm e_{m_\phi}^{\mathrm{HE}^*} e_{\tilde{m}_\phi}^{\mathrm{HE}} + e_{m_z}^{\mathrm{HE}^*} e_{\tilde{m}_z}^{\mathrm{HE}}\right) && (3.26b)
\end{aligned}$$

$\mathbf{e}_{m}^{\mathrm{HE}}(r)$ and $\mathbf{e}_{\tilde{m}}^{\mathrm{HE}}(r)$ are rewritten in terms of their three cylindrical components. Their Hadamard product is scalar multiplied with the vectorial solution of the azimuthal integral. The result is Eq. (3.26b), whereby the radial dependencies and brackets for the complex conjugated input mode are omitted for clearness.

The explicit expressions of the multiplied mode parts in the waveguide core ($r \leq a$) are:

$$e_{m_r}^{\mathrm{HE}^*} e_{\tilde{m}_r}^{\mathrm{HE}} = \frac{\beta\tilde{\beta}}{u^2\tilde{u}^2}\left[s\tilde{s}\frac{m\tilde{m}}{r^2}\bar{J}_m\bar{J}_{\tilde{m}} - s\frac{m}{r}\tilde{u}\bar{J}_m\bar{J}'_{\tilde{m}} - \tilde{s}\frac{\tilde{m}}{r}u\bar{J}_{\tilde{m}}\bar{J}'_m + u\tilde{u}\bar{J}'_m\bar{J}'_{\tilde{m}}\right], \tag{3.27a}$$

$$e_{m_\phi}^{\mathrm{HE}^*} e_{\tilde{m}_\phi}^{\mathrm{HE}} = \frac{\beta\tilde{\beta}}{u^2\tilde{u}^2}\left[\frac{m\tilde{m}}{r^2}\bar{J}_m\bar{J}_{\tilde{m}} - \frac{m}{r}\tilde{s}\tilde{u}\bar{J}_m\bar{J}'_{\tilde{m}} - \frac{\tilde{m}}{r}su\bar{J}_{\tilde{m}}\bar{J}'_m + s\tilde{s}u\tilde{u}\bar{J}'_m\bar{J}'_{\tilde{m}}\right], \tag{3.27b}$$

$$e_{m_z}^{\mathrm{HE}^*} e_{\tilde{m}_z}^{\mathrm{HE}} = \bar{J}_m\bar{J}_{\tilde{m}}, \tag{3.27c}$$

according to their definition in Eq. (2.12). Blue-marked parameters (u, w, β, s) correspond to the input mode and green-marked parameters $(\tilde{u}, \tilde{w}, \tilde{\beta}, \tilde{s})$ to the output mode.

The next step is to add/subtract the radial and azimuthal parts in Eqs. (3.27a) and (3.27b): $e_{m_r}^{\mathrm{HE}^*} e_{\tilde{m}_r}^{\mathrm{HE}} \pm e_{m_\phi}^{\mathrm{HE}^*} e_{\tilde{m}_\phi}^{\mathrm{HE}}$. In both expressions, four terms arise with different combinations of Bessel functions and derivatives of Bessel functions. The terms "one on top of the other" are equal except the parameters s and $\tilde{s}$, for instance $s\tilde{s}\frac{m\tilde{m}}{r^2}\bar{J}_m\bar{J}_{\tilde{m}}$ in Eq. (3.27a) and $\frac{m\tilde{m}}{r^2}\bar{J}_m\bar{J}_{\tilde{m}}$ in Eq. (3.27b). As the radial and angular parts are either added or subtracted, the associated terms can be combined by factorising the parameters s and $\tilde{s}$:

$$\begin{aligned}
&e_{m_r}^{\mathrm{HE}^*} e_{\tilde{m}_r}^{\mathrm{HE}} \pm e_{m_\phi}^{\mathrm{HE}^*} e_{\tilde{m}_\phi}^{\mathrm{HE}} \\
&= \frac{\beta\beta}{u^2\tilde{u}^2}\left[(s\tilde{s}\pm 1)\frac{m\tilde{m}}{r^2}\bar{J}_m\bar{J}_{\tilde{m}} - (s\pm\tilde{s})\frac{m}{r}\tilde{u}\bar{J}_m\bar{J}'_{\tilde{m}} - (\tilde{s}\pm s)\frac{\tilde{m}}{r}u\bar{J}_{\tilde{m}}\bar{J}'_m + (1\pm s\tilde{s})u\tilde{u}\bar{J}'_m\bar{J}'_{\tilde{m}}\right] \\
&= \frac{\beta\tilde{\beta}}{u^2u^2}\left[(s\tilde{s}\pm 1)\left(\frac{m\tilde{m}}{r^2}\bar{J}_m\bar{J}_{\tilde{m}} \pm u\tilde{u}\bar{J}'_m\bar{J}'_{\tilde{m}}\right) - (s\pm\tilde{s})\frac{1}{r}\left(m\tilde{u}\bar{J}_m\bar{J}'_{\tilde{m}} \pm \tilde{m}u\bar{J}_{\tilde{m}}\bar{J}'_m\right)\right].
\end{aligned} \tag{3.28}$$

This expression can not be simplified any further.

However, it is possible to at least qualitatively estimate and compare the coupling constants to output modes with different azimuthal indices: the weakly-guiding approximation is exploited to set $s = \tilde{s} = -1$, see Eq. (2.17) for the HE modes we are referring to. It follows:

$$(s\tilde{s} \pm 1) = -(s \pm \tilde{s}) = \begin{cases} 2 \text{ for } + \\ 0 \text{ for } - \end{cases} . \tag{3.29}$$

The accuracy of this approximation is shown in Fig. C.1 in App. C for typical index modulations. The summation of the multiplied radial and azimuthal hybrid mode components leads to a doubling of Eq. (3.27a) (or analogously of Eq. (3.27b)); in case of subtraction they cancel out. With Eq. (3.26b) the coupling terms are:

$$\begin{aligned} &\langle \mathbf{HE}_{m}^{(\mathrm{e})} | e^{-im_g\phi}\,\Theta(a-r) | \mathbf{HE}_{\tilde{m}=\pm m_g+m}^{(\mathrm{e})} \rangle \qquad (3.30\mathrm{a}) \\ &= \frac{\pi}{2}\int_0^a dr\, r \left(\frac{2\beta\tilde{\beta}}{u^2\tilde{u}^2} \left[\frac{m\tilde{m}}{r^2} \bar{J}_m \bar{J}_{\tilde{m}} + u\tilde{u} \bar{J}'_m \bar{J}'_{\tilde{m}} + \frac{1}{r}\left(m\tilde{u} \bar{J}_m \bar{J}'_{\tilde{m}} + \tilde{m} u \bar{J}_{\tilde{m}} \bar{J}'_m \right) \right] + \bar{J}_m \bar{J}_{\tilde{m}} \right), \\ &\langle \mathbf{HE}_{m}^{(\mathrm{e})} | e^{-im_g\phi}\,\Theta(a-r) | \mathbf{HE}_{\tilde{m}=\pm m_g-m}^{(\mathrm{e})} \rangle = \frac{\pi}{2}\int_0^a dr\, r\, \bar{J}_m \bar{J}_{\tilde{m}}. \qquad (3.30\mathrm{b}) \end{aligned}$$

These expressions are left for numerical integration. Note that the integrand in Eq. (3.30b) consists only of the z-components of the radial field parts. Similar expressions are derived for other input/output modes. The generalisation is depicted in the following.

Generalisation: Coupling between different modes The separation of the transverse integrals over radius r and angle ϕ is applied for all mode combinations. Only the azimuthal indices and the polarisations of the modes change. For example, if a hybrid mode couples with the OAM mode $\mathbf{O}_{+\tilde{m}}^{+}$, then, with its definition in Eq. (2.20a), the azimuthal index of its basis hybrid mode is the incremented topological charge of the OAM mode and the azimuthal vector part is an additive superposition:

$$\begin{aligned} &\langle \mathbf{HE}_{m}^{(\mathrm{e})} | e^{-im_g\phi}\,\Theta(a-r) | \mathbf{O}_{+\tilde{m}}^{+} \rangle \\ &= \left[\int_0^a dr\, r\, \left(\mathbf{e}_{m}^{\mathrm{HE}}(r) \right)^* \circ \mathbf{e}_{\tilde{m}+1}^{\mathrm{HE}}(r) \right]^T \cdot \left[\int_0^{2\pi} d\phi\, \mathbf{g}_{m}^{(\mathrm{e})}(\phi) \circ \mathbf{g}_{\tilde{m}+1}^{(+)}(\phi)\, e^{-im_g\phi} \right]. \end{aligned} \tag{3.31}$$

A summarising list of the arising coupling integrals for a fixed input mode-profile $\mathbf{HE}_{m}^{(\mathrm{e})}$ is shown in App. C.1 in Eq. (C.1).

At first, the integrals over azimuthal angle ϕ are determined. We have already seen their calculation for two even polarised hybrid modes in Eq. (3.25). The integrals for a coupling between two hybrid modes with both odd or different polarisations are solved analogously; their (more detailed) calculation can be looked up in the appendix in Eq. (C.2) and (C.3).

Note that the azimuthal integrals for two orthogonal polarised hybrid modes have purely imaginary solutions: Eq. (3.32) shows for instance the azimuthal integral for a coupling between an even polarised input mode and an odd polarised output mode for $m_g \neq 0$.

$$\int_0^{2\pi} d\phi\, \mathbf{g}_{m}^{(\mathrm{e})}(\phi) \circ \mathbf{g}_{\tilde{m}}^{(\mathrm{o})}(\phi)\, e^{-im_g\phi} = \pm\frac{i\pi}{2} \begin{cases} \begin{pmatrix} 1 \\ \pm 1 \\ 1 \end{pmatrix} & , \text{ if } \tilde{m} = \pm m_g \pm m \\ 0 & , \text{ otherwise} \end{cases} \tag{3.32}$$

This is the reason why the final coupling constants are also purely imaginary if the polarisations of the hybrid modes are different. (Because of the solution of the radial integrals the prefactor and the normalisation terms of the coupling constants in Eq. (3.16a) turn out to be real.)

Now we take a look at the azimuthal integrals for a coupling between a hybrid mode and a circularly polarised (OAM) mode. Their solutions are derived from the previous results as $\mathbf{g}_m^{(\pm)}$ can be written as a superposition of even and odd polarised modes, see Eq. (2.18). The explicit decomposition of the azimuthal integral for the mode example in Eq. (3.31) is:

$$\begin{aligned}&\int_0^{2\pi} d\phi\, \mathbf{g}_m^{(\mathrm{e})}(\phi) \circ \mathbf{g}_{\tilde{m}}^{(+)}(\phi)\, e^{-im_g\phi} \\ &\quad= \int_0^{2\pi} d\phi\, \mathbf{g}_m^{(\mathrm{e})}(\phi) \circ \mathbf{g}_{\tilde{m}}^{(\mathrm{e})}(\phi)\, e^{-im_g\phi} + i\int_0^{2\pi} d\phi\, \mathbf{g}_m^{(\mathrm{e})}(\phi) \circ \mathbf{g}_{\tilde{m}}^{(\mathrm{o})}(\phi)\, e^{-im_g\phi}.\end{aligned} \tag{3.33}$$

The results of the two arising integrals are given by Eq. (3.25) and (3.32). Hence:

$$\int_0^{2\pi} d\phi\, \mathbf{g}_m^{(\mathrm{e})}(\phi) \circ \mathbf{g}_{\tilde{m}}^{(+)}(\phi)\, e^{-im_g\phi} = \pi \begin{cases} \begin{pmatrix} 1 \\ \pm 1 \\ 1 \end{pmatrix} & \text{, if } \tilde{m} = m_g \pm m \\ 0 & \text{, otherwise} \end{cases}. \tag{3.34}$$

Only two azimuthal phase-matching conditions are fulfilled. In case $\tilde{m} = -m_g \pm m$, the two integrals in Eq. (3.33) cancel out and no coupling is possible. The other azimuthal integrals for a coupling between a hybrid mode with a circularly polarised (OAM) mode are solved analogously.

Finally, in case of coupling between two circularly polarised (OAM) modes, only one azimuthal phase-matching condition is fulfilled. It can be derived from the previous results in an analogous way. Consequently, a grating with a unique m_g is required to achieve coupling between two chosen mode profiles. Or from another perspective: the grating determines uniquely how the topological charge of the input mode is transformed into the topological charge of the output mode. All results of the azimuthal integrals are summarised in App. C.1, Tab. C.1.

Moreover, the radial integrals are solved as in Eqs. (3.27) to (3.28) for two coupled HE modes. The difference to the treatment of EH modes is the parameter set $(u, w, n_{\mathrm{eff}}, \beta, s)$, reminding of the discussion in Sec. 2.1. The radial and azimuthal terms vanish in the weakly-guiding approximation in the same way, if both excluded terms are zero: $(s\tilde{s} \pm 1) = 0$ and $(s \pm \tilde{s}) = 0$. In the case of EH modes, only the sign of s changes, see Eq. (2.17). The explicit solutions of the entire coupling terms $\langle \mathbf{f_1} | e^{im_g\phi}\, \Theta(a-r) | \mathbf{f_2} \rangle$ are listed in App. C.1.

In the next subsection, the numerical results of $|\kappa|$ are shown. The so far merely mathematically discovered azimuthal phase-matching conditions will be interpreted.

3.1.3 Numerical results and discussion

The resulting coupling constants are presented for different input modes $\mathbf{f_1}$. The input mode $\mathbf{HE}_m^{(e)}$ is discussed in Sec. 3.1.3.1, followed by $\mathbf{O}_{+1}^{+}$ in Sec. 3.1.3.2. The azimuthal phase-matching conditions determine possible output modes $\mathbf{f_2}$ under the consideration of transmission gratings. How the results change for reflection gratings is explained later. In all calculations, a low-contrast optical waveguide made from glass with refractive indices of $n_{\mathrm{co}} = 1.45$ and $n_{\mathrm{cl}} = 1.44$ is assumed. The perturbation strength of the grating is $\Delta n_0 = 1.0 \times 10^{-2}$. $a = 20\,\mu\mathrm{m}$ is the core radius and $\lambda = 1.55\,\mu\mathrm{m}$ is the pump wavelength ($\Rightarrow V = 13.8$ with Eq. (2.7) and $\Delta\varepsilon_0 = 2.9 \times 10^{-2}$ with Eq. (3.6)).

3.1.3.1 Mode coupling to hybrid mode $\mathbf{HE}_1^{(e)}$

The coupling constants for a coupling with input mode $\mathbf{HE}_1^{(e)}$ are graphically shown in Fig. 3.3. Each integer m_g on the abscissa represents another grating structure, see Eq. (3.1) for definition. The boxes at each calculated value label the corresponding output modes.

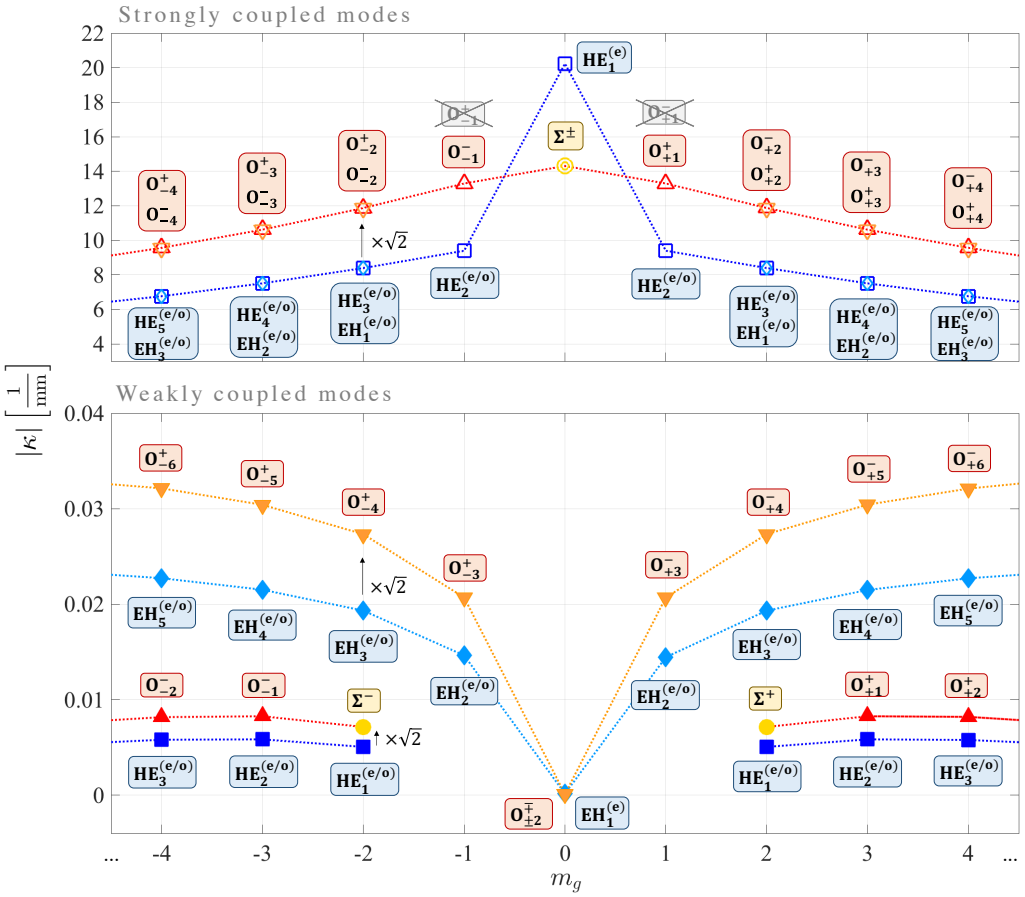

Fig. 3.3 Coupling constants $|\kappa|$ for a coupling between input mode $\mathbf{HE}_1^{(e)}$ and all possible output modes in a grating with $|m_g|$ spirals. The sign of m_g determines the spirals' rotation direction. The coupled modes are sorted into two graphs according to their coupling strength ("strong" or "weak"). Dotted lines show which modes correspond to the same LP group in the weakly-guiding approximation, see Sec. 2.1 and 2.2 for details. Note that the $\mathbf{O}_{-1}^{+}$ and $\mathbf{O}_{+1}^{-}$ modes are not considered as they are unstable, reminding Eq. (2.21); they are marked with the gray, crossed out boxes on the top.

To elaborate the variety of information in the graph, the description ensues step-by-step, divided into paragraphs. Firstly, in paragraph A), the scale of the coupling constants is pointed out. In B), the azimuthal orders of the output modes are explained while in C) some of the associated coupling processes are illustrated. D), E) and F) together explain the relative change of the coupling constants with respect to m_g and the mode categories. How the use of reflection gratings changes the mode-coupling process is addressed in G). In H), the theoretical grating period for perfect phase-matching is determined.

A) Order of magnitude The strongly coupled output modes exhibit coupling constants in the range of $[6.9, 20]\,\frac{1}{\mathrm{mm}}$. Those of the weakly coupled modes are at least two orders of magnitude less. The minimum waveguide length for maximum transmission can be approximated by $L_{\min} = \frac{\pi}{2|\kappa|}$, see Sec. 3.1.1. It follows for a strongly coupled OAM mode $\mathbf{O}^{\pm}_{\pm 1}$ with $|\kappa| = 13\,\frac{1}{\mathrm{mm}}$:

$$L_{\min}^{(\mathrm{strong})}\left(\mathbf{HE}_1^{(\mathrm{e})} \to \mathbf{O}^{\pm}_{\pm 1}\right) = 0.12\,\mathrm{mm}. \tag{3.35}$$

The minimum length for a weakly coupled mode of the same kind is with $|\kappa| = 0.01\,\frac{1}{\mathrm{mm}}$:

$$L_{\min}^{(\mathrm{weak})}\left(\mathbf{HE}_1^{(\mathrm{e})} \to \mathbf{O}^{\pm}_{\pm 1}\right) = 15.7\,\mathrm{cm}. \tag{3.36}$$

With increasing length of the waveguide, intermodal crosstalk and the effects of non-ideal fibres (ellipticity by stress, fibre bend radius by bending) are enlarging, leading to a decreasing efficiency. Only the strongly coupled modes with $\kappa > 1\,\frac{1}{\mathrm{mm}}$ are expected to be stable. [19]

B) Conservation of total angular momentum The orders of the output mode are determined by the azimuthal phase-matching condition derived in Sec. 3.1.2, see Eqs. (3.30a) and (3.30b). Here, the input mode is the fundamental one with $m = 1$. The HE output modes with $\tilde{m} = |m_g| + 1$ are strongly coupled, while those with $\tilde{m} = |m_g| - 1$ are weakly coupled; analogously for all other modes.[2] Interpreting, the conditions represent the conservation of total angular momentum (TAM) - notably not the conservation of OAM. That means, if we would assume a coupling between two OAM modes with spins $\sigma, \tilde{\sigma} \in \{1, -1\}$ (associated with left- or right-handed circular polarisation) and topological charges $\pm m, \pm\tilde{m} \in \{0, \pm 1, \pm 2, \dots\}$ in a grating of order m_g, then

$$\pm\,\tilde{m} + \tilde{\sigma} = \pm\, m + \sigma + m_g \tag{3.37}$$

must be fulfilled, where the green/blue $\pm$ signs are independent of each other. In words: the total angular momentum of the output mode $(\pm\tilde{m} + \tilde{\sigma})$ is equal to the total angular momentum of the input mode $(\pm m + \sigma)$, increased by the grating's twist number m_g. Mode coupling can lead to a transformation of SAM into OAM and vice versa. (For hybrid modes with neither circular polarisation nor OAM, the azimuthal indices represent the mode's potential "degree" of OAM, i.e. the order of the polarisation vortex; see Sec. 2.2 for the impact of the associated $\frac{\pi}{2}$-phase shift.)

[2] Since the enumeration of the waveguide modes starts at 1, no weakly coupled hybrid modes are obtained for $|m_g| \leq 1$.

C) Illustration It follows a visualisation of the possible combinations of the input/output modes. We start with a waveguide without grating. As depicted in Fig. 3.4, the $\mathbf{HE}_1^{(e)}$ input mode is either strongly coupled to the same mode (in a), or weakly coupled to a first-order EH mode (in b). Odd hybrid modes are not coupled since the overlap integral with the even polarised input mode is vanishing. To get an intuition for the output modes in

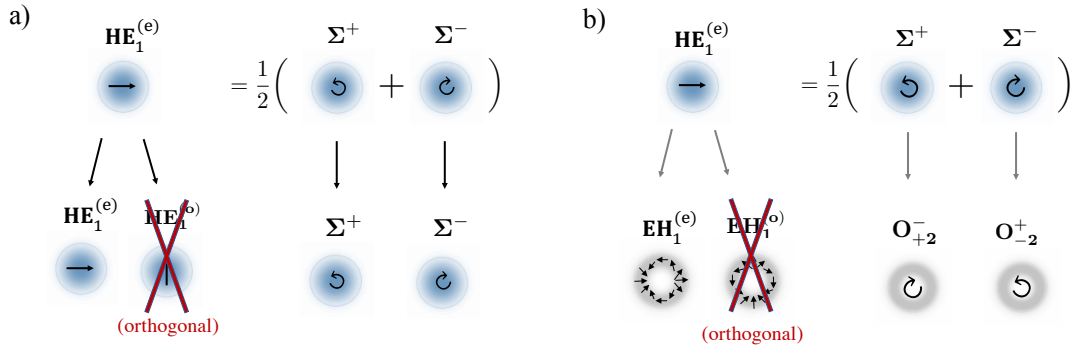

Fig. 3.4 Illustration of the mode coupling without grating, for $m_g = 0$. a) Strong self-coupling with unchanged mode profiles. b) Weak coupling to higher-order modes with spin-orbit-coupling. A coupling to odd modes is not possible due to the orthogonality of input and output modes.

another basis, the hybrid mode is rewritten as a superposition of left- and right-circularly polarised modes, $\mathbf{\Sigma}^+$ and $\mathbf{\Sigma}^-$, respectively. The coupling to the same modes is expected to be stronger than to the second-order OAM modes.

Next, for helical gratings with $m_g > 0$, the coupling process is presented in Fig. 3.5. Only output modes carrying non-zero OAM are considered. By imagining that solely one "part" of the hybrid mode is coupled to the OAM modes, either $\mathbf{\Sigma}^+$ or $\mathbf{\Sigma}^-$, it becomes apparent that the TAM of the coupled OAM modes is not m_g, but $(m_g + 1)$ or $(m_g - 1)$, respectively.

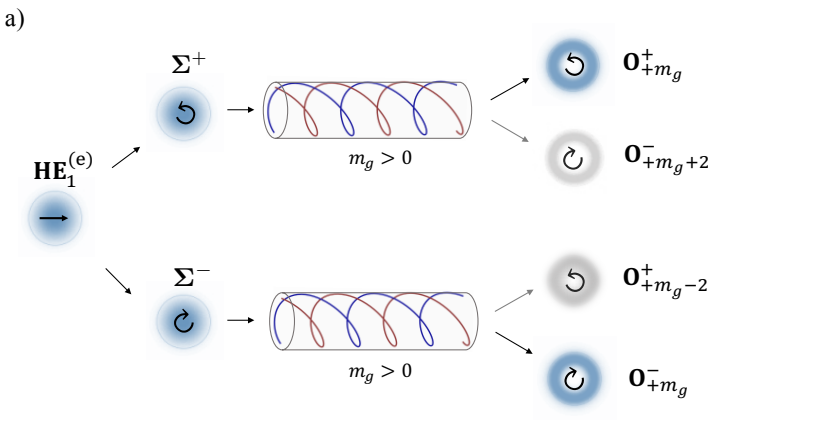

b)

SAM	OAM	TAM
1	m_g	$m_g + 1$
-1	$m_g + 2$	$m_g + 1$
1	$m_g - 2$	$m_g - 1$
-1	m_g	$m_g - 1$

Fig. 3.5 Illustration of the coupling process under the generation of OAM modes with the same TAM, but different SAM and OAM. a) Sketch of the mode profiles before and after the grating. b) List of the angular momenta of the output modes that are written right beside.

Two cases arise: for the (blue-inked) strongly coupled modes, the spin is unchanged and the topological charges are equal to m_g. As the polarisation changes under double in- or decrementation of the OAM order, the coupling is presumably weak.

Returning to Fig. 3.3, we focus on the change of $|\kappa|$ with grating order m_g for different mode classes. The following three paragraphs reveal the main reasons: the modes' degeneracy, the changing of the basis and the varying mode overlap with m_g.

D) Degeneracy To start, the strongly coupled modes of the same basis exhibit identical coupling constants for fixed m_g. Those are written in the same boxes in the figure. For a general grating order m_g, we have:

$$\left|\kappa\Big(\mathbf{HE}_1^{(\mathrm{e})} \to \mathbf{HE}_{|m_g|+1}^{(\mathrm{e/o})}\Big)\right| = \left|\kappa\Big(\mathbf{HE}_1^{(\mathrm{e})} \to \mathbf{EH}_{|m_g|-1}^{(\mathrm{e/o})}\Big)\right| \tag{3.38}$$

and

$$\left|\kappa\Big(\mathbf{HE}_1^{(\mathrm{e})} \to \mathbf{O}_{+m_g}^{+}\Big)\right| = \left|\kappa\Big(\mathbf{HE}_1^{(\mathrm{e})} \to \mathbf{O}_{+m_g}^{-}\Big)\right|. \tag{3.39}$$

The reason for this is that $\mathbf{HE}_{|m_g|+1}^{(\mathrm{e/o})}$ and $\mathbf{EH}_{|m_g|-1}^{(\mathrm{e/o})}$ are degenerate in n_{eff} for the chosen waveguide parameters (i.e. narrow-core with shallow grating with $\varepsilon_{\mathrm{co}} \approx \varepsilon_{\mathrm{cl}}$). Analogously, $|\kappa|$ is the same for OAM modes with different polarisations, since $\mathbf{O}_{\pm|m_g|}^{\pm}$ can be written as a superposition of $\mathbf{HE}_{|m_g|+1}^{(\mathrm{e/o})}$ modes, and $\mathbf{O}_{\pm|m_g|}^{\mp}$ is made up of $\mathbf{EH}_{|m_g|-1}^{(\mathrm{e/o})}$ modes, see Eqs. (2.20a) and (2.20b). The values of the corresponding effective refractive indices are shown in Tab. 3.2. They are in a range of $[n_{\mathrm{cl}}, n_{\mathrm{co}}] = [1.44, 1.45]$. n_{eff} is decreasing with modal order according to the dispersion relation of the waveguide.

E) Basis change The coupling constants for circularly polarised output modes are a factor of $\sqrt{2}$ larger than those corresponding to their associated hybrid modes. It is exemplary highlighted in Fig. 3.3. For instance,

$$\left|\kappa\Big(\mathbf{HE}_1^{(\mathrm{e})} \to \mathbf{O}_{+m_g}^{+}\Big)\right| = \sqrt{2}\ \left|\kappa\Big(\mathbf{HE}_1^{(\mathrm{e})} \to \mathbf{HE}_{m_g+1}^{(\mathrm{e/o})}\Big)\right|. \tag{3.40}$$

An exception is $m_g = 0$, where the coupling constant to the same mode is greater than that to a circularly polarised mode:

$$\left|\kappa\Big(\mathbf{HE}_1^{(\mathrm{e})} \to \mathbf{HE}_1^{(\mathrm{e})}\Big)\right| = \sqrt{2}\ \left|\kappa\Big(\mathbf{HE}_1^{(\mathrm{e})} \to \mathbf{\Sigma}^{\pm}\Big)\right|. \tag{3.41}$$

That leads to the pronounced maximum in the graph. The origin is the associated basis change of the modes. Corresponding derivations can be looked up in App. C.3.

F) Modal overlap Next, the special behaviour of the dotted curves in the figure is considered. Note that the explanation is pointedly kept roughly in terms of the transverse overlap of the modes. To begin with, the graphs are symmetric around $m_g = 0$ since the orders of the coupled HE/EH modes are independent of the grating's handedness, i.e. the sign of m_g; the prediction in Sec. 3.1.2 is checked.

Furthermore, the biggest and the smallest coupling constants are obtained for no grating, where $m_g = 0$. Intuitively, $\kappa\Big(\mathbf{HE}_1^{(\mathrm{e})} \to \mathbf{HE}_1^{(\mathrm{e})}\Big)$ exhibits the largest value because the mode profile is unchanged. $\kappa\Big(\mathbf{HE}_1^{(\mathrm{e})} \to \mathbf{EH}_1^{(\mathrm{e})}\Big)$ is at least one order of magnitude smaller than the coupling constants to other modes, since $\mathbf{HE}_1^{(\mathrm{e})}$ and $\mathbf{EH}_1^{(\mathrm{e})}$ are orthogonal. In detail, the multiplied r- and ϕ-field components cancel out such that only the z-components remain in the coupling integral. (The same holds for output mode $\mathbf{O}_{\pm 2}^{\mp}$ which is made up of $\mathbf{EH}_1^{(\mathrm{e/o})}$ modes.)

Moreover, for $m_g > 0$, an increasing difference between the azimuthal orders of input and output mode is correlated with a decreasing overlap of the transverse profiles. Hence, for the strongly coupled modes, $|\kappa|$ is reducing with modulus grating order $|m_g|$.

For the weakly coupled modes, $|\kappa|$ changes with $|m_g|$ in a different manner; we distinguish between the coupled HE and EH modes including their associated OAM modes. Firstly, for the EH modes, $|\kappa|$ is monotonically rising; i.e. the transverse integrals of the multiplied radial and azimuthal parts of the input/output modes are increasing with $|m_g|$.[3] The reason of the distinct minimum at $m_g = 0$ is that the mentioned overlap integrals of the transverse components are more than two orders of magnitude larger than those of the longitudinal mode components. Secondly, $|\kappa|$ for the HE modes is smaller in comparison to the EH modes.[4]

G) Reflection gratings In the case of reflection gratings, the changing of OAM and SAM of the associated backwards propagating modes must be taken into account, see Sec. 2.2. Hence, the graphs would be mirrored at the ordinate where $m_g = 0$. The absolute values of the coupling constants, $|\kappa|$, remain unchanged for the same coupled modes.

H) Phase matching Lastly, the required grating period for the phase matching of the modes is determined, see Eq. (2.27). The results for Λ_t and Λ_r are listed on the right in the table below.

m_g	Strongly coupled modes				$\beta_2[\frac{1}{\mu\mathrm{m}}]$	n_{eff_2}	$K_\mathrm{t}[\frac{1}{\mathrm{mm}}]$	$\Lambda_\mathrm{t}[\mathrm{mm}]$	$K_\mathrm{r}[\frac{1}{\mu\mathrm{m}}]$	$\Lambda_\mathrm{r}[\mu\mathrm{m}]$
±1	$\mathbf{HE}_2^{(\mathrm{e/o})}$		$\mathbf{O}_{\pm1}^{\pm}$		5.875	1.4493	1.6	3.8	11.752	0.5347
±2	$\mathbf{HE}_3^{(\mathrm{e/o})}$	$\mathbf{EH}_1^{(\mathrm{e/o})}$	$\mathbf{O}_{\pm2}^{\pm}$	$\mathbf{O}_{\pm2}^{\mp}$	5.873	1.4488	3.8	1.7	11.750	0.5348
±3	$\mathbf{HE}_4^{(\mathrm{e/o})}$	$\mathbf{EH}_2^{(\mathrm{e/o})}$	$\mathbf{O}_{\pm3}^{\pm}$	$\mathbf{O}_{\pm3}^{\mp}$	5.870	1.4482	6.4	1.0	11.747	0.5349
±4	$\mathbf{HE}_5^{(\mathrm{e/o})}$	$\mathbf{EH}_3^{(\mathrm{e/o})}$	$\mathbf{O}_{\pm4}^{\pm}$	$\mathbf{O}_{\pm4}^{\mp}$	5.867	1.4474	9.6	0.66	11.744	0.5350

Tab. 3.2 The $\mathbf{HE}_1^{(\mathrm{e})}$ input mode couples strongly with all degenerate modes in the $\mathrm{LP}_{|m_g|}$ group in a spiral grating of order m_g. The wavenumbers β_2 and effective refractive indices n_{eff_2} of all output modes are equal for the same $|m_g|$. The periodic lengths $\Lambda_{\mathrm{t,r}}$ are correlated with the wavevector mismatches $K_{\mathrm{t,r}}$ via $\Lambda_{\mathrm{t,r}} = \frac{2\pi}{K_{\mathrm{t,r}}}$ for transmission or reflection gratings, respectively. The wavenumber of the input mode is $\beta_1 = 5.877\,\frac{1}{\mu\mathrm{m}}$.

The periodic lengths for transmission gratings are in a scale of millimetres; for reflection gratings they are more than three orders of magnitude smaller. Λ_t is decreasing while Λ_r is rising with $|m_g|$ since β_2 is reduced for higher-order modes: The associated wavenumber difference $K_\mathrm{t} = \frac{2\pi}{\Lambda_\mathrm{t}} = \beta_1 - \beta_2$ for transmission gratings is increasing whereas the sum $K_\mathrm{r} = \frac{2\pi}{\Lambda_\mathrm{r}} = \beta_1 + \beta_2$ for reflection gratings is decreasing with $|m_g|$.

The coupling process for another input mode is shown in the next subsection.

[3] Broadly, that implies that the associated "orthogonality" of the EH output modes with the fundamental input mode is decreasing with $|m_g|$.

[4] The reason for this is that

$$\int_0^a \mathrm{d}r\, r \left(e_{1_r}^{\mathrm{HE}}\, e_{m_g-1_r}^{\mathrm{HE}} - e_{1_\phi}^{\mathrm{HE}}\, e_{m_g-1_\phi}^{\mathrm{HE}}\right) < \int_0^a \mathrm{d}r\, r \left(e_{1_r}^{\mathrm{HE}}\, e_{m_g+1_r}^{\mathrm{EH}} + e_{1_\phi}^{\mathrm{HE}}\, e_{m_g+1_\phi}^{\mathrm{EH}}\right), \tag{3.42}$$

according to the solutions of the azimuthal integrals in Sec. 3.1.2. Moreover, $|\kappa|$ is monotonically decreasing with $|m_g|$, if $|m_g| > 2$. The cause is the same as for the strongly coupled modes: a decreasing overlap with modal order difference. However, $|\kappa|$ is for the weakly coupled $\mathbf{HE}_1^{(\mathrm{e/o})}$ mode smaller than for the $\mathbf{HE}_2^{(\mathrm{e/o})}$ mode because of the with n_{eff} associated change of the mode profile. That change is for the chosen waveguide parameters maximum at $|m_g| = 3$.

3.1.3.2 Mode coupling to OAM mode $\mathbf{O}^{+}_{+1}$

The coupling constants for an input mode profile $\mathbf{O}^{+}_{+1}$ are depicted in Fig. 3.3. As derived in Sec. 3.1.2, only half of the considered modes are coupled. (A conversion to other modes is not possible because of the conservation of TAM.)

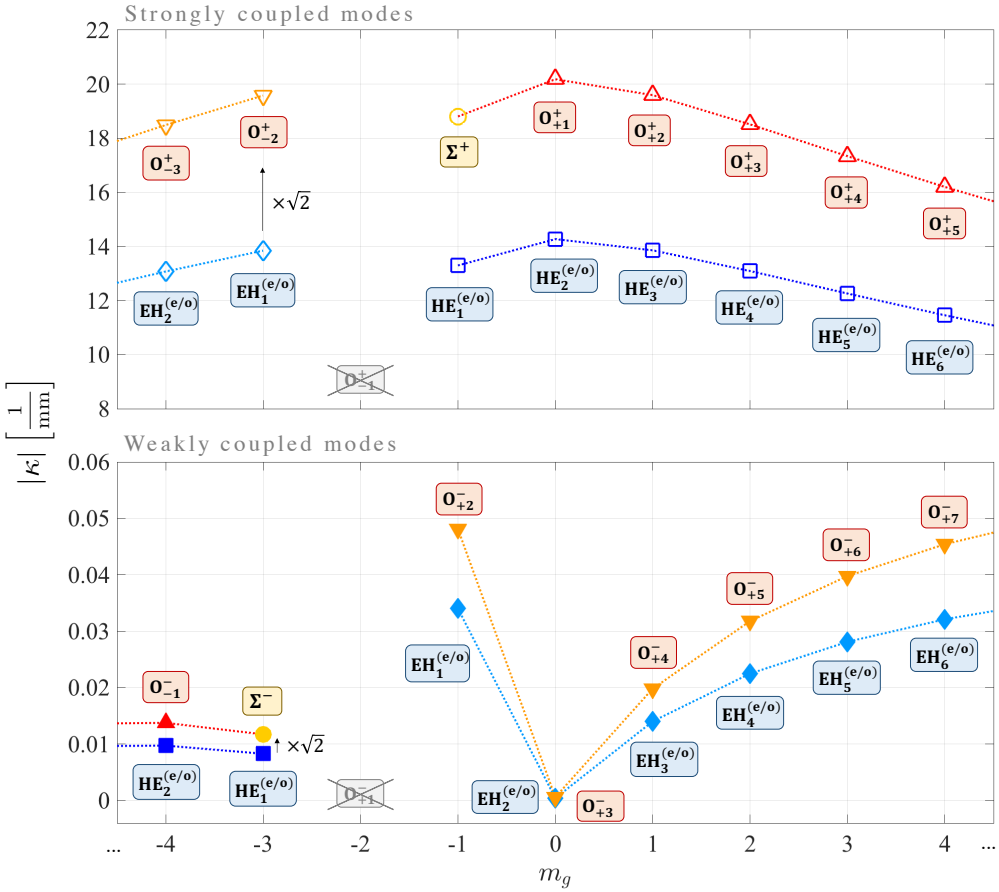

Fig. 3.6 Coupling constants $|\kappa|$ for a coupling between input mode $\mathbf{f}_1 = \mathbf{O}^{+}_{+1}$ to all possible output modes $\mathbf{f}_2$. The labelling is the same as in Fig. 3.3.

In comparison to Fig. 3.3, the order of magnitude of $|\kappa|$ is unchanged. To check, $|\kappa|$ for the strongly coupled $\mathbf{HE}^{(e)}_{1}$ output mode at $m_g = -1$ in Fig. 3.6 exhibits the same value as $|\kappa|$ for the strongly coupled $\mathbf{O}^{+}_{+1}$ output mode at $m_g = 1$ in Fig. 3.3. As well, the degenerate modes are coupled with the same efficiency. Here, though, they are associated with different gratings. For example:

$$\left|\kappa\left(\mathbf{O}^{+}_{+1} \to \mathbf{HE}^{(e/o)}_{3}\right)\right|_{m_g=1} = \left|\kappa\left(\mathbf{O}^{+}_{+1} \to \mathbf{EH}^{(e/o)}_{1}\right)\right|_{m_g=-3} \tag{3.43a}$$

$$\left|\kappa\left(\mathbf{O}^{+}_{+1} \to \mathbf{HE}^{(e/o)}_{4}\right)\right|_{m_g=2} = \left|\kappa\left(\mathbf{O}^{+}_{+1} \to \mathbf{EH}^{(e/o)}_{2}\right)\right|_{m_g=-4} \tag{3.43b}$$

where the subscripts at the absolute-value bars denote the corresponding grating order. (Equivalent equations hold for the associated OAM modes.)

The curve behaviour could be explained in the same manner. For example, maxima and minima are found at $m_g = 0$. There, the $\mathbf{O}^{+}_{+1}$ mode is strongly coupled to itself, and weakly coupled to the $\mathbf{O}^{-}_{+3}$ mode since $\mathbf{HE}^{(\mathrm{e/o})}_{2}$ and $\mathbf{EH}^{(\mathrm{e/o})}_{2}$ are orthogonal. $|\kappa|$ is decreasing with m_g for the strongly coupled modes of the same mode category, since the mode overlap of the interacting modes is decreasing with azimuthal order difference. For the correlated weakly coupled modes, $|\kappa|$ is increasing with m_g because the above mentioned associated "orthogonality" is decreasing. In the depicted range of m_g, we find in the weak-coupling regime a maximum value of $|\kappa| = 4.8 \times 10^{-2}\,\frac{1}{\mathrm{mm}}$ for the generation of a $\mathbf{O}^{-}_{+2}$ mode, i.e.

$$\left|\kappa\left(\mathbf{O}^{+}_{+1} \to \mathbf{O}^{-}_{+2}\right)\right|_{m_g=-1} > \left|\kappa\left(\mathbf{O}^{+}_{+1} \to \mathbf{O}^{-}_{+m_g+3}\right)\right|_{m_g \in [1,4]}. \tag{3.44}$$

This is because the associated $\mathbf{HE}^{(\mathrm{e/o})}_{2}$ mode "anti-overlaps" significantly more with the $\mathbf{EH}^{(\mathrm{e/o})}_{1}$ mode than with EH modes of higher-order.[5] Concluding the discussion of Fig. 3.6, the corresponding grating periods are in the same order of magnitude as those listed in Tab. 3.2 for an HE input mode. Since the same waveguide parameters and pump wavelengths are considered, the effective refractive indices are unchanged for the same degenerate output modes.

For illustration, the mode profiles of the strongly coupled circularly polarised modes are shown in Fig. 3.7. We consider different grating orders m_g.

From top to bottom: firstly, if the input mode is inserted into a grating with right-handed helicity, $m_g > 0$, then the topological charge of the output mode is increased by m_g. Next, if there is exactly one left-handed spiral inscribed in the waveguide, then the OAM of the output mode is zero; left is a circularly polarised mode with the same spin as the input mode. Furthermore, if the order of the grating is with $m_g = -2$ equal to the TAM of the input mode (with changing signs), then no strong mode coupling occurs. This refers to the instability of the $\mathbf{O}^{+}_{-1}$ mode. Lastly, for $m_g \leq 3$, an OAM mode is obtained with reversed handedness of its phase fronts.

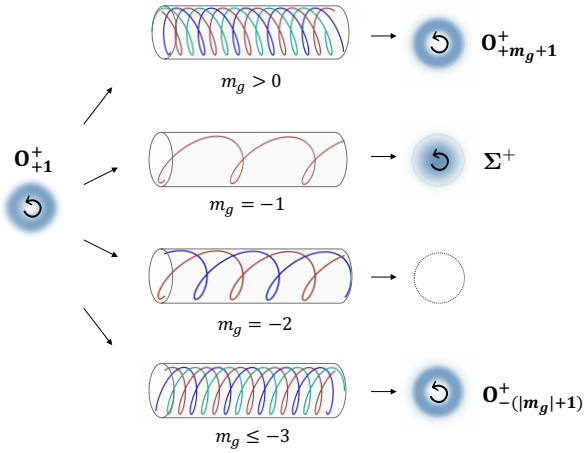

Fig. 3.7 Image showing to which mode profiles the first-order OAM mode is coupled in a helical grating. Different grating orders and handednesses are regarded. The dotted circle for $m_g = -2$ suggests that the modal intensity is zero, no light is transmitted.

Thus, the OAM order can be increased by using helical gratings. To describe entanglement in OAM, we playfully consider inputs with polarisation entanglement.

[5] In this case the radial, the angular and the longitudinal field components of the azimuthal integrals have the same signs such that the components are added in the radial integrals:

$$\int_0^a \mathrm{d}r\, r \left(e^{\mathrm{HE}}_{2_r}\, e^{\mathrm{EH}}_{m_g+2_r} + e^{\mathrm{HE}}_{2_\phi}\, e^{\mathrm{EH}}_{m_g+2_\phi} + e^{\mathrm{HE}}_{2_z}\, e^{\mathrm{EH}}_{m_g+2_z}\right). \tag{3.45}$$

This overlap integral exhibits a minimum at $m_g = 0$ and is crucially increased for $m_g = -1$.

3.1.4 Gedankenexperiment

Imagine a setup as depicted in Fig. 3.8. An external SPDC source produces photon pairs that are entangled in their orthonormal polarisation basis (even and odd). Such photons are then spatially separated (by beam splitters) and inserted into different waveguides: one with a spiral transmission grating and one with a spiral reflection grating.

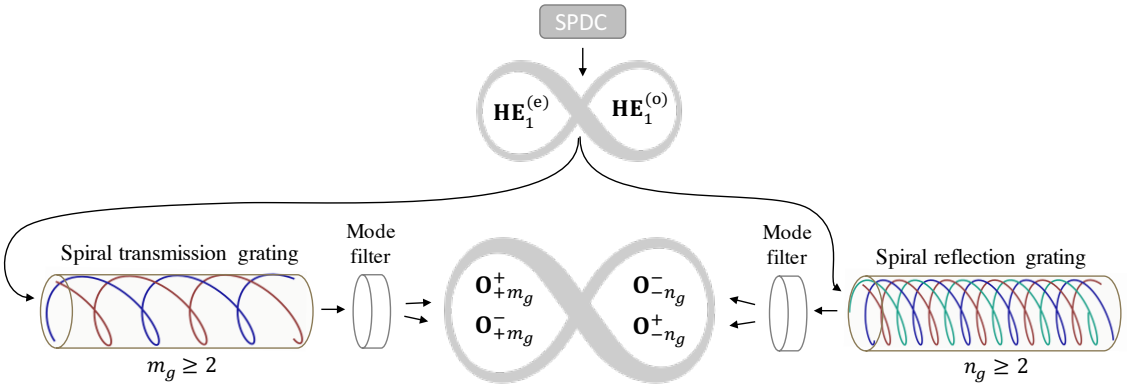

Fig. 3.8 Pictorial setup to transform polarisation entanglement into OAM and path entanglement

The mode profiles of the photons are nearly losslessly transformed into the fundamental waveguide modes $\mathbf{HE}_1^{(e)}$ and $\mathbf{HE}_1^{(o)}$. With the numerical results shown in Sec. 3.1.3, all strongly coupled output modes are known. The polarisation of the input mode has no impact on the coupling. Both modes, $\mathbf{HE}_1^{(e)}$ and $\mathbf{HE}_1^{(o)}$, couple to OAM modes whose topological charges are equal to the number of spirals inscribed in the waveguide ($|m_g|$ and $|n_g|$). Furthermore, the rotation direction of the mode's phase fronts is determined by the handedness of the helical grating structure. If there is more than one spiral ($|m_g|, |n_g| \geq 2$), then the hybrid modes couple to superpositions of left- and right-circularly polarised OAM modes. By using polarisation filters after the waveguides the desired superposition of OAM modes can be extracted. Left are two superpositions of OAM modes whose topological charges are determined by the gratings. One is forwards propagating (transmission grating) and one is backwards propagating (reflection grating).

More details can be seen in the quantum-mechanical approach: the initial photon pairs are described as the Bell state

$$|\psi_{in}\rangle = \frac{1}{\sqrt{2}}\left(|\mathbf{HE}_1^{(e)}\rangle_s\,|\mathbf{HE}_1^{(o)}\rangle_i + |\mathbf{HE}_1^{(o)}\rangle_s\,|\mathbf{HE}_1^{(e)}\rangle_i\right), \tag{3.46}$$

where the indices s, i denote signal and idler modes, respectively.

Analogously, if the rotation directions of the gratings are the same, say m_g, $n_g \geq 2$, then the output state is given by

$$|\psi_{out}\rangle = \frac{1}{\sqrt{2}}\left(|\mathbf{O}^{\zeta}_{+m_g}, \rightarrow\rangle_s\,|\mathbf{O}^{\zeta}_{-n_g}, \leftarrow\rangle_i + |\mathbf{O}^{\zeta}_{-n_g}, \leftarrow\rangle_s\,|\mathbf{O}^{\zeta}_{+m_g}, \rightarrow\rangle_i\right), \tag{3.47}$$

with

$$\mathbf{O}^{\zeta}_{\pm m_g} = \frac{1}{\sqrt{2}}\left(\mathbf{O}^{+}_{\pm m_g} + \mathbf{O}^{-}_{\pm m_g}\right) \tag{3.48}$$

representing superpositions of left- and right-circularly polarised OAM modes. "$\rightarrow$" and

"←" denote forwards or backwards propagation, respectively. As a result, the entanglement in polarisation is converted into entanglement in OAM (m_g, n_g) connected with the direction of propagation. Or in other words: a hyperentangled state in the bases of OAM and spatial direction is generated.

The superposition of modes in Eq. (3.47) can be extracted by the use of polarisation filters after the waveguides. For example, a filtering of modes with positive spins would lead to the output state

$$|\psi^+_{out}\rangle = \frac{1}{2\sqrt{2}} \left(|\mathbf{O}^+_{+m_g}, \rightarrow\rangle_s \, |\mathbf{O}^+_{-n_g}, \leftarrow\rangle_i + |\mathbf{O}^+_{-n_g}, \leftarrow\rangle_s \, |\mathbf{O}^+_{+m_g}, \rightarrow\rangle_i \right). \tag{3.49}$$

Notice that if $m_g = -n_g$, then the output modes have the same topological charges and are not entangled in OAM. Only the entanglement in the direction of propagation would be left.

However, if $m_g = n_g$, then counterpropagating OAM modes with opposite topological charges are generated. This situation is strongly desirable for the realisation of multidimsional quantum-information protocols because the hyperentangled states have a lot of advantages in comparison to one-dimensional entanglement. One important example is superdense teleportation which is impossible in one-dimensional entangled systems [5].

Moreover, by enlarging m_g OAM modes of higher-order are created leading to an increased capacity of information encoding and an enhanced quantum memory and information storage capability [53].

Concluding, the mode-coupling process in helical gratings would have many applications. Nevertheless, the usage of an external photon-pair source requires a bulky setup. The next chapter deals with the more desirable direct generation of entangled states in the waveguide. We decrease the scalability of the setup providing a miniaturisation.

3.2 Four-wave mixing in periodic waveguides

The goal is to obtain counterpropagating photons entangled in their OAM degree of freedom. For this we consider the FWM process depicted in Fig. 3.9 where two pumps, described by $\mathbf{HE}_1^{(e)}$ modes, are inserted into the waveguide core from different sides. The generated modes are the desired entangled OAM modes propagating in opposite directions. To increase the degeneracy between the pump modes and generated modes, different frequencies of the pumps are assumed. Two gratings with different periodic lengths are therefore necessary for an efficient mode-coupling process: each grating frequency separately matches the frequencies of signal and idler photons.

In the following, we derive the generated state in the FWM process in the quantum-mechanical approach and discuss the spectral distribution of the signal and idler photons. The two-photon amplitude is shown for different output modes and the influence of the grating is expounded. We calculate the average number of created photon pairs per pump pulse and thus estimate the efficiency of the process.

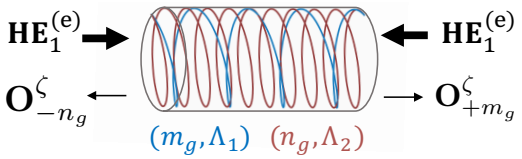

Fig. 3.9 Two $\mathbf{HE}_1^{(e)}$ pump modes generate signal and idler modes in the FWM process. By using helical gratings in the waveguide the modes are coupled to OAM modes. Two right-handed transmission gratings of different orders m_g and n_g and periodic lengths Λ_1 and Λ_2 are considered.

We start with the nonlinear Hamiltonian of the FWM process: [44]

$$\hat{H}_{\mathrm{NL}}(t) = i\,\varepsilon_0 \sum_{\mu\nu\tau\rho} \chi^{(3)}_{\mu\nu\tau\rho} \int_V \mathrm{d}\mathbf{r} \left[\left(E^{(+)}_{p_1}\right)_\mu \left(E^{(+)}_{p_2}\right)_\nu \left(\hat{E}^{(-)}_s\right)_\tau \left(\hat{E}^{(-)}_i\right)_\rho \right] + \mathrm{h.c.}, \tag{3.50}$$

where $\chi^{(3)}_{\mu\nu\tau\rho}$ is the third-order electric susceptibility of a nonlinear material with indices $\mu,\nu,\tau,\rho \in \{r,\phi,z\}$. The subscript $l \in \{p_1,p_2,s,i\}$ of the electric fields denotes the two pumps and the signal and idler modes, respectively (equivalent to the previous mode index $j \in \mathbb{N}$ in Sec. 3.1). The superscripts $(+)$ and $(-)$ indicate each the positive or the negative frequency parts of the electric fields, as in Eq. (3.8). Roughly speaking, it signalises that the pump photons "create" the signal and idler photons in the nonlinear process. Next, the caret $\hat{}$ marks the functions that contain quantum operators; those are the quantum signal and idler fields ($\hat{E}_s$ and $\hat{E}_i$) and thus the Hamiltonian $\hat{H}_{\mathrm{NL}}$. The fields are integrated over the effective volume $V = L\,\pi\,a^2$ of the waveguide where L is its length and a the core radius. h.c. denotes the Hermitian conjugated term.

The electric fields are described one after another. Firstly, $\mathbf{E}_{p_1}$ and $\mathbf{E}_{p_2}$ are treated as non-depleted classical fields:

$$\mathbf{E}_{p_1} = E_0\,\mathbf{HE}_1^{(e)}(r,\phi)\,e^{i(\beta_1 z - \bar{\omega}_1 t)} + \mathrm{h.c.}, \tag{3.51a}$$

$$\mathbf{E}_{p_2} = E_0\,\mathbf{HE}_1^{(e)}(r,\phi)\,e^{-i(\beta_2 z + \bar{\omega}_2 t)} + \mathrm{h.c.}. \tag{3.51b}$$

E_0 is the field amplitude associated with a typical laser power of $P = 100\,\mu\mathrm{W}$ by $P = \frac{c\,\bar{n}_{\mathrm{eff}}\,\varepsilon_0\,\pi\,r_p^2\,E_0^2}{2}$ where $\bar{n}_{\mathrm{eff}}$ is the average n_{eff} and $r_p = 200\,\mu\mathrm{m}$ is the FWHM of the pump pulses. The profiles are the fundamental waveguide mode $\mathbf{HE}_1^{(e)}$. The first pump is forwards propagating with wavenumber β_1, the second backwards with β_2. Note that $\bar{\omega}_1$ and $\bar{\omega}_2$ are the central frequencies of the modes, any spectral distribution is neglected.

In comparison, the signal and idler fields

$$\hat{\mathbf{E}}_s = \mathcal{N}_s \, a_s(z) \, \mathbf{O}^{\pm}_{\pm m_s}(r,\phi) \int \mathrm{d}\omega_s \left[e^{i(\beta_s(\omega_s) z - \omega_s t)} \, \hat{b}_s(\omega_s) \right] + \text{h.c.} \tag{3.52a}$$

$$\hat{\mathbf{E}}_i = \mathcal{N}_i \, a_i(z) \, \mathbf{O}^{\pm}_{\pm m_i}(r,\phi) \int \mathrm{d}\omega_i \left[e^{-i(\beta_i(\omega_i) z + \omega_i t)} \, \hat{b}_i(\omega_i) \right] + \text{h.c.} \tag{3.52b}$$

are described quantum mechanically using bosonic annihilation and creation operators, $\hat{b}_{s,i}$ and $\hat{b}^\dagger_{s,i}$, respectively [54]. We choose that the signal mode is forwards propagating and the idler backwards. The phase fronts are either left- or right-handed as the signs of the topological charges can be positive or negative. Independently, the modes are either left- or right-circularly polarised, indicated by the upper coloured $\pm$ signs of the OAM modes. The amplitudes (a_s and a_i) and the transverse profiles are outside the integrals because they vary with frequency much less in comparison with the exponential functions. It is thus reasonable to evaluate them at the corresponding central frequencies $\bar{\omega}_s$ and $\bar{\omega}_i$. The normalisation constant

$$\mathcal{N}_{s,i} = \sqrt{\frac{\hbar \bar{\omega}_{s,i}}{2 \, \varepsilon_0 \, c^2 \, n_{\mathrm{eff}_{s,i}}(\bar{\omega}_{s,i}) \, V}} \tag{3.53}$$

is evaluated at $\bar{\omega}_s$ and $\bar{\omega}_i$ as well under the assumption of small spectral bandwidths.

With the electric fields in Eqs. (3.51) and (3.52) the nonlinear Hamiltonian $\hat{H}_{\mathrm{NL}}(t)$ in Eq. (3.50) is determined. The generated state $|\psi_{\mathrm{gen}}\rangle$ from the FWM process is given by Eq. (3.54a) in the limit of a low probability of pair production per pulse. $|0\rangle_s$ and $|0\rangle_i$ are the vacuum states of the signal and idler modes, respectively.

$$\begin{aligned}
&|\psi_{\mathrm{gen}}\rangle \\
&\quad = \frac{1}{i\hbar} \int_{-\infty}^{\infty} \mathrm{d}t \; \hat{H}_{\mathrm{NL}}(t) \; |0\rangle_s \, |0\rangle_i && \text{(3.54a)} \\
&\quad = \Gamma \iint \mathrm{d}\omega_s \, \mathrm{d}\omega_i \; \Phi(\omega_s, \omega_i) \; \delta(\bar{\omega}_1 + \bar{\omega}_2 - \omega_s - \omega_i) \; \hat{b}^\dagger_s(\omega_s) \; \hat{b}^\dagger_i(\omega_i) \; |0\rangle_s \, |0\rangle_i + \text{h.c.} && \text{(3.54b)} \\
&\quad = \Gamma \int \mathrm{d}\omega_s \; \Phi(\omega_s, \tilde{\omega}_i) \; \hat{b}^\dagger_s(\omega_s) \; \hat{b}^\dagger_i(\tilde{\omega}_i) \; |0\rangle_s \, |0\rangle_i + \text{h.c.} && \text{(3.54c)}
\end{aligned}$$

The substitution of the Hamiltonian (3.50) yields Eq. (3.54b). On the right side the bosonic creation operators of the signal and idler fields are rediscovered. As they act on the vacuum states, single-photon states are created at the frequencies they depend on, ω_s and ω_i, respectively. In the middle, the Dirac-delta function δ arises from the time integral in Eq. (3.54a):

$$\int_{-\infty}^{\infty} \mathrm{d}t \; e^{-i(\bar{\omega}_1 + \bar{\omega}_2 - \omega_s - \omega_i)t} = 2\pi \, \delta(\bar{\omega}_1 + \bar{\omega}_2 - \omega_s - \omega_i), \tag{3.55}$$

which signifies energy conservation as discussed in Sec. 2.4. The signal and idler frequencies are therefore interdependent; ω_i is fixed by ω_s via

$$\tilde{\omega}_i = \bar{\omega}_1 + \bar{\omega}_2 - \omega_s \tag{3.56}$$

or vice versa. The integral over ω_i is erased in Eq. (3.54c). (We further omit the tilde sign above ω_i for simplification.)

Next, the prefactor

$$\Gamma = \frac{\pi E_0^2}{c^2\, V} \sqrt{\frac{\bar{\omega}_s\ \bar{\omega}_i}{n_{\mathrm{eff}_s}(\bar{\omega}_s)\ n_{\mathrm{eff}_i}(\bar{\omega}_i)}}\ \Upsilon_{\mathrm{NL}} \tag{3.57}$$

collects the normalisation constants from the generated fields, see Eq. (3.53), and includes the pump-field amplitudes E_0 in Eq. (3.52). Additionally, it comprises

$$\Upsilon_{\mathrm{NL}} = \sum_{\mu\nu\tau\rho} \chi^{(3)}_{\mu\nu\tau\rho}\, I_{\mu\nu\tau\rho} \tag{3.58}$$

representing the summed integrals over the transverse plane, $I_{\mu\nu\tau\rho}$, weighted by the components of the third-order susceptibility tensor $\chi^{(3)}_{\mu\nu\tau\rho}$.[6] We recover the transverse profiles of all four fields:

$$I_{\mu\nu\tau\rho} = \int_0^\infty \mathrm{d}r\, r \int_0^{2\pi} \mathrm{d}\phi\ \left[\left(\mathrm{HE}_1^{(\mathrm{e})}\right)_\mu \left(\mathrm{HE}_1^{(\mathrm{e})}\right)_\nu \left(\mathrm{O}^{\pm}_{\pm m_s}\right)^*_\tau \left(\mathrm{O}^{\pm}_{\pm m_i}\right)^*_\rho\right]. \tag{3.59}$$

Remember that different colours for the spins of the OAM modes represent their independence; all four combination possibilities "++", "+−", "−+", and "−−" are possible. The topological charges are not correlated as well.

The only remaining term in Eq. (3.54c) is the joint-spectral amplitude (JSA) $\Phi(\omega_s, \omega_i)$. This is the probability amplitude that signal and idler photons are created with frequencies ω_s and ω_i, respectively. Here, the JSA consists of the z-integral

$$\Phi(\omega_s, \omega_i) = \int_0^L \mathrm{d}z\ (a_s(z))^*\, (a_i(z))^*\, e^{i\Delta\beta(\omega_s,\omega_i)z} \tag{3.60}$$

which comprises the conjugated amplitudes of the signal and idler modes $a_s(z)$ and $a_i(z)$, respectively, and particularly depends on the wavevector mismatch of the four modes:

$$\Delta\beta(\omega_s, \omega_i) = (\beta_1 - \beta_2) - (\beta_s(\omega_s) - \beta_i(\omega_i)). \tag{3.61}$$

Additional brackets highlight that each modal pair is counterpropagating, i.e. the β's have different signs. (The dependency of $\beta_{1,2}$ on $\bar{\omega}_{1,2}$ is not shown for clearness.) Since the JSA can not be factorised into two separate functions of ω_s and ω_i, the photons are said to have spectral entanglement.

We continue with a derivation of $\Phi(\omega_s, \omega_i)$ to examine the spectral distribution of the modes. First, the mode amplitudes $a_s(z)$ and $a_i(z)$ are given by the solutions of the coupled-mode equations in Eq. (3.17). For the forwards propagating signal, the previous boundary conditions of the input and output modes are applied: $\tilde{a}_1(0) = 1$ and $\tilde{a}_2(0) = 0$ by reminding of Tab. 3.1 in Sec. 3.1.1. For the counterpropagating idler we have analogously: $\tilde{a}_1(L) = 1$ and $\tilde{a}_2(L) = 0$.[7] The solutions of the output modes are for $d = 0$ the amplitudes of the signal and idler modes:

$$a_s(z) = \frac{|\kappa|}{\gamma_t} \sin(\gamma_t z), \tag{3.62a}$$

$$a_i(z) = \frac{|\kappa|}{\gamma_t} \sin(\gamma_t (z - L)), \tag{3.62b}$$

[6] The sum can be excluded in that manner, since the mode profile is the only vectorial part of the electric fields.

[7] Note that the indices 1, 2 correspond to the previous notation of the input/output modes in Sec. 3.1.1. They are not associated with the pumps labelled with the same indices.

where κ is the coupling constant between the fundamental input modes $\mathbf{HE}_1^{(e)}$ and the OAM output modes $\mathbf{O}^{\pm}_{\pm m_s}$ and $\mathbf{O}^{\pm}_{\pm m_i}$. Assuming a right-handed helical grating of order m_g for the signal and n_g for the idler, we know from Sec. 3.1.3.1 that an $\mathbf{HE}_1^{(e)}$ mode couples strongly with a forwards propagating signal $\mathbf{O}^{\pm}_{+m_g}$ mode and with a backwards propagating idler $\mathbf{O}^{\pm}_{-n_g}$ mode, see the ansatz of the electric fields in Eq. (3.52). In the following consideration we set $m_g = n_g$ and suppose that the modes with different spins are coupled with the same efficiency, treating their basis modes $\mathbf{HE}^{(e/o)}_{m_g+1}$ and $\mathbf{EH}^{(e/o)}_{m_g-1}$ as degenerate.

To phase match the modes, the wavenumber mismatch in Eq. (3.61) must be vanishing: $\Delta\beta(\omega_s, \omega_i) = 0$. For fixed pump frequencies $\bar{\omega}_1$ and $\bar{\omega}_2$ this is only given for specific generated frequencies ω_s and ω_i according to the dispersion relation of the signal/idler modes. Since ω_s and ω_i are correlated with Eq. (3.56) we express both in terms of the frequency difference $\Delta\omega = \omega_s - \bar{\omega}_1 = \bar{\omega}_2 - \omega_i$, see Fig. 2.5 a) for illustration. In such a way we can vary both generated frequencies by using only one variable.

Some exemplary curves are shown in Fig. 3.10 on the left. We see how $\Delta\beta$ varies with $\Delta\omega$ for different signal/idler modes.[8] Without grating, $m_g = 0$, those are equal to the unchanged pump profiles, the fundamental hybrid modes. We have $\Delta\beta = 0$ for $\Delta\omega = 0$ with Eq. (3.61) since $\beta_1(\bar{\omega}_1) = \beta_s(\omega_s)$ and $\beta_2(\bar{\omega}_2) = \beta_i(\omega_i)$. All modes are described by the same dispersion relation. Next, for $m_g = 3$, the associated generated OAM modes exhibit at $\Delta\beta = 0$ the marked frequency detuning of $\Delta\omega = 0.43\,\mathrm{THz}$ from the pump frequencies. For $m_g = 6$, $\Delta\omega = 1.1\,\mathrm{THz}$ is found.

Note that the detuning does not scale linearly with m_g, it depends on the dispersion relation of the modes: their effective refractive indices - and thus their propagation constants β - are progressively decreasing with modal order for a fixed V-number, see Sec. 2.1.

To further enlarge $\Delta\omega$, the waveguide parameters and the pump wavelengths can be varied. The latter determine the order of magnitude of $\Delta\omega$. For example, by decreasing the pump wavelength difference from 1.05 µm to 0.10 µm, the frequency shift is strikingly reduced: $\Delta\omega = 3.6 \times 10^{-2}\,\mathrm{THz}$ for $\mathbf{O}^{\pm}_{\pm 3}$, or $\Delta\omega = 9.5 \times 10^{-2}\,\mathrm{THz}$ for $\mathbf{O}^{\pm}_{\pm 6}$ at $\Delta\beta = 0$; assuming $\lambda_1 = 1.5\,\mu\mathrm{m}$ and $\lambda_2 = 1.6\,\mu\mathrm{m}$.

Moreover, the refractive index of the waveguide core could be moderately scaled up from the previous 1.45 to 1.50. The V-number is then optimised for an OAM mode of the sixth order. (A further increase of n_{co} would cause the detuning to drop again.) As a result, the frequency shift is slightly increased for all $m_g \neq 0$: for the OAM modes $\mathbf{O}^{\pm}_{\pm 3}$, $\Delta\omega(\Delta\beta = 0)$ rises by $2.1 \times 10^{-2}\,\mathrm{THz}$; for $\mathbf{O}^{\pm}_{\pm 6}$ by $6.4 \times 10^{-2}\,\mathrm{THz}$. The latter is shown by the blue-dashed curve on the left in Fig. 3.9.[9] However, an increased refractive-index change between the core and the cladding of the waveguide does not change the order of magnitude of the frequency shift. [10] Therefore, $n_{\mathrm{co}} = 1.50$ is not further considered and we return to a shallow grating with $n_{\mathrm{co}} = 1.45$ and $n_{\mathrm{cl}} = 1.44$.

For those the modulus squared JSA, $|\Phi(\omega_s, \omega_i)|^2$, is calculated according to Eqs. (3.60), (3.61) and (3.62b). The result is depicted on the right in Fig. 3.10. Note that a compa-

[8] Note that although $\Delta\beta$ seems to scale linearly with $\Delta\omega$, there is actually a slight curvature due to the dispersion of the modes in the grating. Besides, $\Delta\beta(\omega_s, \omega_i) = \beta_1 - \beta_2 - \beta_s(\omega_s) + \beta_i(\omega_i)$ is not increasing but decreasing with $\Delta\omega$, because $\omega_s = \bar{\omega}_1 + \Delta\omega$ and thus $\beta_s(\omega_s)$ are rising while, analogously. $\beta_i(\omega_i)$ is monotonically dropping with $\Delta\omega$.

[9] Corresponding curves for $\mathbf{HE}_1^{(e/o)}$ and $\mathbf{O}^{\pm}_{\pm 3}$ would be almost not distinguishable from the solid lines.

[10] Note that the V-number is positively correlated with the maximal possible topological charge m_{max} of the OAM mode. In a narrow-core waveguide with $n_{\mathrm{co}} = 1.45$ we find $m_{\mathrm{max}} = 10$, leading to $\Delta\omega(\Delta\beta = 0) = 2.4\,\mathrm{THz}$. At $n_{\mathrm{co}} = 1.50$, $m_{\mathrm{max}} = 28$ with $\Delta\omega = 15\,\mathrm{THz}$. In practice, OAM modes of that order are unstable because of inter-modal crosstalk. [19]

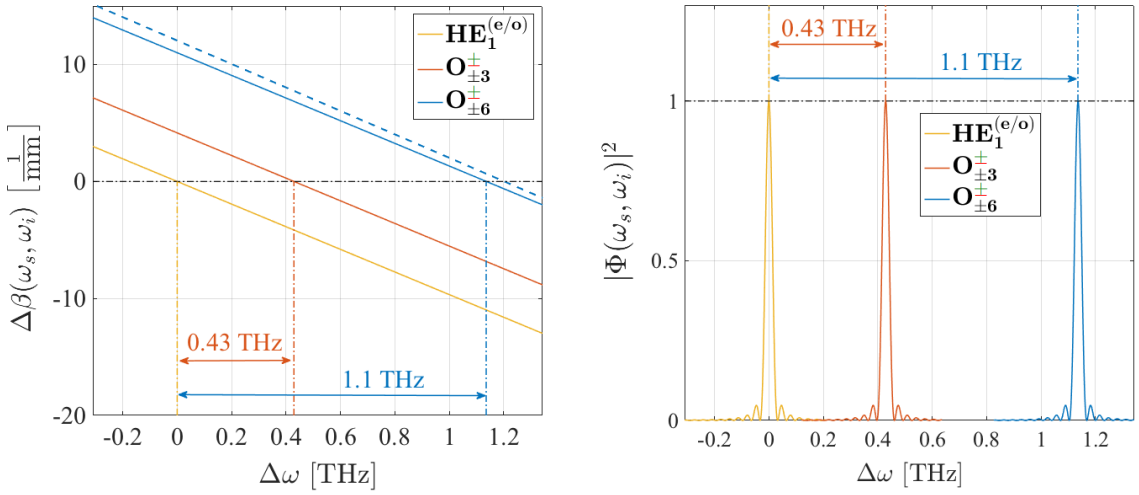

Fig. 3.10 Left: wavenumber difference $\Delta\beta(\omega_s, \omega_i)$ of the four interacting modes for varying frequency detuning $\Delta\omega$ between the pumps and the generated modes. Different colours mark the signal/idler modes. Those correspond to gratings characterised by $m_g = 0$ (yellow), $m_g = 3$ (red) and $m_g = 6$ (blue). Note that the OAM modes denote all four combination possibilities of OAM and SAM handednesses since their basis modes are treated as degenerate. Right: modulus squared JSA $|\Phi(\omega_s, \omega_i)|^2$ in a.u. against $\Delta\omega$ for the same modes and associated grating orders. Its maximum value is normalised to 1. Coupling parameters are $\kappa = 10\,\frac{1}{\text{mm}}$ and $L = 15\,\text{mm}$, notably equal for all modes. In both plots, two different pump wavelengths are considered with $\lambda_1 = 1.55\,\mu\text{m}$ and $\lambda_2 = 0.5\,\mu\text{m}$. For the solid-line plots, the waveguide characteristics are the same as in Sec. 3.1: We assume a low-contrast waveguide with refractive indices $n_{\text{co}} = 1.45$ and $n_{\text{cl}} = 1.44$ in a shallow grating of $\Delta n_0 = 1.0 \times 10^{-2}$. The waveguiding core is narrow with radius $a = 20\,\mu\text{m}$. The impact of an increased core index of $n_{\text{co}} = 1.50$ on $\Delta\beta$ for $m_g = 6$ is shown by the blue-dashed curve in the left plot.

rably large coupling parameter is chosen with $\kappa L = 150$. $|\Phi(\omega_s, \omega_i)|^2$ exhibits pronounced maxima at the frequency detunings where $\Delta\beta(\omega_s, \omega_i) = 0$. It is equally sinc-shaped for all output modes as identical coupling constants are assumed.

Choosing smaller coupling constants yields side-peaks of equal strength at $\Delta\beta = \pm 2\kappa$ in the observed frequency range, see Fig. 3.11. This is due to two additional sinc functions the JSA consists of:

$$\Phi \propto \Phi_{\text{NL}} - \Phi_g, \tag{3.63}$$

where

$$\Phi_{\text{NL}} = 2\cos(\kappa L)\,\text{sinc}\left[\frac{\Delta\beta\, L}{2}\right], \tag{3.64a}$$

$$\Phi_g = e^{i\frac{\Delta\beta L}{2}}\,\text{sinc}\left[\frac{(\Delta\beta + 2\kappa)L}{2}\right] + e^{-i\frac{\Delta\beta L}{2}}\,\text{sinc}\left[\frac{(\Delta\beta - 2\kappa)L}{2}\right]. \tag{3.64b}$$

$\Phi_{\text{NL}} \propto \cos(\kappa L)$ leads to fast oscillations of the nonlinear JSA with respect to κ if $L \gg \frac{\pi}{\kappa}$. This is crucial because $\kappa \propto \Delta\varepsilon_0$ is correlated with imperfections of the waveguide structure. In Fig. 3.11 it can be seen that for $\kappa = 1\,\frac{1}{\text{mm}}$ the central peak is greater than the sideband peaks. For $\kappa = 2\,\frac{1}{\text{mm}}$ the central peak is suppressed. These oscillations can be stabilised by the use of shorter waveguides of length $L \ll \frac{\pi}{\kappa}$.

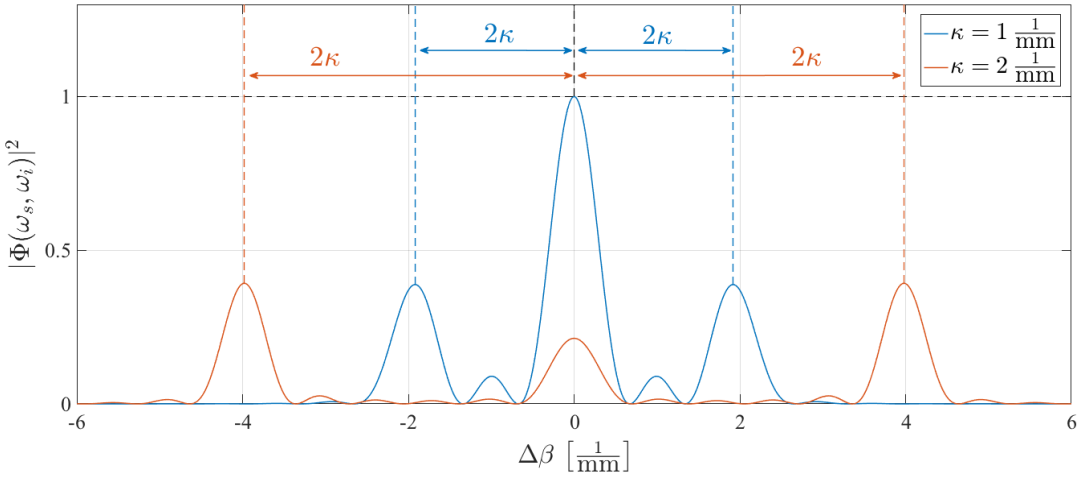

Fig. 3.11 JSA $|\Phi(\omega_s, \omega_i)|^2$ in a.u. against the wavenumber difference $\Delta\beta(\omega_s, \omega_i)$ for different κ where $L = 10\,\mathrm{mm}$. Note that the dependency of the mode profiles as in Fig. 3.10 sits the mode's dispersion relation which connects $\Delta\beta$ with $\Delta\omega$. For $\kappa = 1\,\frac{1}{\mathrm{mm}}$, $|\Phi(\omega_s, \omega_i)|^2$ is normalised to 1 for its maximum value at $\Delta\beta = 0$. To facilitate comparison, the same normalisation of $|\Phi(\omega_s, \omega_i)|^2$ is applied for the red-coloured plot corresponding to $\kappa = 2\,\frac{1}{\mathrm{mm}}$.

An interference of the sinc functions leads to a small shift of the sidelobes as they are not exactly at $\Delta\beta = \pm 2\kappa$. If $\kappa \gg \Delta\beta$, then the side-peaks are highly separated and no interference of the sinc functions needs to be taken into account.[11] However, κ does not drastically effect the height of the sidelobes of $|\Phi(\omega_s, \omega_i)|^2$ in the inspected order of magnitude. (The sinc functions are in that sense sufficiently separated for the chosen parameters.)

In summary, a complete modification of the JSA is possible with spectral dispersion engineering. By changing κ the sideband peaks can be shifted and the central peak suppressed.

Next, the average number of photon pairs per pump pulse N_{pairs} is derived:

$$N_{\mathrm{pairs}} = \langle \psi_{\mathrm{gen}} | \psi_{\mathrm{gen}} \rangle = |\Gamma|^2 \int \mathrm{d}\omega_s \ |\Phi(\omega_s, \omega_i)|^2 \tag{3.65}$$

is given by the generated state $|\psi_{\mathrm{gen}}\rangle$ defined in Eq. (3.54). To determine $\Gamma \propto \Upsilon_{\mathrm{NL}}$ (see Eqs. (3.57) to (3.59)), the transverse integrals $I_{\mu\nu\tau\rho}$ are solved. As in Sec. 3.1, the mode profiles are written in terms of their radial and azimuthal field parts such that the transverse integrals can be separated:

$$I_{\mu\nu\tau\rho} = \int_0^\infty \mathrm{d}r\, r \int_0^{2\pi} \mathrm{d}\phi \, \left(\mathrm{HE}_1^{(\mathrm{e})}\right)_\mu \left(\mathrm{HE}_1^{(\mathrm{e})}\right)_\nu \left(\mathrm{O}^{\pm}_{+m_g}\right)^*_\tau \left(\mathrm{O}^{\mp}_{-m_g}\right)^*_\rho \tag{3.66a}$$

$$= \int_0^\infty \mathrm{d}r\, r \, \left(e_1^{\mathrm{HE}}\right)_\mu \left(e_1^{\mathrm{HE}}\right)_\nu \left(e^{\mathrm{HE/EH}}_{m_g \pm 1}\right)^*_\tau \left(e^{\mathrm{HE/EH}}_{m_g \pm 1}\right)^*_\rho$$
$$\times \int_0^{2\pi} \mathrm{d}\phi \, \left(g_1^{(\mathrm{e})}\right)_\mu \left(g_1^{(\mathrm{e})}\right)_\nu \left(g^{(+)}_{m_g \pm 1}\right)^*_\tau \left(g^{(-)}_{m_g \pm 1}\right)^*_\rho \tag{3.66b}$$

in virtue of Eqs. (2.15) and (2.20).

[11] This was the case in Fig. 3.10, where the sidelobes are not visible in the depicted range of $\Delta\omega$.

The radial integrals are determined numerically.[12] For the same modes the radial integrals with only transverse field components ($\mu, \nu, \rho, \tau \in \{ r, \phi \}$) are in the same order of magnitude. The integrals containing one or more longitudinal components of the electric fields are at least two orders of magnitudes less and are neglected. How the radial overlap changes for different mode combinations is explained later.

First, the analytical calculation of the azimuthal integral in Eq. (3.66b) is presented. The "$rrrr$"-component yields for example:

$$\int_0^{2\pi} \mathrm{d}\phi \, \left(g_1^{(\mathrm{e})}\right)_r \left(g_1^{(\mathrm{e})}\right)_r \left(g_{m_g \pm 1}^{(+)}\right)_r^* \left(g_{m_g \pm 1}^{(-)}\right)_r^* \tag{3.67a}$$

$$= \int_0^{2\pi} \mathrm{d}\phi \, \cos^2(\phi) \, e^{-i(m_g \pm 1)\phi} \, e^{i(m_g \pm 1)\phi} \tag{3.67b}$$

$$= \begin{cases} \pi & \text{, for "}+\,+\text{" } \vee \text{ "}-\,-\text{" (different spins)} \\ \frac{\pi}{2} & \text{, for "}+\,-\text{" } \vee \text{ "}-\,+\text{" (same spins)} \end{cases} \tag{3.67c}$$

under the use of Eqs. (2.18) and (2.10). The general solution is $\forall\, \mu, \nu, \tau, \rho \in \{ r, \phi \}$:

$$\int_0^{2\pi} \mathrm{d}\phi \, \left(g_1^{(\mathrm{e})}\right)_\mu \left(g_1^{(\mathrm{e})}\right)_\nu \left(g_{m_g \pm 1}^{(+)}\right)_\tau^* \left(g_{m_g \pm 1}^{(-)}\right)_\rho^* = \begin{cases} \begin{cases} \pi, \text{ if } \mu = \nu \\ 0, \text{ if } \mu \neq \nu \end{cases} & \text{(different spins)} \\ \frac{\pi}{2} & \text{(same spins)} \end{cases} . \tag{3.68}$$

In the first case, if the spins of the generated OAM modes are different, then the azimuthal integrals are zero as each one r- and one ϕ-component of the $\mathbf{HE}_1^{(\mathrm{e})}$ modes are considered. All other azimuthal integrals are non-vanishing - or more specifically - have equal solutions, π or $\frac{\pi}{2}$, depending on the spins of the generated OAM modes.

With the solutions of transverse integrals $I_{\mu\nu\tau\rho}$ the only remaining parameter for the calculation of Υ_{NL} is the third-order susceptibility tensor, see Eq. (3.58). $\chi^{(3)}$ is estimated for a material with isotropic symmetry such as SiO_2. The tensor is typically given in Cartesian coordinates exhibiting the following eight interdependent dominant components:

$$\chi^{(3)}_{xxxx} = \chi^{(3)}_{yyyy} = 3\chi^{(3)}_{xxyy} = 3\chi^{(3)}_{yyxx} = 3\chi^{(3)}_{xyxy} = 3\chi^{(3)}_{yxyx} = 3\chi^{(3)}_{xyyx} = 3\chi^{(3)}_{xyyx} \approx 3 \times 10^{-22} \, \frac{\mathrm{m}^2}{\mathrm{V}^2}. \tag{3.69}$$

The tensor is in the considered orthonormal cylindrical coordinate system the same as in Cartesian coordinates; substituting $x \to r$ and $y \to \phi$ or vice versa. [55]

[12] For further analytical investigation one could exploit the weakly-guiding approximation: the s-parameter from Eq. (2.17) becomes $s_{p_1} = s_{p_2} = -1$ for the HE pumps. The values of s for the signal and idler modes depend on their associated basis modes, i.e. whether their OAM and SAM of the generated modes are co- or counterrotating, see Eq. (2.20). Exploiting this substitution the algebraic simplification of the radial integrals can be done in a similar manner as the derivation of the overlap integrals between the coupled input and output modes in Sec. 3.1.2.

The resulting average numbers of generated photon pairs per pump pulse, N_{pairs} from Eq. (3.65), are shown in Tab. 3.3. As a matter of principle, the FWM effect is assumed to be very weak since $N_{\text{pairs}} \ll 1$.

	N_{pairs}	
Generated OAM modes	$m_g = 3$	$m_g = 6$
$\mathbf{O}^{+}_{+m_g}\,\mathbf{O}^{-}_{-m_g}$	8.2×10^{-10}	3.5×10^{-11}
$\mathbf{O}^{-}_{+m_g}\,\mathbf{O}^{+}_{-m_g}$	2.7×10^{-9}	4.7×10^{-10}
$\mathbf{O}^{+}_{+m_g}\,\mathbf{O}^{+}_{-m_g}$	3.5×10^{-17}	2.7×10^{-17}
$\mathbf{O}^{-}_{+m_g}\,\mathbf{O}^{-}_{-m_g}$	6.7×10^{-15}	4.3×10^{-15}

Tab. 3.3 Average number of generated photon pairs per pulse N_{pairs} for different signal and idler modes with topological charges $m_g = 3$ and $m_g = 6$. Fixed parameters are coupling constant $\kappa = 1\,\frac{1}{\text{cm}}$, waveguide length $L = 1\,\text{cm}$, laser-pump power $P = 100\,\mu\text{W}$, laser-pump FWHM $r_p = 200\,\mu\text{m}$, pump wavelengths $\lambda_{p_1} = 1.55\,\mu\text{m}$ and $\lambda_{p_2} = 0.5\,\mu\text{m}$ and waveguide characteristics $n_{\text{co}} = 1.45$, $n_{\text{co}} = 1.44$ and $a = 20\,\mu\text{m}$ with a dominant component of the third-order susceptibility tensor of $\chi^{(3)}_{xxxx} = 3 \times 10^{-22}\,\frac{\text{m}^2}{\text{V}^2}$.

N_{pairs} depends on the spins of the generated OAM modes because the spatial profiles of the associated hybrid modes differ: $\mathbf{O}^{\pm}_{\pm m_g} = \mathbf{HE}^{(\text{e})}_{m_g+1} \pm i\mathbf{HE}^{(\text{o})}_{m_g+1}$ while $\mathbf{O}^{\mp}_{\pm m_g} = \mathbf{EH}^{(\text{e})}_{m_g-1} \pm i\mathbf{EH}^{(\text{o})}_{m_g-1}$, see Eq. (2.20). Looking at the mode combinations shown in the first and the second row of Tab. 3.3 where the angular moments of the OAM modes, SAM and OAM, are both co- or counterrotating, all radial overlap integrals are positive:

$$\int_0^\infty \mathrm{d}r\, r \left(\mathrm{HE}_1^{(\text{e})}\right)_\mu \left(\mathrm{HE}_1^{(\text{e})}\right)_\nu \left(\mathrm{O}^{\pm}_{+m_s}\right)^*_\tau \left(\mathrm{O}^{\mp}_{-m_i}\right)^*_\rho > 0. \tag{3.70}$$

For the modes depicted in the last two rows of Tab. 3.3, the radial overlaps of the modes possess opposite signs for different components, for example

$$\int_0^\infty \mathrm{d}r\, r \left(\mathrm{HE}_1^{(\text{e})}\right)_r \left(\mathrm{HE}_1^{(\text{e})}\right)_r \left(\mathrm{O}^{\pm}_{+m_s}\right)^*_r \left(\mathrm{O}^{\pm}_{-m_i}\right)^*_r > 0, \tag{3.71a}$$

$$\int_0^\infty \mathrm{d}r\, r \left(\mathrm{HE}_1^{(\text{e})}\right)_\phi \left(\mathrm{HE}_1^{(\text{e})}\right)_\phi \left(\mathrm{O}^{\pm}_{+m_s}\right)^*_\phi \left(\mathrm{O}^{\pm}_{-m_i}\right)^*_\phi < 0 \tag{3.71b}$$

for the "$rrrr$"- and "$\phi\phi\phi\phi$"-components of the radial integrals in $I_{\mu\nu\tau\rho}$. Analogously, $I_{r\phi\phi r} > 0$ and $I_{\phi rr\phi} < 0$ or $I_{r\phi r\phi} > 0$ and $I_{\phi r\phi r} < 0$ have different signs for instance. Consequently, the weighted total sum over all transverse integrals is reduced since the tensor components of $\chi^{(3)}$ are non-negative and all integrals $|I_{\mu\nu\tau\rho}|$ for the same modes are in the same order of magnitude for the transverse field components we are considering, reminding Eq. (3.58). The generation process of two entangled OAM modes with the same polarisation handednesses is expected to be much weaker than the creation of OAM modes with opposite spins.

Furthermore, N_{pairs} is slightly decreasing with grating order m_g since the radial overlap integrals are smaller for a larger azimuthal order difference between the input and output modes. We have for example

$$\pi \sum_{\mu\tau\rho} \chi^{(3)}_{\mu\mu\tau\rho} \int_0^\infty \mathrm{d}r\, r \left(e_1^{\text{HE}}\right)_\mu \left(e_1^{\text{HE}}\right)_\mu \left(e_4^{\text{HE}}\right)^*_\tau \left(e_4^{\text{HE}}\right)^*_\rho$$
$$> \pi \sum_{\mu\tau\rho} \chi^{(3)}_{\mu\mu\tau\rho} \int_0^\infty \mathrm{d}r\, r \left(e_1^{\text{HE}}\right)_\mu \left(e_1^{\text{HE}}\right)_\mu \left(e_7^{\text{HE}}\right)^*_\tau \left(e_7^{\text{HE}}\right)^*_\rho \tag{3.72}$$

for the modes listed first in Tab. 3.3: $\mathbf{O}^+_{+3}$ and $\mathbf{O}^-_{-3}$ in comparison to the higher-order modes $\mathbf{O}^+_{+6}$ and $\mathbf{O}^-_{-6}$.[13]

Moreover, the generation of entangled $\mathbf{O}^-_{+m_g}$ and $\mathbf{O}^+_{-m_g}$ modes is more likely than the creation of $\mathbf{O}^+_{+m_g}$ and $\mathbf{O}^-_{-m_g}$ modes because of their bigger modal overlap:

$$\pi \sum_{\mu\tau\rho} \chi^{(3)}_{\mu\mu\tau\rho} \int_0^\infty \mathrm{d}r\, r \left(e_1^{\text{HE}}\right)_\mu \left(e_1^{\text{HE}}\right)_\mu \left(e_{m_g-1}^{\text{EH}}\right)^*_\tau \left(e_{m_g-1}^{\text{EH}}\right)^*_\rho$$
$$> \pi \sum_{\mu\tau\rho} \chi^{(3)}_{\mu\mu\tau\rho} \int_0^\infty \mathrm{d}r\, r \left(e_1^{\text{HE}}\right)_\mu \left(e_1^{\text{HE}}\right)_\mu \left(e_{m_g+1}^{\text{HE}}\right)^*_\tau \left(e_{m_g+1}^{\text{HE}}\right)^*_\rho . \tag{3.73}$$

Similarly, N_{pairs} of the $\mathbf{O}^-_{+m_g}$ and $\mathbf{O}^-_{-m_g}$ modes is larger than the number of photon pairs respecting the generation of $\mathbf{O}^+_{+m_g}$ and $\mathbf{O}^+_{-m_g}$ modes since

$$\frac{\pi}{2} \sum_{\mu\nu\tau\rho} \chi^{(3)}_{\mu\nu\tau\rho} \int_0^\infty \mathrm{d}r\, r \left(e_1^{\text{HE}}\right)_\mu \left(e_1^{\text{HE}}\right)_\nu \left(e_{m_g-1}^{\text{EH}}(\bar{\omega}_s)\right)^*_\tau \left(e_{m_g+1}^{\text{HE}}(\bar{\omega}_i)\right)^*_\rho$$
$$> \frac{\pi}{2} \sum_{\mu\nu\tau\rho} \chi^{(3)}_{\mu\nu\tau\rho} \int_0^\infty \mathrm{d}r\, r \left(e_1^{\text{HE}}\right)_\mu \left(e_1^{\text{HE}}\right)_\nu \left(e_{m_g+1}^{\text{HE}}(\bar{\omega}_s)\right)^*_\tau \left(e_{m_g-1}^{\text{EH}}(\bar{\omega}_i)\right)^*_\rho , \tag{3.74}$$

where the radial parts $e^{\text{HE}}_{m_g+1}$ (of the $\mathbf{O}^+_{+m_g}$ and $\mathbf{O}^-_{-m_g}$ modes) and $e^{\text{EH}}_{m_g-1}$ (of $\mathbf{O}^-_{+m_g}$ and $\mathbf{O}^+_{-m_g}$) are evaluated at the central signal or idler frequencies, respectively.

Recapitulating, in the case of different spins of the signal and idler photons the mean photon number per pump pulse is in the order magnitude 10^{-9} to 10^{-10} with regard to the chosen waveguide parameters and pump wavelengths. The generation probability of OAM modes with the same spins is negligible because the associated spin-orbit-coupling process has a low probability. To further enhance the efficiency of the process for a fixed value of N_{pairs}, short-pulsed lasers can be used to increase the number of generated photon pairs per second; then $\frac{N_{\text{pairs}}}{\tau_{\text{pulse}}}$ is greater for the same pump power per pulse as the pulse duration τ_{pulse} is minimised.

Overall, it is shown that inserting non-degenerate pump modes into a helically structured waveguide from different sides leads to the production of counterpropagating photon pairs that are entangled in their OAM degree of freedom. The characteristics of the modes (topological charges, polarisation frequency and transverse profiles) are determined by the waveguide structure (grating order, periodic length and modulation strength).

[13] The azimuthal integral is excluded with $\mu = \nu$ using Eq. (3.68) for modes with opposite spins.

4 Conclusion

Using helical grating structures in cylindrical step-index waveguides, the mode-coupling process from fundamental to higher-order modes has been investigated. The coupled mode equations have been derived and the corresponding transmission and reflection spectra have been presented for uniform and apodised gratings. The coupling constants between the input and output modes have been examined analytically and numerically. Supposing a narrow-core waveguide with a shallow grating the strongly coupled modes exhibit coupling constants in the range of $[6.9, 20]\,\frac{1}{\mathrm{mm}}$, leading to minimum waveguide lengths of less than 1 mm for maximum transmission. The weakly coupled modes associated with spin-orbit coupling are not expected to be stable. A Gedankenexperiment based on an external photon source has shown that the spiral gratings can be used to convert polarisation entanglement into higher-dimensional entanglement in OAM connected with the path degree of freedom.

A miniaturisation of the setup has been provided by the description of a non-linear FWM process in the periodic waveguides. The generated state has been derived in the quantum-mechanical approach and the difference between the central frequencies of the pumps and the signal (idler) photons has been calculated. By choosing non-degenerate pumps with a large wavelength difference of 1.05 µm, the generated OAM modes exhibit a frequency detuning of $\Delta\omega = 0.43\,\mathrm{THz}$ for the chosen waveguide parameters and a grating order of $m_g = 3$. For higher-order modes with topological charge $m_g = 6$, the frequency difference from the pumps is increased with $\Delta\omega = 1.1\,\mathrm{THz}$. Spectral filtering would be possible with bandpass filters. The derivation of the two-photon amplitude has revealed that - next to the typical sinc function with a maximum at $\Delta\beta = 0$ representing perfect phase matching - the JSA consists of two additional sinc functions due to the grating. The latter lead to sidelobes of the total JSA at approximately $\Delta\beta = \pm 2\kappa$. Moreover, the central peak of the JSA oscillates with $\kappa \propto \Delta\varepsilon_0$ but is almost stable in short waveguides with $L \ll \frac{\pi}{\kappa}$. A suppression of the central peak is possible using appropriate dispersion engineering. The calculation of the mean photon number per pump pulse has come to the conclusion that N_{pairs} is in the order of magnitude 10^{-9} to 10^{-10} with respect to the generation of OAM modes with different spins and the supposed waveguide and pump characteristics. The generation probability of OAM modes with the same spins is negligible.

In summary, high-dimensional entanglement can be stored by counterpropagating OAM modes described by a FWM process in helically structured core-cladding waveguides. Integrated platforms on-chip offer a possible implementation. In further investigations one could introduce losses in the waveguide structure and optimise the waveguide characteristics such as core radius, refractive indices and periodic lengths. Apodised gratings and a spectral distribution of the pump photons and the mode profiles could be taken into account.

Appendix A

Group velocity of hybrid modes - Derivation

In this section the group velocity $\mathbf{v}_G$ of a hybrid mode is derived.[1] It can be defined as the average Poynting vector $\langle \mathbf{S} \rangle$ (associated with the energy flux) per average energy density $\langle u_{\mathrm{em}} \rangle$: [27]

$$\mathbf{v}_G = \frac{\langle \mathbf{S} \rangle}{\langle u_{\mathrm{em}} \rangle}. \tag{A.1}$$

$\langle \mathbf{S} \rangle$ and $\langle u_{\mathrm{em}} \rangle$ are derived one after another.

We start with the general electric field ansatz[2]

$$\mathbf{E}^{(+)}(x,y,z,t) = a(z,t)\,\mathbf{f}(x,y)\,e^{i(\beta z - \omega t)} \tag{A.2}$$

which determines the magnetic field using Maxwell's equations:

$$\begin{aligned}
\frac{\partial}{\partial t}\mathbf{H}^{(+)}(x,y,z,t) &= -\frac{1}{\mu_0}\boldsymbol{\nabla} \times \mathbf{E}^{(+)}(x,y,z,t) \\
&= -\frac{1}{\mu_0}\begin{pmatrix}\partial_x\\ \partial_y\\ \partial_z\end{pmatrix} \times \left(a(z,t)\begin{pmatrix} f_x(x,y)\\ f_y(x,y)\\ f_z(x,y)\end{pmatrix} e^{i(\beta z-\omega t)}\right) \\
&= -\frac{1}{\mu_0}\left(\begin{pmatrix} \frac{\partial f_z}{\partial y} - f_y(i\beta + \frac{\partial}{\partial z})\\ f_x(i\beta + \frac{\partial}{\partial z}) - \frac{\partial f_z}{\partial x}\\ \frac{\partial f_y}{\partial x} - \frac{\partial f_x}{\partial y}\end{pmatrix} a(z,t)\right) e^{i(\beta z-\omega t)},
\end{aligned} \tag{A.3}$$

where $\partial_\xi = \frac{\partial}{\partial \xi}$ with $\xi \in \{\, x, y, z \,\}$ denotes a partial derivation and μ_0 is the magnetic permeability in vacuum. $\boldsymbol{\nabla}\times$ represents the curl operator; $\times$ solely labels a cross product - exceptional in this section. Partial integration over t leads to:

$$\begin{aligned}
\mathbf{H}^{(+)}(x,y,z,t) &= \frac{1}{i\omega\mu_0}\left(\begin{pmatrix} \frac{\partial f_z}{\partial y} - f_y(i\beta + \frac{\partial}{\partial z})\\ f_x(i\beta + \frac{\partial}{\partial z}) - \frac{\partial f_z}{\partial x}\\ \frac{\partial f_y}{\partial x} - \frac{\partial f_x}{\partial y}\end{pmatrix}\left(a(z,t) + \frac{1}{i\omega}\frac{\partial a(z,t)}{\partial t}\right)\right) e^{i(\beta z-\omega t)} \\
&= \frac{1}{i\omega\mu_0}\left(\begin{pmatrix} \frac{\partial f_z}{\partial y} - f_y(i\beta + \frac{\partial}{\partial z})\\ f_x(i\beta + \frac{\partial}{\partial z}) - \frac{\partial f_z}{\partial x}\\ \frac{\partial f_y}{\partial x} - \frac{\partial f_x}{\partial y}\end{pmatrix} a(z,t)\right) e^{i(\beta z-\omega t)}.
\end{aligned} \tag{A.4}$$

The slowly-varying approximation $\frac{\partial a(z,t)}{\partial t} \ll \omega\, a(z,t)$ is applied in the second step.[3]

[1] The subscript that labelled the mode in the main text is omitted for simplicity.

[2] This notation is in correspondence with the electric field ansatz in Eq. (3.9) with the mode profiles $\mathbf{f}(r,\phi) \to \mathbf{f}(x,y)$ in Cartesian coordinates x, y in the transverse plane.

[3] The integration constant is set to 0 for simplicity.

With these expressions of the electric field (Eq. (A.2)) and the magnetic field (Eq. (A.4)), the average Poynting vector of mode j is given by

$$\begin{aligned}
\langle \mathbf{S} \rangle &= \frac{1}{2} \iiint \mathrm{d}x\,\mathrm{d}y\,\mathrm{d}z\,\mathrm{Re}\Big[\left(\mathbf{E}^{(+)}\right)^* \times \mathbf{H}^{(+)} \Big] \\
&= \frac{1}{2} \iiint \mathrm{d}x\,\mathrm{d}y\,\mathrm{d}z\,\mathrm{Re}\left[a^*(z,t)\ \mathbf{f}^*(x,y) \times \left(\frac{1}{i\omega\mu_0} \begin{pmatrix} \frac{\partial f_z}{\partial y} - f_y(i\beta + \frac{\partial}{\partial z}) \\ f_x(i\beta + \frac{\partial}{\partial z}) - \frac{\partial f_z}{\partial x} \\ \frac{\partial f_y}{\partial x} - \frac{\partial f_x}{\partial y} \end{pmatrix} a(z,t) \right) \right] \\
&= \frac{\beta}{2\omega\mu_0} \left(\int \mathrm{d}z\ |a(z,t)|^2 \right) \left(\iint \mathrm{d}x\,\mathrm{d}y \begin{pmatrix} f_x^*(x,y) \\ f_y^*(x,y) \\ f_z^*(x,y) \end{pmatrix} \times \begin{pmatrix} -f_y(x,y) \\ f_x(x,y) \\ 0 \end{pmatrix} \right) \\
&= \frac{\varepsilon_0}{2}\, c\, n_{\mathrm{eff}} \left(\int \mathrm{d}z\ |a(z,t)|^2 \right) \left(\iint \mathrm{d}x\,\mathrm{d}y \begin{pmatrix} -f_z^*(x,y)\ f_x(x,y) \\ -f_z^*(x,y)\ f_y(x,y) \\ |f_x(x,y)|^2 + |f_y(x,y)|^2 \end{pmatrix} \right) \\
&= \frac{\varepsilon_0}{2}\, c\, n_{\mathrm{eff}}\, \langle a(z,t) | a(z,t) \rangle \begin{pmatrix} -\langle f_z(x,y) | f_x(x,y) \rangle \\ -\langle f_z(x,y) | f_y(x,y) \rangle \\ \langle f_x(x,y) | f_x(x,y) \rangle + \langle f_y(x,y) | f_y(x,y) \rangle \end{pmatrix}, \qquad \text{(A.5)}
\end{aligned}$$

where $\times$ denotes a cross product, ε_0 is the dielectric constant in vacuum, $c = \frac{1}{\sqrt{\varepsilon_0 \mu_0}}$ is the vacuum speed of light and $n_{\mathrm{eff}} = \frac{c\beta}{\omega}$ is the effective refractive index of the mode. Here, the brackets $\langle . | . \rangle$ denote an integration over z for $a(z,t)$ or over the transverse plane x, y for $\mathbf{f}(x,y)$, respectively. Note that the spatial derivations $\frac{\partial a(z,t)}{\partial z}$ and $\frac{\partial \mathbf{f}(x,y)}{\partial y}$ in the third step vanish because of the real-part function.[4]

Under the assumption that the overlap integrals with a longitudinal mode-profile component f_z are much smaller than those without,

$$\langle f_{x,y,z}(x,y) | f_z(x,y) \rangle \ll \langle f_{x,y}(x,y) | f_{x,y}(x,y) \rangle\,, \qquad \text{(A.6)}$$

only the longitudinal component of the average Poynting vector is left:

$$\langle \mathbf{S} \rangle \approx \frac{\varepsilon_0}{2}\, c\, n_{\mathrm{eff}}\, \langle a(z,t) | a(z,t) \rangle\, \langle \mathbf{f}(x,y) | \mathbf{f}(x,y) \rangle\ \mathbf{e_z}, \qquad \text{(A.7)}$$

where $\mathbf{e_z}$ represents the unity vector in z-direction.

The calculation of the integrated electromagnetic energy density is shown next. It is divided into its additive electric and magnetic energy-density parts. The average electric energy density is given by

$$\begin{aligned}
\langle u_{\mathrm{e}} \rangle &= \frac{1}{4} \iiint \mathrm{d}x\,\mathrm{d}y\,\mathrm{d}z\,\mathrm{Re}\Big[\varepsilon_0\, \bar{\varepsilon}(x,y) \left| \mathbf{E}^{(+)} \right|^2 \Big] \qquad \text{(A.8)} \\
&= \frac{\varepsilon_0}{4} \langle a(z,t) | a(z,t) \rangle\, \langle \mathbf{f}(x,y) | \bar{\varepsilon}(x,y) | \mathbf{f}(x,y) \rangle\,, \qquad \text{(A.9)}
\end{aligned}$$

where a dispersionless medium with $\frac{\mathrm{d}\varepsilon}{\mathrm{d}\omega} = 0$ and a small perturbation $\Delta\varepsilon(x,y,z)$ to the mean dielectric constant $\bar{\varepsilon}(x,y)$, i.e. $\Delta\varepsilon(x,y,z) \ll \bar{\varepsilon}(x,y)$, are assumed.

[4] The definition of the real-part function is $\mathrm{Re}[\alpha_1 + i\alpha_2] = \alpha_1$, where $\alpha_{1,2} \in \mathbb{R}$.

Secondly, the average magnetic energy density is derived:

$$\begin{aligned}
\langle u_{\mathrm{m}} \rangle &= \frac{1}{4} \iiint \mathrm{d}x\, \mathrm{d}y\, \mathrm{d}z\, \mathrm{Re}\left[\mu_0 \left| \mathbf{H}^{(+)} \right|^2 \right] \\
&= \frac{\varepsilon_0}{4} \langle a(z,t) | a(z,t) \rangle \left(\langle f_x(x,y) | \bar{\varepsilon}(x,y) | f_x(x,y) \rangle + \langle f_y(x,y) | \bar{\varepsilon}(x,y) | f_y(x,y) \rangle \right) \\
&= \frac{\varepsilon_0}{4} \langle a(z,t) | a(z,t) \rangle \left(\langle \mathbf{f}(x,y) | \bar{\varepsilon}(x,y) | \mathbf{f}(x,y) \rangle - \langle f_z(x,y) | \bar{\varepsilon}(x,y) | f_z(x,y) \rangle \right) \\
&\approx \frac{\varepsilon_0}{4} \langle a(z,t) | a(z,t) \rangle \langle \mathbf{f}(x,y) | \bar{\varepsilon}(x,y) | \mathbf{f}(x,y) \rangle \,, \qquad \text{(A.10)}
\end{aligned}$$

where

$$\langle f_z(x,y) | \bar{\varepsilon}(x,y) | f_z(x,y) \rangle \ll \langle f_{x,y}(x,y) | \bar{\varepsilon}(x,y) | f_{x,y}(x,y) \rangle \qquad \text{(A.11)}$$

is assumed in the last step. The average electromagnetic energy density is consequently

$$\langle u_{\mathrm{em}} \rangle = \langle u_{\mathrm{e}} \rangle + \langle u_{\mathrm{m}} \rangle \approx \frac{\varepsilon_0}{2} \langle a(z,t) | a(z,t) \rangle \langle \mathbf{f}(x,y) | \bar{\varepsilon}(x,y) | \mathbf{f}(x,y) \rangle \,. \qquad \text{(A.12)}$$

In such a way, the group velocity (A.1) becomes by using Eqs. (A.7) and (A.12),

$$\mathbf{v}_G = \frac{\langle \mathbf{S} \rangle}{\langle u_{\mathrm{em}} \rangle} \approx c\, n_{\mathrm{eff}} \frac{\langle \mathbf{f}(x,y) | \mathbf{f}(x,y) \rangle}{\langle \mathbf{f}(x,y) | \bar{\varepsilon}(x,y) | \mathbf{f}(x,y) \rangle} \mathbf{e_z}, \qquad \text{(A.13)}$$

under the assumptions of (A.6) and (A.11).

Appendix B

Helical grating structure

The helical structure

$$\Delta\varepsilon(r,\phi,z) = \cos\left(\frac{2\pi}{\Lambda}z - m_g\phi\right) \tag{B.1}$$

with $m_g \in \mathbb{Z}$ is both, periodic in azimuthal phase $\phi \in [0, 2\pi]$ and longitudinal direction $z \in [0, \Lambda]$ according to

$$\Delta\varepsilon(r,\phi,z) = \Delta\varepsilon(r,\phi+2\pi,z) = \Delta\varepsilon(r,\phi,z+\Lambda), \tag{B.2}$$

since

$$\Delta\varepsilon(r,\phi+2\pi,z) = \cos\left(\frac{2\pi}{\Lambda}z - m_g(\phi+2\pi)\right) = \cos\left(\frac{2\pi}{\Lambda}z - m_g\phi\right) \tag{B.3}$$

and

$$\Delta\varepsilon(r,\phi,z+\Lambda) = \cos\left(\frac{2\pi}{\Lambda}(z+\Lambda) - m_g\phi\right) = \cos\left(\frac{2\pi}{\Lambda}z - m_g\phi\right). \tag{B.4}$$

$|m_g|$ is the number of index modulations in the cross-section of the waveguide core. The sign of m_g, $sign(m_g)$, determines the helical handedness of the grating.

For comparison, commonly used helical gratings as in [56] or [57] are described by

$$\Delta\tilde{\varepsilon}(r,\phi,z) = \cos\left(|m_g|\left(\frac{2\pi}{\tilde{\Lambda}}z - sign(m_g)\phi\right)\right). \tag{B.5}$$

Their termed "grating period" $\tilde{\Lambda}$ is the period of one of the intertwined helicoids. Our Λ is the minimal grating period with respect to all $|m_g|$ spirals; the whole index modulation is considered. The periods are related via

$$\tilde{\Lambda} = m_g\Lambda. \tag{B.6}$$

However, the physics stays the same. Only the notations differentiate.

Appendix C

Coupling constants - Derivation

The analytical calculation of the coupling constants (3.16) in Sec. 3.1.2 is supplemented.

C.1 Coupled mode integrals

First, the overlap integrals of the coupled modes are investigated. Eq. (C.1) shows a list of the transverse integrals for a fixed input mode $\mathbf{HE}_m^{(\mathrm{e})}$ to all possible output modes after the separation of the radial and azimuthal integrals.

- Hybrid modes

$$\begin{aligned}
\langle \mathbf{HE}_m^{(\mathrm{e})} | e^{-im_g\phi}\,\Theta(a-r) | \mathbf{HE}_{\tilde{m}}^{(\mathrm{e})} \rangle &= \left[\int_0^a dr\, r\, \mathbf{e}_m^{\mathrm{HE}^*}(r) \circ \mathbf{e}_{\tilde{m}}^{\mathrm{HE}}(r)\right]^T \cdot \left[\int_0^{2\pi} d\phi\, \mathbf{g}_m^{(\mathrm{e})}(\phi) \circ \mathbf{g}_{\tilde{m}}^{(\mathrm{e})}(\phi)\, e^{-im_g\phi}\right] \\
\langle \mathbf{HE}_m^{(\mathrm{e})} | e^{-im_g\phi}\,\Theta(a-r) | \mathbf{HE}_{\tilde{m}}^{(\mathrm{o})} \rangle &= \left[\int_0^a dr\, r\, \mathbf{e}_m^{\mathrm{HE}^*}(r) \circ \mathbf{e}_{\tilde{m}}^{\mathrm{HE}}(r)\right]^T \cdot \left[\int_0^{2\pi} d\phi\, \mathbf{g}_m^{(\mathrm{e})}(\phi) \circ \mathbf{g}_{\tilde{m}}^{(\mathrm{o})}(\phi)\, e^{-im_g\phi}\right] \\
\langle \mathbf{HE}_m^{(\mathrm{e})} | e^{-im_g\phi}\,\Theta(a-r) | \mathbf{EH}_{\tilde{m}}^{(\mathrm{e})} \rangle &= \left[\int_0^a dr\, r\, \mathbf{e}_m^{\mathrm{HE}^*}(r) \circ \mathbf{e}_{\tilde{m}}^{\mathrm{EH}}(r)\right]^T \cdot \left[\int_0^{2\pi} d\phi\, \mathbf{g}_m^{(\mathrm{e})}(\phi) \circ \mathbf{g}_{\tilde{m}}^{(\mathrm{e})}(\phi)\, e^{-im_g\phi}\right] \\
\langle \mathbf{HE}_m^{(\mathrm{e})} | e^{-im_g\phi}\,\Theta(a-r) | \mathbf{EH}_{\tilde{m}}^{(\mathrm{o})} \rangle &= \left[\int_0^a dr\, r\, \mathbf{e}_m^{\mathrm{HE}^*}(r) \circ \mathbf{e}_{\tilde{m}}^{\mathrm{EH}}(r)\right]^T \cdot \left[\int_0^{2\pi} d\phi\, \mathbf{g}_m^{(\mathrm{e})}(\phi) \circ \mathbf{g}_{\tilde{m}}^{(\mathrm{o})}(\phi)\, e^{-im_g\phi}\right]
\end{aligned}$$

- OAM modes

$$\begin{aligned}
\langle \mathbf{HE}_m^{(\mathrm{e})} | e^{-im_g\phi}\,\Theta(a-r) | \mathbf{O}_{+\tilde{\mathbf{m}}}^{+} \rangle &= \left[\int_0^a dr\, r\, \mathbf{e}_m^{\mathrm{HE}^*}(r) \circ \mathbf{e}_{\tilde{m}+1}^{\mathrm{HE}}(r)\right]^T \cdot \left[\int_0^{2\pi} d\phi\, \mathbf{g}_m^{(\mathrm{e})}(\phi) \circ \mathbf{g}_{\tilde{m}+1}^{(+)}(\phi)\, e^{-im_g\phi}\right] \\
\langle \mathbf{HE}_m^{(\mathrm{e})} | e^{-im_g\phi}\,\Theta(a-r) | \mathbf{O}_{+\tilde{\mathbf{m}}}^{-} \rangle &= \left[\int_0^a dr\, r\, \mathbf{e}_m^{\mathrm{HE}^*}(r) \circ \mathbf{e}_{\tilde{m}-1}^{\mathrm{EH}}(r)\right]^T \cdot \left[\int_0^{2\pi} d\phi\, \mathbf{g}_m^{(\mathrm{e})}(\phi) \circ \mathbf{g}_{\tilde{m}-1}^{(+)}(\phi)\, e^{-im_g\phi}\right] \\
\langle \mathbf{HE}_m^{(\mathrm{e})} | e^{-im_g\phi}\,\Theta(a-r) | \mathbf{O}_{-\tilde{\mathbf{m}}}^{+} \rangle &= \left[\int_0^a dr\, r\, \mathbf{e}_m^{\mathrm{HE}^*}(r) \circ \mathbf{e}_{\tilde{m}-1}^{\mathrm{EH}}(r)\right]^T \cdot \left[\int_0^{2\pi} d\phi\, \mathbf{g}_m^{(\mathrm{e})}(\phi) \circ \mathbf{g}_{\tilde{m}-1}^{(-)}(\phi)\, e^{-im_g\phi}\right] \\
\langle \mathbf{HE}_m^{(\mathrm{e})} | e^{-im_g\phi}\,\Theta(a-r) | \mathbf{O}_{-\tilde{\mathbf{m}}}^{-} \rangle &= \left[\int_0^a dr\, r\, \mathbf{e}_m^{\mathrm{HE}^*}(r) \circ \mathbf{e}_{\tilde{m}+1}^{\mathrm{HE}}(r)\right]^T \cdot \left[\int_0^{2\pi} d\phi\, \mathbf{g}_m^{(\mathrm{e})}(\phi) \circ \mathbf{g}_{\tilde{m}+1}^{(-)}(\phi)\, e^{-im_g\phi}\right]
\end{aligned}$$

- Circularly polarised modes

$$\begin{aligned}
\langle \mathbf{HE}_m^{(\mathrm{e})} | e^{-im_g\phi}\,\Theta(a-r) | \mathbf{\Sigma}^{+} \rangle &= \left[\int_0^a dr\, r\, \mathbf{e}_m^{\mathrm{HE}^*}(r) \circ \mathbf{e}_1^{\mathrm{HE}}(r)\right]^T \cdot \left[\int_0^{2\pi} d\phi\, \mathbf{g}_m^{(\mathrm{e})}(\phi) \circ \mathbf{g}_1^{(+)}(\phi)\, e^{-im_g\phi}\right] \\
\langle \mathbf{HE}_m^{(\mathrm{e})} | e^{-im_g\phi}\,\Theta(a-r) | \mathbf{\Sigma}^{+} \rangle &= \left[\int_0^a dr\, r\, \mathbf{e}_m^{\mathrm{HE}^*}(r) \circ \mathbf{e}_1^{\mathrm{HE}}(r)\right]^T \cdot \left[\int_0^{2\pi} d\phi\, \mathbf{g}_m^{(\mathrm{e})}(\phi) \circ \mathbf{g}_1^{(-)}(\phi)\, e^{-im_g\phi}\right]
\end{aligned} \tag{C.1}$$

$m \geq 1$ for $\{\, \mathbf{HE}_m^{(\mathrm{e/o})}, \mathbf{EH}_m^{(\mathrm{e/o})}, \mathbf{O}_{+m}^{-}, \mathbf{O}_{-m}^{+} \,\}$ and $m \geq 2$ for $\{\, \mathbf{O}_{+m}^{+}, \mathbf{O}_{-m}^{-} \,\}$ are supposed as defined in Sec. 2.2. The list could be extended to other input modes.

The integrals over the azimuthal angle ϕ are solved next. Assuming the coupling between an even and an odd polarised hybrid mode in a helical grating with $m_g \neq 0$, that is:

$$
\begin{aligned}
&\int_0^{2\pi} d\phi\, \mathbf{g}_m^{(\mathrm{e})^*} \circ \mathbf{g}_{\tilde{m}}^{(\mathrm{o})}\, e^{-im_g\phi} \\
&= \int_0^{2\pi} d\phi \begin{pmatrix} \cos(m\phi) \\ \sin(m\phi) \\ \cos(m\phi) \end{pmatrix} \circ \begin{pmatrix} \sin(\tilde{m}\phi) \\ -\cos(\tilde{m}\phi) \\ \sin(\tilde{m}\phi) \end{pmatrix} e^{-im_g\phi} \\
&= \frac{1}{4}\int_0^{2\pi} d\phi \begin{pmatrix} e^{im\phi} + e^{-im\phi} \\ -i(e^{im\phi} - e^{-im\phi}) \\ e^{im\phi} + e^{-im\phi} \end{pmatrix} \circ \begin{pmatrix} -i(e^{i\tilde{m}\phi} - e^{-i\tilde{m}\phi}) \\ -(e^{i\tilde{m}\phi} + e^{-i\tilde{m}\phi}) \\ -i(e^{i\tilde{m}\phi} - e^{-i\tilde{m}\phi}) \end{pmatrix} e^{-im_g\phi} \\
&= -\frac{i}{4}\int_0^{2\pi} d\phi \begin{pmatrix} e^{i(m+\tilde{m})\phi} - e^{i(m-\tilde{m})\phi} + e^{-i(m-\tilde{m})\phi} - e^{-i(m+\tilde{m})\phi} \\ -e^{i(m+\tilde{m})\phi} - e^{i(m-\tilde{m})\phi} + e^{-i(m-\tilde{m})\phi} + e^{-i(m+\tilde{m})\phi} \\ e^{i(m+\tilde{m})\phi} - e^{i(m-\tilde{m})\phi} + e^{-i(m-\tilde{m})\phi} - e^{-i(m+\tilde{m})\phi} \end{pmatrix} e^{-im_g\phi} \\
&= -\frac{i}{4}\, 2\pi \times \begin{cases} \begin{pmatrix} 1 \\ -1 \\ 1 \end{pmatrix} & \text{, if } m_g = m + \tilde{m} \;\leftrightarrow\; \tilde{m} = m_g - m \\ \begin{pmatrix} -1 \\ -1 \\ -1 \end{pmatrix} & \text{, if } m_g = m - \tilde{m} \;\leftrightarrow\; \tilde{m} = -m_g + m \\ \begin{pmatrix} 1 \\ 1 \\ 1 \end{pmatrix} & \text{, if } m_g = -(m - \tilde{m}) \;\leftrightarrow\; \tilde{m} = m_g + m \\ \begin{pmatrix} -1 \\ 1 \\ -1 \end{pmatrix} & \text{, if } m_g = -(m + \tilde{m}) \;\leftrightarrow\; \tilde{m} = -m_g - m \\ 0 & \text{, otherwise} \end{cases} \\
&= -\frac{i\pi}{2} \times \begin{cases} \pm \begin{pmatrix} 1 \\ 1 \\ 1 \end{pmatrix} & \text{, if } m_g = \tilde{m} = \pm m_g + m \\ \pm \begin{pmatrix} 1 \\ -1 \\ 1 \end{pmatrix} & \text{, if } m_g = \tilde{m} = \pm m_g - m \\ 0 & \text{, otherwise} \end{cases} \\
&= \mp\frac{i\pi}{2} \times \begin{cases} \begin{pmatrix} 1 \\ \pm 1 \\ 1 \end{pmatrix} & \text{, if } \tilde{m} = \pm\, m_g \pm m \\ 0 & \text{, otherwise} \end{cases} .
\end{aligned}
\tag{C.2}
$$

The derivation of the azimuthal integral for two coupled, odd polarised hybrid modes yields analogously:

$$
\begin{aligned}
&\int_0^{2\pi} d\phi\, \mathbf{g}_m^{(\mathrm{o})^*}(r,\phi) \circ \mathbf{g}_{\tilde{m}}^{(\mathrm{o})}(r,\phi)\, e^{-im_g\phi} \\
&= \int_0^{2\pi} d\phi \begin{pmatrix} \sin(m\phi) \\ -\cos(m\phi) \\ \sin(m\phi) \end{pmatrix} \circ \begin{pmatrix} \sin(\tilde{m}\phi) \\ -\cos(\tilde{m}\phi) \\ \sin(\tilde{m}\phi) \end{pmatrix} e^{-im_g\phi} \\
&= \frac{1}{4}\int_0^{2\pi} d\phi \begin{pmatrix} -i(e^{im\phi} - e^{-im\phi}) \\ -(e^{im\phi} + e^{-im\phi}) \\ -i(e^{im\phi} - e^{-im\phi}) \end{pmatrix} \circ \begin{pmatrix} -i(e^{i\tilde{m}\phi} - e^{-i\tilde{m}\phi}) \\ -(e^{i\tilde{m}\phi} + e^{-i\tilde{m}\phi}) \\ -i(e^{i\tilde{m}\phi} - e^{-i\tilde{m}\phi}) \end{pmatrix} e^{-im_g\phi} \\
&= \frac{1}{4}\int_0^{2\pi} d\phi \begin{pmatrix} -e^{i(m+\tilde{m})\phi} + e^{i(m-\tilde{m})\phi} + e^{-i(m-\tilde{m})\phi} - e^{-i(m+\tilde{m})\phi} \\ e^{i(m+\tilde{m})\phi} + e^{i(m-\tilde{m})\phi} + e^{-i(m-\tilde{m})\phi} + e^{-i(m+\tilde{m})\phi} \\ -e^{i(m+\tilde{m})\phi} + e^{i(m-\tilde{m})\phi} + e^{-i(m-\tilde{m})\phi} - e^{-i(m+\tilde{m})\phi} \end{pmatrix} e^{-im_g\phi} \\
&= \frac{\pi}{2} \times \begin{cases} \begin{pmatrix} -1 \\ 1 \\ -1 \end{pmatrix} & , \text{if } m_g = m + \tilde{m} \;\leftrightarrow\; \tilde{m} = m_g - m \\ \begin{pmatrix} 1 \\ 1 \\ 1 \end{pmatrix} & , \text{if } m_g = m - \tilde{m} \;\leftrightarrow\; \tilde{m} = -m_g + m \\ \begin{pmatrix} 1 \\ 1 \\ 1 \end{pmatrix} & , \text{if } m_g = -(m - \tilde{m}) \;\leftrightarrow\; \tilde{m} = m_g + m \\ \begin{pmatrix} -1 \\ 1 \\ -1 \end{pmatrix} & , \text{if } m_g = -(m + \tilde{m}) \;\leftrightarrow\; \tilde{m} = -m_g - m \\ 0 & , \text{otherwise} \end{cases} \\
&= \frac{\pi}{2} \times \begin{cases} \begin{pmatrix} 1 \\ 1 \\ 1 \end{pmatrix} & , \text{if } m_g = \tilde{m} = \pm m_g + m \\ -\begin{pmatrix} 1 \\ -1 \\ 1 \end{pmatrix} & , \text{if } m_g = \tilde{m} = \pm m_g - m \\ 0 & , \text{otherwise} \end{cases} \\
&= \pm\frac{\pi}{2} \times \begin{cases} \begin{pmatrix} 1 \\ \pm 1 \\ 1 \end{pmatrix} & , \text{if } \tilde{m} = \pm\, m_g \pm m \\ 0 & , \text{otherwise} \end{cases} .
\end{aligned}
\tag{C.3}
$$

The angular integrals for all other mode combinations are calculated in the same way. The results are summarised in the following Tab. C.1.

hybrid mode → hybrid mode	$\int_0^{2\pi} d\phi\, \mathbf{g}_m^{(\mathrm{e})} \circ \mathbf{g}_{\tilde{m}}^{(\mathrm{e})}\, e^{-im_g\phi} =$	$\frac{\pi}{2}\begin{pmatrix}1\\1\\1\end{pmatrix}$	$\frac{\pi}{2}\begin{pmatrix}1\\1\\1\end{pmatrix}$	$\frac{\pi}{2}\begin{pmatrix}1\\-1\\1\end{pmatrix}$	$\frac{\pi}{2}\begin{pmatrix}1\\-1\\1\end{pmatrix}$
	$\int_0^{2\pi} d\phi\, \mathbf{g}_m^{(\mathrm{e})} \circ \mathbf{g}_{\tilde{m}}^{(\mathrm{o})}\, e^{-im_g\phi} =$	$\frac{-i\pi}{2}\begin{pmatrix}1\\1\\1\end{pmatrix}$	$\frac{i\pi}{2}\begin{pmatrix}1\\1\\1\end{pmatrix}$	$\frac{-i\pi}{2}\begin{pmatrix}1\\-1\\1\end{pmatrix}$	$\frac{i\pi}{2}\begin{pmatrix}1\\-1\\1\end{pmatrix}$
	$\int_0^{2\pi} d\phi\, \mathbf{g}_m^{(\mathrm{o})} \circ \mathbf{g}_{\tilde{m}}^{(\mathrm{e})}\, e^{-im_g\phi} =$	$\frac{i\pi}{2}\begin{pmatrix}1\\1\\1\end{pmatrix}$	$\frac{-i\pi}{2}\begin{pmatrix}1\\1\\1\end{pmatrix}$	$\frac{-i\pi}{2}\begin{pmatrix}1\\-1\\1\end{pmatrix}$	$\frac{i\pi}{2}\begin{pmatrix}1\\-1\\1\end{pmatrix}$
	$\int_0^{2\pi} d\phi\, \mathbf{g}_m^{(\mathrm{o})} \circ \mathbf{g}_{\tilde{m}}^{(\mathrm{o})}\, e^{-im_g\phi} =$	$\frac{\pi}{2}\begin{pmatrix}1\\1\\1\end{pmatrix}$	$\frac{\pi}{2}\begin{pmatrix}1\\1\\1\end{pmatrix}$	$\frac{-\pi}{2}\begin{pmatrix}1\\-1\\1\end{pmatrix}$	$\frac{-\pi}{2}\begin{pmatrix}1\\-1\\1\end{pmatrix}$
hybrid mode → circularly polarised mode	$\int_0^{2\pi} d\phi\, \mathbf{g}_m^{(\mathrm{e})} \circ \mathbf{g}_{\tilde{m}}^{(+)}\, e^{-im_g\phi} =$	$\pi\begin{pmatrix}1\\1\\1\end{pmatrix}$	0	$\pi\begin{pmatrix}1\\-1\\1\end{pmatrix}$	0
	$\int_0^{2\pi} d\phi\, \mathbf{g}_m^{(\mathrm{o})} \circ \mathbf{g}_{\tilde{m}}^{(+)}\, e^{-im_g\phi} =$	$i\pi\begin{pmatrix}1\\1\\1\end{pmatrix}$	0	$-i\pi\begin{pmatrix}1\\-1\\1\end{pmatrix}$	0
	$\int_0^{2\pi} d\phi\, \mathbf{g}_m^{(\mathrm{e})} \circ \mathbf{g}_{\tilde{m}}^{(-)}\, e^{-im_g\phi} =$	0	$\pi\begin{pmatrix}1\\1\\1\end{pmatrix}$	0	$\pi\begin{pmatrix}1\\-1\\1\end{pmatrix}$
	$\int_0^{2\pi} d\phi\, \mathbf{g}_m^{(\mathrm{o})} \circ \mathbf{g}_{\tilde{m}}^{(-)}\, e^{-im_g\phi} =$	0	$-i\pi\begin{pmatrix}1\\1\\1\end{pmatrix}$	0	$i\pi\begin{pmatrix}1\\-1\\1\end{pmatrix}$
circularly polarised mode → hybrid mode	$\int_0^{2\pi} d\phi\, \mathbf{g}_m^{(+)^*} \circ \mathbf{g}_{\tilde{m}}^{(\mathrm{e})}\, e^{-im_g\phi} =$	$\pi\begin{pmatrix}1\\1\\1\end{pmatrix}$	0	0	$\pi\begin{pmatrix}1\\-1\\1\end{pmatrix}$
	$\int_0^{2\pi} d\phi\, \mathbf{g}_m^{(+)^*} \circ \mathbf{g}_{\tilde{m}}^{(\mathrm{o})}\, e^{-im_g\phi} =$	$-i\pi\begin{pmatrix}1\\1\\1\end{pmatrix}$	0	0	$i\pi\begin{pmatrix}1\\-1\\1\end{pmatrix}$
	$\int_0^{2\pi} d\phi\, \mathbf{g}_m^{(-)^*} \circ \mathbf{g}_{\tilde{m}}^{(\mathrm{e})}\, e^{-im_g\phi} =$	0	$\pi\begin{pmatrix}1\\1\\1\end{pmatrix}$	$\pi\begin{pmatrix}1\\-1\\1\end{pmatrix}$	0
	$\int_0^{2\pi} d\phi\, \mathbf{g}_m^{(-)^*} \circ \mathbf{g}_{\tilde{m}}^{(\mathrm{o})}\, e^{-im_g\phi} =$	0	$i\pi\begin{pmatrix}1\\1\\1\end{pmatrix}$	$-i\pi\begin{pmatrix}1\\-1\\1\end{pmatrix}$	0
circularly polarised mode → circularly polarised mode	$\int_0^{2\pi} d\phi\, \mathbf{g}_m^{(+)^*} \circ \mathbf{g}_{\tilde{m}}^{(+)}\, e^{-im_g\phi} =$	$2\pi\begin{pmatrix}1\\1\\1\end{pmatrix}$	0	0	0
	$\int_0^{2\pi} d\phi\, \mathbf{g}_m^{(+)^*} \circ \mathbf{g}_{\tilde{m}}^{(-)}\, e^{-im_g\phi} =$	0	0	0	$2\pi\begin{pmatrix}1\\-1\\1\end{pmatrix}$
	$\int_0^{2\pi} d\phi\, \mathbf{g}_m^{(-)^*} \circ \mathbf{g}_{\tilde{m}}^{(+)}\, e^{-im_g\phi} =$	0	0	$2\pi\begin{pmatrix}1\\-1\\1\end{pmatrix}$	0
	$\int_0^{2\pi} d\phi\, \mathbf{g}_m^{(-)^*} \circ \mathbf{g}_{\tilde{m}}^{(-)}\, e^{-im_g\phi} =$	0	$2\pi\begin{pmatrix}1\\1\\1\end{pmatrix}$	0	0
	for $\tilde{m} =$	$m_g + m$	$-m_g + m$	$m_g - m$	$-m_g - m$

Tab. C.1 Solutions of the azimuthal integrals (as in Eq. (C.1)) for a coupling between two different modes: hybrid modes with even (e) or odd (o) polarisation and circularly polarised modes (including OAM modes) composed of an additive (+) or a subtractive (−) linear combination of hybrid modes, see Eq. (2.18) for definition. The integrals are only non-zero if one of the azimuthal phase-matching conditions for $\tilde{m}$ is fulfilled, see last row.

Note that to each azimuthal vector $\left(\mathbf{g}_m^{(\mathrm{e})}, \mathbf{g}_m^{(\mathrm{o})}, \mathbf{g}_{\mathbf{m}}^{(+)} \text{ and } \mathbf{g}_m^{(-)}\right)$ corresponds more than one mode profile:

$$
\begin{aligned}
&\mathbf{g}_m^{(\mathrm{e})} \rightarrow \{\mathbf{HE}_m^{(\mathrm{e})}, \mathbf{EH}_m^{(\mathrm{e})}\} \\
&\mathbf{g}_m^{(\mathrm{o})} \rightarrow \{\mathbf{HE}_m^{(\mathrm{o})}, \mathbf{EH}_m^{(\mathrm{o})}\} \\
&\mathbf{g}_m^{(+)} \rightarrow \{\mathbf{O}_{+m-1}^{+} \text{ for } m \geq 2,\ \mathbf{O}_{+m+1}^{-} \text{ for } m \geq 1,\ \mathbf{\Sigma}^{+} \text{ for } m = 1\} \\
&\mathbf{g}_m^{(-)} \rightarrow \{\mathbf{O}_{-(m-1)}^{-} \text{ for } m \geq 2,\ \mathbf{O}_{-(m+1)}^{+} \text{ for } m \geq 1,\ \mathbf{\Sigma}^{-} \text{ for } m = 1\}.
\end{aligned}
$$

Based on the results of the azimuthal integrals in Tab. C.1 the list of the coupling integrals in Eq. (C.1) is simplified. The vanishing terms with non-fulfilled azimuthal phase-matching conditions are omitted for clarity.

- Hybrid modes

$$
\begin{aligned}
\langle \mathbf{HE}_m^{(\mathrm{e})} | e^{-im_g\phi}\,\Theta(a-r) | \mathbf{HE}_{\tilde{m}=\pm m_g \pm m}^{(\mathrm{e})} \rangle &= \frac{\pi}{2} \int_0^a dr\, r \left(e_{m_r}^{\mathrm{HE}^*} e_{\tilde{m}_r}^{\mathrm{HE}} \pm e_{m_\phi}^{\mathrm{HE}^*} e_{\tilde{m}_\phi}^{\mathrm{HE}} + e_{m_z}^{\mathrm{HE}^*} e_{\tilde{m}_z}^{\mathrm{HE}} \right) \\
\langle \mathbf{HE}_m^{(\mathrm{e})} | e^{-im_g\phi}\,\Theta(a-r) | \mathbf{HE}_{\tilde{m}=\pm m_g \pm m}^{(\mathrm{o})} \rangle &= \frac{\mp i\pi}{2} \int_0^a dr\, r \left(e_{m_r}^{\mathrm{HE}^*} e_{\tilde{m}_r}^{\mathrm{HE}} \pm e_{m_\phi}^{\mathrm{HE}^*} e_{\tilde{m}_\phi}^{\mathrm{HE}} + e_{m_z}^{\mathrm{HE}^*} e_{\tilde{m}_z}^{\mathrm{HE}} \right) \\
\langle \mathbf{HE}_m^{(\mathrm{e})} | e^{-im_g\phi}\,\Theta(a-r) | \mathbf{EH}_{\tilde{m}=\pm m_g \pm m}^{(\mathrm{e})} \rangle &= \frac{\pi}{2} \int_0^a dr\, r \left(e_{m_r}^{\mathrm{HE}^*} e_{\tilde{m}_r}^{\mathrm{EH}} \pm e_{m_\phi}^{\mathrm{HE}^*} e_{\tilde{m}_\phi}^{\mathrm{EH}} + e_{m_z}^{\mathrm{HE}^*} e_{\tilde{m}_z}^{\mathrm{EH}} \right) \\
\langle \mathbf{HE}_m^{(\mathrm{e})} | e^{-im_g\phi}\,\Theta(a-r) | \mathbf{EH}_{\tilde{m}=\pm m_g \pm m}^{(\mathrm{o})} \rangle &= \frac{\mp i\pi}{2} \int_0^a dr\, r \left(e_{m_r}^{\mathrm{HE}^*} e_{\tilde{m}_r}^{\mathrm{EH}} \pm e_{m_\phi}^{\mathrm{HE}^*} e_{\tilde{m}_\phi}^{\mathrm{EH}} + e_{m_z}^{\mathrm{HE}^*} e_{\tilde{m}_z}^{\mathrm{EH}} \right)
\end{aligned}
$$

- OAM modes

$$
\begin{aligned}
\langle \mathbf{HE}_m^{(\mathrm{e})} | e^{-im_g\phi}\,\Theta(a-r) | \mathbf{O}_{+\tilde{m}=m_g \pm m-1}^{+} \rangle &= \pi \int_0^a dr\, r \left(e_{m_r}^{\mathrm{HE}^*} e_{\tilde{m}+1_r}^{\mathrm{HE}} \pm e_{m_\phi}^{\mathrm{HE}^*} e_{\tilde{m}+1_\phi}^{\mathrm{HE}} + e_{m_z}^{\mathrm{HE}^*} e_{\tilde{m}+1_z}^{\mathrm{HE}} \right) \\
\langle \mathbf{HE}_m^{(\mathrm{e})} | e^{-im_g\phi}\,\Theta(a-r) | \mathbf{O}_{+\tilde{m}=m_g \pm m-1}^{-} \rangle &= \pi \int_0^a dr\, r \left(e_{m_r}^{\mathrm{HE}^*} e_{\tilde{m}-1_r}^{\mathrm{EH}} \pm e_{m_\phi}^{\mathrm{HE}^*} \mathbf{e}_{\tilde{\mathbf{m}}-\mathbf{1}\phi}^{\mathrm{EH}} + e_{m_z}^{\mathrm{HE}^*} e_{\tilde{m}-1_z}^{\mathrm{EH}} \right) \\
\langle \mathbf{HE}_m^{(\mathrm{e})} | e^{-im_g\phi}\,\Theta(a-r) | \mathbf{O}_{-\tilde{m}=-(-m_g \pm m+1)}^{+} \rangle &= \pi \int_0^a dr\, r \left(e_{m_r}^{\mathrm{HE}^*} e_{\tilde{m}-1_r}^{\mathrm{EH}} \pm e_{m_\phi}^{\mathrm{HE}^*} e_{\tilde{m}-1_\phi}^{\mathrm{EH}} + e_{m_z}^{\mathrm{HE}^*} e_{\tilde{m}-1_z}^{\mathrm{EH}} \right) \\
\langle \mathbf{HE}_m^{(\mathrm{e})} | e^{-im_g\phi}\,\Theta(a-r) | \mathbf{O}_{-\tilde{m}=-(-m_g \pm m+1)}^{-} \rangle &= \pi \int_0^a dr\, r \left(e_{m_r}^{\mathrm{HE}^*} e_{\tilde{m}+1_r}^{\mathrm{HE}} \pm e_{m_\phi}^{\mathrm{HE}^*} e_{\tilde{m}+1_\phi}^{\mathrm{HE}} + e_{m_z}^{\mathrm{HE}^*} \mathbf{e}_{\tilde{\mathbf{m}}+\mathbf{1_z}}^{\mathrm{HE}} \right)
\end{aligned}
$$

- Circularly polarised modes

$$
\begin{aligned}
\langle \mathbf{HE}_{m=m_g \pm 1}^{(\mathrm{e})} | e^{-im_g\phi}\,\Theta(a-r) | \mathbf{\Sigma}^{+} \rangle &= \pi \int_0^a dr\, r \left(e_{m_r}^{\mathrm{HE}^*} e_{1_r}^{\mathrm{HE}} \pm e_{m_\phi}^{\mathrm{HE}^*} e_{1_\phi}^{\mathrm{HE}} + e_{m_z}^{\mathrm{HE}^*} e_{1_z}^{\mathrm{HE}} \right) \\
\langle \mathbf{HE}_{m=-m_g \pm 1}^{(\mathrm{e})} | e^{-im_g\phi}\,\Theta(a-r) | \mathbf{\Sigma}^{-} \rangle &= \pi \int_0^a dr\, r \left(e_{m_r}^{\mathrm{HE}^*} e_{1_r}^{\mathrm{HE}} \pm e_{m_\phi}^{\mathrm{HE}^*} e_{1_\phi}^{\mathrm{HE}} + e_{m_z}^{\mathrm{HE}^*} e_{1_z}^{\mathrm{HE}} \right)
\end{aligned}
\tag{C.4}
$$

The integrands in Eq. (C.4) of two hybrid modes $\mathrm{M}, \tilde{\mathrm{M}} \in \{\,\mathrm{HE}, \mathrm{EH}\,\}$ are with Eq. (2.12):

$$e^{\mathrm{M}^*}_{m_r} e^{\tilde{\mathrm{M}}}_{\tilde{m}_r} \pm e^{\mathrm{M}^*}_{m_\phi} e^{\tilde{\mathrm{M}}}_{\tilde{m}_\phi} + e^{\mathrm{M}^*}_{m_z} e^{\tilde{\mathrm{M}}}_{\tilde{m}_z}$$
$$= \frac{\beta\tilde{\beta}}{u^2\tilde{u}^2}\left[(s\tilde{s} \pm 1)\left(\frac{m\tilde{m}}{r^2}\bar{J}_m\bar{J}_{\tilde{m}} \pm u\tilde{u}\bar{J}'_m\bar{J}'_{\tilde{m}}\right) - (s \pm \tilde{s})\frac{1}{r}\left(m\tilde{u}\bar{J}_m\bar{J}'_{\tilde{m}} \pm \tilde{m}u\bar{J}_{\tilde{m}}\bar{J}'_m\right)\right] + \bar{J}_m\bar{J}_{\tilde{m}}. \tag{C.5}$$

The values of s, $\tilde{s}$ are given by Eq. (2.17) in the weakly-guiding approximation. The approximation is reasonable for small variations of the dielectric constant, $n_{\mathrm{co}} - n_{\mathrm{cl}} = 0.01$. Exact solutions of s for different modes and index changes are represented in the figure below.

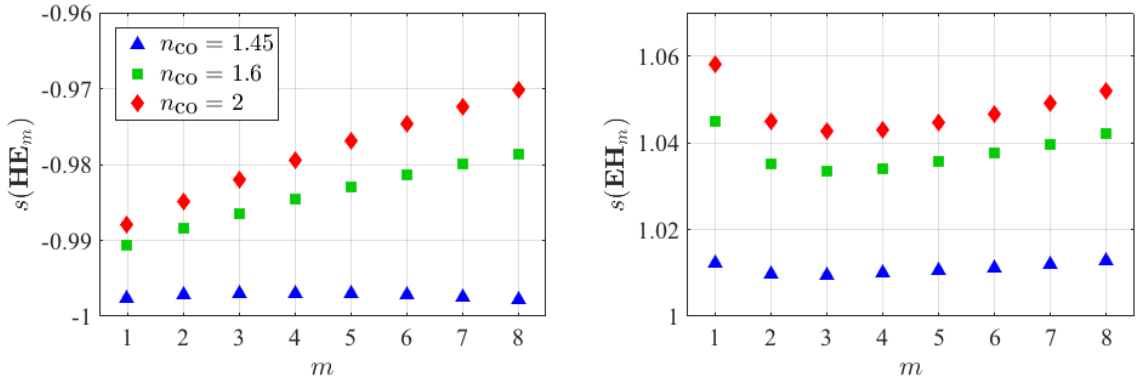

Fig. C.1 Numerical solutions of the parameter s from Eq. (2.14) for both HE and EH modes with varying azimuthal orders m for different mean refractive indices of the waveguide core n_{co}. The legend holds for both graphs. Fixed parameters are the refractive index of the cladding $n_{\mathrm{cl}} = 1.44$, the vacuum wavelength $\lambda = 1.55\,\mu\mathrm{m}$ and the core radius of the waveguide $a = 20\,\mu\mathrm{m}$.

Tab. C.2 shows the values of the excluded terms $(s\tilde{s} \pm 1)$ and $(s \pm \tilde{s})$ in Eq. (C.5) in the weakly-guiding approximation.

M	$\tilde{\mathrm{M}}$	$s\tilde{s}+1$	$s+\tilde{s}$	$s\tilde{s}-1$	$s-\tilde{s}$
HE	HE	2	−2	0	0
EH	EH	2	2	0	0
HE	EH	0	0	−2	−2
EH	HE	0	0	2	−2

Tab. C.2 List of the arising terms in Eq. (C.5) in the weakly-guiding approximation for all four combination possibilities of the hybrid-mode classes HE and EH

Substituting the values of $(s\tilde{s} \pm 1)$ and $(s \pm \tilde{s})$ shown in Tab. C.2, Eq. (C.5) becomes for all hybrid-mode combinations:

- HE $\rightarrow$ HE

$$
\begin{aligned}
&e^{\mathrm{HE}^*}_{m_r} e^{\mathrm{HE}}_{\tilde{m}_r} - e^{\mathrm{HE}^*}_{m_\phi} e^{\mathrm{HE}}_{\tilde{m}_\phi} + e^{\mathrm{HE}^*}_{m_z} e^{\mathrm{HE}}_{\tilde{m}_z} = \bar{J}_m \bar{J}_{\tilde{m}} \\
&e^{\mathrm{HE}^*}_{m_r} e^{\mathrm{HE}}_{\tilde{m}_r} + e^{\mathrm{HE}^*}_{m_\phi} e^{\mathrm{HE}}_{\tilde{m}_\phi} + e^{\mathrm{HE}^*}_{m_z} e^{\mathrm{HE}}_{\tilde{m}_z} \\
&\quad = \frac{2\beta\tilde{\beta}}{u^2\tilde{u}^2}\left[\frac{m\tilde{m}}{r^2}\bar{J}_m\bar{J}_{\tilde{m}} + u\tilde{u}\bar{J}'_m\bar{J}'_{\tilde{m}} + \frac{1}{r}\left(m\tilde{u}\bar{J}_m\bar{J}'_{\tilde{m}} + \tilde{m}u\bar{J}_{\tilde{m}}\bar{J}'_m\right)\right] + \bar{J}_m\bar{J}_{\tilde{m}}
\end{aligned}
$$

- HE $\rightarrow$ EH

$$
\begin{aligned}
&e^{\mathrm{HE}^*}_{m_r} e^{\mathrm{EH}}_{\tilde{m}_r} + e^{\mathrm{HE}^*}_{m_\phi} e^{\mathrm{EH}}_{\tilde{m}_\phi} + e^{\mathrm{HE}^*}_{m_z} e^{\mathrm{EH}}_{\tilde{m}_z} = \bar{J}_m \bar{J}_{\tilde{m}} \\
&e^{\mathrm{HE}^*}_{m_r} e^{\mathrm{EH}}_{\tilde{m}_r} - e^{\mathrm{HE}^*}_{m_\phi} e^{\mathrm{EH}}_{\tilde{m}_\phi} + e^{\mathrm{HE}^*}_{m_z} e^{\mathrm{EH}}_{\tilde{m}_z} \\
&\quad = \frac{-2\beta\tilde{\beta}}{u^2\tilde{u}^2}\left[\frac{m\tilde{m}}{r^2}\bar{J}_m\bar{J}_{\tilde{m}} + u\tilde{u}\bar{J}'_m\bar{J}'_{\tilde{m}} - \frac{1}{r}\left(m\tilde{u}\bar{J}_m\bar{J}'_{\tilde{m}} + \tilde{m}u\bar{J}_{\tilde{m}}\bar{J}'_m\right)\right] + \bar{J}_m\bar{J}_{\tilde{m}}
\end{aligned}
$$

- EH $\rightarrow$ HE

$$
\begin{aligned}
&e^{\mathrm{EH}^*}_{m_r} e^{\mathrm{HE}}_{\tilde{m}_r} + e^{\mathrm{EH}^*}_{m_\phi} e^{\mathrm{HE}}_{\tilde{m}_\phi} + e^{\mathrm{EH}^*}_{m_z} e^{\mathrm{HE}}_{\tilde{m}_z} = \bar{J}_m \bar{J}_{\tilde{m}} \\
&e^{\mathrm{EH}^*}_{m_r} e^{\mathrm{HE}}_{\tilde{m}_r} - e^{\mathrm{EH}^*}_{m_\phi} e^{\mathrm{HE}}_{\tilde{m}_\phi} + e^{\mathrm{EH}^*}_{m_z} e^{\mathrm{HE}}_{\tilde{m}_z} \\
&\quad = \frac{-2\beta\tilde{\beta}}{u^2\tilde{u}^2}\left[\frac{m\tilde{m}}{r^2}\bar{J}_m\bar{J}_{\tilde{m}} + u\tilde{u}\bar{J}'_m\bar{J}'_{\tilde{m}} + \frac{1}{r}\left(m\tilde{u}\bar{J}_m\bar{J}'_{\tilde{m}} + \tilde{m}u\bar{J}_{\tilde{m}}\bar{J}'_m\right)\right] + \bar{J}_m\bar{J}_{\tilde{m}}
\end{aligned}
$$

- EH $\rightarrow$ EH

$$
\begin{aligned}
&e^{\mathrm{EH}^*}_{m_r} e^{\mathrm{EH}}_{\tilde{m}_r} - e^{\mathrm{EH}^*}_{m_\phi} e^{\mathrm{EH}}_{\tilde{m}_\phi} + e^{\mathrm{EH}^*}_{m_z} e^{\mathrm{EH}}_{\tilde{m}_z} = \bar{J}_m \bar{J}_{\tilde{m}} \\
&e^{\mathrm{EH}^*}_{m_r} e^{\mathrm{EH}}_{\tilde{m}_r} + e^{\mathrm{EH}^*}_{m_\phi} e^{\mathrm{EH}}_{\tilde{m}_\phi} + e^{\mathrm{EH}^*}_{m_z} e^{\mathrm{EH}}_{\tilde{m}_z} \\
&\quad = \frac{2\beta\tilde{\beta}}{u^2\tilde{u}^2}\left[\frac{m\tilde{m}}{r^2}\bar{J}_m\bar{J}_{\tilde{m}} + u\tilde{u}\bar{J}'_m\bar{J}'_{\tilde{m}} - \frac{1}{r}\left(m\tilde{u}\bar{J}_m\bar{J}'_{\tilde{m}} + \tilde{m}u\bar{J}_{\tilde{m}}\bar{J}'_m\right)\right] + \bar{J}_m\bar{J}_{\tilde{m}}.
\end{aligned}
\tag{C.6}
$$

As a result, the overlap integrals in Eq. (C.4) are for the strongly coupled, even polarised output modes:

$$
\begin{aligned}
&\langle \mathbf{HE}^{(\mathrm{e})}_m | e^{-im_g\phi}\,\Theta(a-r) | \mathbf{HE}^{(\mathrm{e})}_{\tilde{m}=\pm m_g+m} \rangle \\
&= \frac{\pi}{2}\int_0^a dr\, r \left(\frac{2\beta\tilde{\beta}}{u^2\tilde{u}^2}\left[\frac{m\tilde{m}}{r^2}\bar{J}_m\bar{J}_{\tilde{m}} + u\tilde{u}\bar{J}'_m\bar{J}'_{\tilde{m}} + \frac{1}{r}\left(m\tilde{u}\bar{J}_m\bar{J}'_{\tilde{m}} + \tilde{m}u\bar{J}_{\tilde{m}}\bar{J}'_m\right)\right] + \bar{J}_m\bar{J}_{\tilde{m}}\right), \\
&\langle \mathbf{HE}^{(\mathrm{e})}_m | e^{-im_g\phi}\,\Theta(a-r) | \mathbf{EH}^{(\mathrm{e})}_{\tilde{m}=\pm m_g-m} \rangle \\
&= \frac{\pi}{2}\int_0^a dr\, r \left(\frac{-2\beta\tilde{\beta}}{u^2\tilde{u}^2}\left[\frac{m\tilde{m}}{r^2}\bar{J}_m\bar{J}_{\tilde{m}} + u\tilde{u}\bar{J}'_m\bar{J}'_{\tilde{m}} - \frac{1}{r}\left(m\tilde{u}\bar{J}_m\bar{J}'_{\tilde{m}} + \tilde{m}u\bar{J}_{\tilde{m}}\bar{J}'_m\right)\right] + \bar{J}_m\bar{J}_{\tilde{m}}\right).
\end{aligned}
\tag{C.7}
$$

In the case of the weakly coupled modes, the radial and azimuthal components of the hybrid modes annul each other and only the longitudinal components are left:

$$\begin{aligned}\langle \mathbf{HE}^{(e)}_{m}|e^{-im_g\phi}\,\Theta(a-r)|\mathbf{HE}^{(e)}_{\tilde{m}=\pm m_g-m}\rangle &= \frac{\pi}{2}\int_0^a dr\, r\, \bar{J}_m \bar{J}_{\tilde{m}},\\ \langle \mathbf{HE}^{(e)}_{m}|e^{-im_g\phi}\,\Theta(a-r)|\mathbf{EH}^{(e)}_{\tilde{m}=\pm m_g+m}\rangle &= \frac{\pi}{2}\int_0^a dr\, r\, \bar{J}_m \bar{J}_{\tilde{m}}.\end{aligned} \tag{C.8}$$

If the output modes are odd polarised, the overlap integrals are the same except for a phase:

$$\begin{aligned}\langle \mathbf{HE}^{(e)}_{m}|e^{-im_g\phi}\,\Theta(a-r)|\mathbf{HE}^{(o)}_{\tilde{m}=\pm m_g+m}\rangle &= -i\,\langle \mathbf{HE}^{(e)}_{m}|e^{-im_g\phi}\,\Theta(a-r)|\mathbf{HE}^{(e)}_{\tilde{m}=\pm m_g+m}\rangle\,,\\ \langle \mathbf{HE}^{(e)}_{m}|e^{-im_g\phi}\,\Theta(a-r)|\mathbf{EH}^{(o)}_{\tilde{m}=\pm m_g-m}\rangle &= -i\,\langle \mathbf{HE}^{(e)}_{m}|e^{-im_g\phi}\,\Theta(a-r)|\mathbf{EH}^{(e)}_{\tilde{m}=\pm m_g-m}\rangle\,,\\ \langle \mathbf{HE}^{(e)}_{m}|e^{-im_g\phi}\,\Theta(a-r)|\mathbf{HE}^{(o)}_{\tilde{m}=\pm m_g-m}\rangle &= \mp i\,\langle \mathbf{HE}^{(e)}_{m}|e^{-im_g\phi}\,\Theta(a-r)|\mathbf{EH}^{(e)}_{\tilde{m}=\pm m_g-m}\rangle\,,\\ \langle \mathbf{HE}^{(e)}_{m}|e^{-im_g\phi}\,\Theta(a-r)|\mathbf{EH}^{(o)}_{\tilde{m}=\pm m_g+m}\rangle &= \mp i\,\langle \mathbf{HE}^{(e)}_{m}|e^{-im_g\phi}\,\Theta(a-r)|\mathbf{HE}^{(e)}_{\tilde{m}=\pm m_g+m}\rangle\,,\end{aligned} \tag{C.9}$$

see Eq. (C.4). The integrals for OAM modes are twice the coupling integrals with the corresponding basis hybrid-modes as output mode-profiles:

$$\begin{aligned}\langle \mathbf{HE}^{(e)}_{m}|e^{-im_g\phi}\,\Theta(a-r)|\mathbf{O}^{+}_{+\tilde{m}=m_g\pm m}\rangle &= 2\,\langle \mathbf{HE}^{(e)}_{m}|e^{-im_g\phi}\,\Theta(a-r)|\mathbf{HE}^{(e)}_{\tilde{m}=m_g\pm m+1}\rangle\,,\\ \langle \mathbf{HE}^{(e)}_{m}|e^{-im_g\phi}\,\Theta(a-r)|\mathbf{O}^{-}_{+\tilde{m}=m_g\pm m}\rangle &= 2\,\langle \mathbf{HE}^{(e)}_{m}|e^{-im_g\phi}\,\Theta(a-r)|\mathbf{EH}^{(e)}_{\tilde{m}=m_g\pm m-1}\rangle\,,\\ \langle \mathbf{HE}^{(e)}_{m}|e^{-im_g\phi}\,\Theta(a-r)|\mathbf{O}^{+}_{-\tilde{m}=-(-m_g\pm m)}\rangle &= 2\,\langle \mathbf{HE}^{(e)}_{m}|e^{-im_g\phi}\,\Theta(a-r)|\mathbf{EH}^{(e)}_{\tilde{m}=-m_g\pm m-1}\rangle\,,\\ \langle \mathbf{HE}^{(e)}_{m}|e^{-im_g\phi}\,\Theta(a-r)|\mathbf{O}^{-}_{-\tilde{m}=-(-m_g\pm m)}\rangle &= 2\,\langle \mathbf{HE}^{(e)}_{m}|e^{-im_g\phi}\,\Theta(a-r)|\mathbf{HE}^{(e)}_{\tilde{m}=-m_g\pm m+1}\rangle\,.\end{aligned} \tag{C.10}$$

The same holds for the circularly polarised modes:

$$\begin{aligned}\langle \mathbf{HE}^{(e)}_{m=m_g\pm 1}|e^{-im_g\phi}\,\Theta(a-r)|\mathbf{\Sigma}^{+}\rangle &= 2\,\langle \mathbf{HE}^{(e)}_{m=m_g\pm 1}|e^{-im_g\phi}\,\Theta(a-r)|\mathbf{HE}^{(e)}_{1}\rangle\,,\\ \langle \mathbf{HE}^{(e)}_{m=-m_g\pm 1}|e^{-im_g\phi}\,\Theta(a-r)|\mathbf{\Sigma}^{-}\rangle &= 2\,\langle \mathbf{HE}^{(e)}_{m=m_g\pm 1}|e^{-im_g\phi}\,\Theta(a-r)|\mathbf{HE}^{(e)}_{1}\rangle\,.\end{aligned} \tag{C.11}$$

C.2 Normalisation

The transverse modes $\mathbf{f}(r,\phi) \in \{\, \mathbf{HE}_m^{(\mathrm{e/o})},\ \mathbf{EH}_m^{(\mathrm{e/o})},\ \mathbf{O}_{\pm m}^{\pm},\ \mathbf{O}_{\pm m}^{\mp},\ \mathbf{\Sigma}^{\pm} \,\}$ are i.a. normalised by

$$\langle \mathbf{f}(r,\phi)|\bar{\varepsilon}(r)|\mathbf{f}(r,\phi)\rangle = \int_0^\infty dr\ r\ \bar{\varepsilon}(r) \int_0^{2\pi} d\phi\ \left|\mathbf{f}(r,\phi)\right|^2, \tag{C.12}$$

where the mean dielectric constant $\bar{\varepsilon}(r)$ is the squared mean refractive index in the core or the cladding of the waveguide, see Eq. (2.2). The two integrals in Eq. (C.12) can be calculated one after another by using the mode separations in Eqs. (2.15), (2.19) and (2.20). As shown in App. C.1, the integral over the azimuthal angle ϕ is solved analytically while the integral over radius r is left for numerical calculations. The integrals for even and odd polarised hybrid modes $\mathrm{M} \in \{\, \mathrm{HE},\, \mathrm{EH} \,\}$ are equal according to

$$\begin{aligned}
&\langle \mathbf{M}_m^{(\mathrm{e})}|\bar{\varepsilon}(r)|\mathbf{M}_m^{(\mathrm{e})}\rangle \\
&\quad= \left[\int_0^\infty dr\, r\, \bar{\varepsilon}(r) \begin{pmatrix} \left|e_{m_r}^{\mathrm{M}}(r)\right|^2 \\ \left|e_{m_\phi}^{\mathrm{M}}(r)\right|^2 \\ \left|e_{m_z}^{\mathrm{M}}(r)\right|^2 \end{pmatrix}\right]^T \cdot \left[\int_0^{2\pi} d\phi \begin{pmatrix} \cos^2(m\phi) \\ \sin^2(m\phi) \\ \cos^2(m\phi) \end{pmatrix}\right] = \pi \int_0^\infty dr\, r\, \bar{\varepsilon}(r)\ \left|\mathbf{e}_m^{\mathrm{M}}(r)\right|^2, \\
&\langle \mathbf{M}_m^{(\mathrm{o})}|\bar{\varepsilon}(r)|\mathbf{M}_m^{(\mathrm{o})}\rangle \\
&\quad= \left[\int_0^\infty dr\, r\, \bar{\varepsilon}(r) \begin{pmatrix} \left|e_{m_r}^{\mathrm{M}}(r)\right|^2 \\ \left|e_{m_\phi}^{\mathrm{M}}(r)\right|^2 \\ \left|e_{m_z}^{\mathrm{M}}(r)\right|^2 \end{pmatrix}\right]^T \cdot \left[\int_0^{2\pi} d\phi \begin{pmatrix} \sin^2(m\phi) \\ \cos^2(m\phi) \\ \sin^2(m\phi) \end{pmatrix}\right] = \pi \int_0^\infty dr\, r\, \bar{\varepsilon}(r)\ \left|\mathbf{e}_m^{\mathrm{M}}(r)\right|^2,
\end{aligned} \tag{C.13}$$

where $m \geq 1$. The integrals for OAM modes and circularly polarised modes are analogously:

$$\begin{aligned}
\langle \mathbf{O}_{\pm m}^{\pm}|\bar{\varepsilon}(r)|\mathbf{O}_{\pm m}^{\pm}\rangle &= 2\pi \int_0^\infty dr\, r\, \bar{\varepsilon}(r)\ \left|\mathbf{e}_{m+1}^{\mathrm{HE}}(r)\right|^2 \ \text{, for } m \geq 1, \\
\langle \mathbf{O}_{\pm m}^{\mp}|\bar{\varepsilon}(r)|\mathbf{O}_{\pm m}^{\mp}\rangle &= 2\pi \int_0^\infty dr\, r\, \bar{\varepsilon}(r)\ \left|\mathbf{e}_{m-1}^{\mathrm{EH}}(r)\right|^2 \ \text{, for } m \geq 2, \\
\langle \mathbf{\Sigma}^{\pm}|\bar{\varepsilon}(r)|\mathbf{\Sigma}^{\pm}\rangle &= 2\pi \int_0^\infty dr\, r\, \bar{\varepsilon}(r)\ \left|\mathbf{e}_1^{\mathrm{HE}}(r)\right|^2.
\end{aligned} \tag{C.14a}$$

They can be rewritten in terms of the hybrid-mode integrals in Eq. (C.13):

$$\begin{aligned}
\langle \mathbf{O}_{\pm m}^{\pm}|\bar{\varepsilon}(r)|\mathbf{O}_{\pm m}^{\pm}\rangle &= 2\,\langle \mathbf{HE}_{m+1}^{(\mathrm{e})}|\bar{\varepsilon}(r)|\mathbf{HE}_{m+1}^{(\mathrm{e})}\rangle \ \text{, for } m \geq 1, \\
\langle \mathbf{O}_{\pm m}^{\mp}|\bar{\varepsilon}(r)|\mathbf{O}_{\pm m}^{\mp}\rangle &= 2\,\langle \mathbf{EH}_{m-1}^{(\mathrm{e})}|\bar{\varepsilon}(r)|\mathbf{EH}_{m-1}^{(\mathrm{e})}\rangle \ \text{, for } m \geq 2, \\
\langle \mathbf{\Sigma}^{\pm}|\bar{\varepsilon}(r)|\mathbf{\Sigma}^{\pm}\rangle &= 2\,\langle \mathbf{HE}_1^{(\mathrm{e})}|\bar{\varepsilon}(r)|\mathbf{HE}_1^{(\mathrm{e})}\rangle.
\end{aligned} \tag{C.14b}$$

Other integrals that are necessary for the normalisation,

$$\langle \mathbf{f}(r,\phi)|\mathbf{f}(r,\phi)\rangle = \int_0^\infty dr\ r \int_0^{2\pi} d\phi\ \left|\mathbf{f}(r,\phi)\right|^2, \tag{C.15}$$

lead to the same expressions without $\bar{\varepsilon}(r)$.

C.3 Connections between coupled modes

Concluding, the change of the coupling constants is derived for different strongly coupled modes. Considering the coupling between an $\mathbf{HE}_1^{(\mathrm{e})}$ and an $\mathbf{O}_{+m_g}^{+}$ mode profile that is:

$$\begin{aligned}
&\kappa_1\Big(\mathbf{HE}_1^{(\mathrm{e})} \to \mathbf{O}_{+m_g}^{+}\Big) \\
&= \frac{\Delta\varepsilon_0\,\omega^2}{4\beta_1 c^2}\sqrt{\frac{\langle \mathbf{HE}_1^{(\mathrm{e})}|\bar{\varepsilon}(r)|\mathbf{HE}_1^{(\mathrm{e})}\rangle}{\langle \mathbf{O}_{+m_g}^{+}|\bar{\varepsilon}(r)|\mathbf{O}_{+m_g}^{+}\rangle}}\,\frac{\langle \mathbf{HE}_1^{(\mathrm{e})}|e^{-im_g\phi}\,\Theta(a-r)|\mathbf{O}_{+m_g}^{+}\rangle}{\langle \mathbf{HE}_1^{(\mathrm{e})}|\mathbf{HE}_1^{(\mathrm{e})}\rangle} \\
&= \frac{\Delta\varepsilon_0\,\omega^2}{4\beta_1 c^2}\sqrt{\frac{\langle \mathbf{HE}_1^{(\mathrm{e})}|\bar{\varepsilon}(r)|\mathbf{HE}_1^{(\mathrm{e})}\rangle}{2\,\langle \mathbf{HE}_{m_g+1}^{(\mathrm{e})}|\bar{\varepsilon}(r)|\mathbf{HE}_{m_g+1}^{(\mathrm{e})}\rangle}}\,\frac{2\,\langle \mathbf{HE}_1^{(\mathrm{e})}|e^{-im_g\phi}\,\Theta(a-r)|\mathbf{HE}_{m_g+1}^{(\mathrm{e})}\rangle}{\langle \mathbf{HE}_1^{(\mathrm{e})}|\mathbf{HE}_1^{(\mathrm{e})}\rangle} \\
&= \sqrt{2}\,\kappa_1\Big(\mathbf{HE}_1^{(\mathrm{e})} \to \mathbf{HE}_{m_g+1}^{(\mathrm{e})}\Big)\,,
\end{aligned} \tag{C.16}$$

where $m_g \geq 1$. In the first step, the definition of κ_1 in Eq. (3.16a) is applied. In the second step, Eqs. (C.10) and (C.14b) are used. In the last step, the definition of $\kappa_1\Big(\mathbf{HE}_1^{(\mathrm{e})} \to \mathbf{HE}_{m_g+1}^{(\mathrm{e})}\Big)$ is identified. The derivation can be generalised to all other modes that differ by a $\frac{\pi}{2}$-phase shift. The coupling to circularly polarised OAM modes is therefore increased by a factor of $\sqrt{2}$.

An exception is the case of $m_g = 0$ where the self-coupling constant is a factor of $\sqrt{2}$ larger than κ_1 for the circularly polarised modes $\mathbf{\Sigma}^{+}$ and $\mathbf{\Sigma}^{-}$. The proof is as follows:

$$\begin{aligned}
&\kappa_1\Big(\mathbf{HE}_1^{(\mathrm{e})} \to \mathbf{HE}_1^{(\mathrm{e})}\Big) \\
&= \kappa_1\left(\mathbf{HE}_1^{(\mathrm{e})} \to \frac{1}{2}\left(\mathbf{\Sigma}^{+} + \mathbf{\Sigma}^{-}\right)\right) \\
&= \frac{\Delta\varepsilon_0\,\omega^2}{4\beta_1 c^2}\sqrt{\frac{\langle \mathbf{HE}_1^{(\mathrm{e})}|\bar{\varepsilon}(r)|\mathbf{HE}_1^{(\mathrm{e})}\rangle}{\langle \frac{1}{2}\left(\mathbf{\Sigma}^{+} + \mathbf{\Sigma}^{-}\right)|\bar{\varepsilon}(r)|\frac{1}{2}\left(\mathbf{\Sigma}^{+} + \mathbf{\Sigma}^{-}\right)\rangle}}\,\frac{\langle \mathbf{HE}_1^{(\mathrm{e})}|\Theta(a-r)|\frac{1}{2}\left(\mathbf{\Sigma}^{+} + \mathbf{\Sigma}^{-}\right)\rangle}{\langle \mathbf{HE}_1^{(\mathrm{e})}|\mathbf{HE}_1^{(\mathrm{e})}\rangle} \\
&= \frac{\Delta\varepsilon_0\,\omega^2}{4\beta_1 c^2}\sqrt{\frac{\langle \mathbf{HE}_1^{(\mathrm{e})}|\bar{\varepsilon}(r)|\mathbf{HE}_1^{(\mathrm{e})}\rangle}{\frac{2}{4}\,\langle \mathbf{\Sigma}^{\pm}|\bar{\varepsilon}(r)|\mathbf{\Sigma}^{\pm}\rangle}}\,\frac{\langle \mathbf{HE}_1^{(\mathrm{e})}|\Theta(a-r)|\mathbf{\Sigma}^{\pm}\rangle}{\langle \mathbf{HE}_1^{(\mathrm{e})}|\mathbf{HE}_1^{(\mathrm{e})}\rangle} \\
&= \sqrt{2}\,\kappa_1\Big(\mathbf{HE}_1^{(\mathrm{e})} \to \mathbf{\Sigma}^{\pm}\Big)\,,
\end{aligned} \tag{C.17}$$

where

$$\begin{aligned}
\langle \mathbf{HE}_1^{(\mathrm{e})}|\Theta(a-r)|\mathbf{\Sigma}^{+}\rangle &= \langle \mathbf{HE}_1^{(\mathrm{e})}|\Theta(a-r)|\mathbf{\Sigma}^{-}\rangle\,, \\
\langle \mathbf{\Sigma}^{+}|\bar{\varepsilon}(r)|\mathbf{\Sigma}^{+}\rangle &= \langle \mathbf{\Sigma}^{-}|\bar{\varepsilon}(r)|\mathbf{\Sigma}^{-}\rangle\,, \\
\langle \mathbf{\Sigma}^{+}|\bar{\varepsilon}(r)|\mathbf{\Sigma}^{-}\rangle &= \langle \mathbf{\Sigma}^{-}|\bar{\varepsilon}(r)|\mathbf{\Sigma}^{+}\rangle = 0
\end{aligned} \tag{C.18}$$

are applied in the third step of Eq. (C.17).

Bibliography

[1] M. Erhard, R. Fickler, M. Krenn, and A. Zeilinger, "Twisted photons: new quantum perspectives in high dimensions," *Light: Science & Applications*, vol. 7, p. 17146, Mar 2018.

[2] W. Zhang, D.-S. Ding, Y.-B. Sheng, L. Zhou, B.-S. Shi, and G.-C. Guo, "Quantum secure direct communication with quantum memory," *Phys. Rev. Lett.*, vol. 118, p. 220501, May 2017.

[3] J. G. Rarity, P. M. Gorman, K. W. Paul Knight, and P. R. Tapster, "Quantum cryptography to satellites for global secure key distribution," *Proc. SPIE*, vol. 10569, p. 105690W 8, Nov 2017.

[4] J.-G. Ren, P. Xu, H.-L. Yong, L. Zhang, S.-K. Liao, J. Yin, W.-Y. Liu, W.-Q. Cai, M. Yang, L. Li, K.-X. Yang, X. Han, Y.-Q. Yao, J. Li, H.-Y. Wu, S. Wan, L. Liu, D.-Q. Liu, Y.-W. Kuang, Z.-P. He, P. Shang, C. Guo, R.-H. Zheng, K. Tian, Z.-C. Zhu, N.-L. Liu, C.-Y. Lu, R. Shu, Y.-A. Chen, C.-Z. Peng, J.-Y. Wang, and J.-W. Pan, "Ground-to-satellite quantum teleportation," *Nature*, vol. 549, p. 70, Aug 2017.

[5] T. M. Graham, H. J. Bernstein, T.-C. Wei, M. Junge, and P. G. Kwiat, "Superdense teleportation using hyperentangled photons," *Nature Comm.*, vol. 6, p. 7185, May 2015.

[6] G.-Y. Wang, T. Li, Q. Ai, and F.-G. Deng, "Self-error-corrected hyperparallel photonic quantum computation working with both the polarization and the spatial-mode degrees of freedom," *Opt. Express*, vol. 26, pp. 23333–23346, Sep 2018.

[7] J. Romero and M. Padgett, "Practical bound for dimensionality in high-dimensional entanglement," *Proceedings of the National Academy of Sciences*, vol. 111, pp. 6122–6123, Apr 2014.

[8] W. K. Wootters and W. H. Zurek, "A single quantum cannot be cloned," *Nature*, vol. 299, p. 802, Oct 1982.

[9] H. Bechmann-Pasquinucci and W. Tittel, "Quantum cryptography using larger alphabets," *Phys. Rev. A*, vol. 61, p. 062308, May 2000.

[10] N. J. Cerf, M. Bourennane, A. Karlsson, and N. Gisin, "Security of quantum key distribution using d-level systems," *Phys. Rev. Lett.*, vol. 88, p. 127902, Mar 2002.

[11] E. Campbell, H. Anwar, and D. Browne, "Magic-state distillation in all prime dimensions using quantum reed-muller codes," *Phys. Rev. X*, vol. 2, p. 041021, May 2012.

[12] J. O'Gorman and E. T. Campbell, "Quantum computation with realistic magic-state factories," *Phys. Rev. A*, vol. 95, p. 032338, Mar 2017.

[13] A. Bocharov, M. Roetteler, and K. M. Svore, "Factoring with qutrits: Shor's algorithm on ternary and metaplectic quantum architectures," *Phys. Rev. A*, vol. 96, p. 012306, Jul 2017.

[14] A. Mair, A. Vaziri, G. Weihs, and A. Zeilinger, "Entanglement of the orbital angular momentum states of photons," *Nature*, vol. 412, pp. 313–316, Jul 2001.

[15] A. E. Willner, "Communication with a twist," *IEEE Spectrum*, vol. 53, pp. 34–39, Aug 2016.

[16] Y. Zhang, M. Agnew, T. Roger, F. S. Roux, T. Konrad, D. Faccio, J. Leach, and A. Forbes, "Simultaneous entanglement swapping of multiple orbital angular momentum states of light," *Nature Comm.*, vol. 8, p. 632, Sep 2017.

[17] M. Krenn, A. Hochrainer, M. Lahiri, and A. Zeilinger, "Entanglement by path identity," *Phys. Rev. Lett.*, vol. 118, p. 080401, Feb 2017.

[18] R. Fickler, R. Lapkiewicz, M. Huber, M. P. J. Lavery, M. J. Padgett, and A. Zeilinger, "Interface between path and orbital angular momentum entanglement for high-dimensional photonic quantum information," *Nature Comm.*, vol. 5, p. 4502, Jul 2014.

[19] S. Chen and J. Wang, "Theoretical analyses on orbital angular momentum modes in conventional graded-index multimode fibre," *Scientific Reports*, vol. 7, p. 3990, Jun 2017.

[20] N. Zhao, X. Li, G. Li, and J. M. Kahn, "Capacity limits of spatially multiplexed free-space communication," *Nature Photonics*, vol. 9, p. 822, Nov 2015.

[21] R. Noé, *Essentials of Modern Optical Fiber Communication*. Springer-Verlag Berlin Heidelberg, 2010.

[22] A. W. Snyder and W. R. Young, "Modes of optical waveguides," *J. Opt. Soc. Am.*, vol. 68, pp. 297–309, Mar 1978.

[23] A. W. Snyder and J. D. Love, *Optical waveguide theory*, ch. 12, pp. 239–249. Science paperbacks, London [u.a.] : Chapman and Hall, 1983.

[24] G. H. Owyang, *Foundations of optical waveguides*, ch. 2. Elsevier North Holland, Inc., Jun 1981.

[25] M. Koshiba, *Optical Waveguide Analysis*. New York [u.a]: McGraw-Hill, Inc., 1992.

[26] K. Okamoto, *Fundamentals of Optical Waveguides*, ch. 3, pp. 63–68. Amsterdam [u.a.]: Elsevier, 2nd ed., 2006.

[27] M. Steel, *Theory of Waveguide Optics and Coupled Mode Analysis*. Lecture notes, unpublished, Oct 2017.

[28] S. Ramachandran and P. Kristensen, "Optical vortices in fiber," *Nanophotonics*, vol. 2, pp. 455–474, Dec 2013.

[29] Y. Ma, J. Xu, H. Gao, and X. Xiong, "Intensity profile stabilities of high order vectorial modes of optical fibers," *Optik - International Journal for Light and Electron Optics*, vol. 149, pp. 277–287, Aug 2017.

[30] J. Xin, K. Dai, L. Zhong, Q. Na, and C. Gao, "Generation of optical vortices by using spiral phase plates made of polarization dependent devices," *Opt. Lett.*, vol. 39, pp. 1984–1987, Apr 2014.

[31] J. Arlt, K. Dholakia, L. Allen, and M. J. Padgett, "The production of multiringed laguerre–gaussian modes by computer-generated holograms," *Journal of Modern Optics*, vol. 45, pp. 1231–1237, Sep 1998.

[32] G. Ruffato, M. Girardi, M. Massari, E. Mafakheri, B. Sephton, P. Capaldo, A. Forbes, and F. Romanato, "A compact diffractive sorter for high-resolution demultiplexing of orbital angular momentum beams," *Scientific Reports*, vol. 8, p. 10248, Jul 2018.

[33] C. Brunet and L. A. Rusch, "Optical fibers for the transmission of orbital angular momentum modes," *Optical Fiber Technology*, vol. 35, pp. 2–7, Feb 2017.

[34] "Orbital angular momentum of light." *wikipedia.org*. Picture of OAM phase fronts. Accessed: 1st Aug 2018.

[35] D. J. Thouless, *Topological Quantum Numbers in Nonrelativistic Physics*. World Scientific, Mar 1998.

[36] P. Z. Dashti, F. Alhassen, and H. Lee, "Observation of orbital angular momentum transfer between acoustic and optical vortices in optical fiber," *Phys. Rev. Lett.*, vol. 96, p. 043604, Feb 2006.

[37] A. Y. Okulov, "Angular momentum of photons and phase conjugation," *Journal of Physics B: Atomic, Molecular and Optical Physics*, vol. 41, p. 101001, May 2008.

[38] T. B. Simpson and J. Liu, "Waveguide four-wave mixing," *Jayor San Diego, CA 92186-5154*, vol. 59, pp. 7–14, Oct 1991.

[39] Z. Xiong, W. Chen, P. Wang, and Y. Chen, "Classification of symmetry properties of waveguide modes in presence of gain/losses, anisotropy/bianisotropy, or continuous/discrete rotational symmetry," *Opt. Express*, vol. 25, pp. 29822–29834, Nov 2017.

[40] L. Wang, P. Vaity, B. Ung, Y. Messaddeq, L. A. Rusch, and S. LaRochelle, "Characterization of oam fibers using fiber bragg gratings," *Opt. Express*, vol. 22, pp. 15653–15661, Jun 2014.

[41] I. Petermann, B. Sahlgren, S. Helmfrid, A. T. Friberg, and P.-Y. Fonjallaz, "Fabrication of advanced fiber bragg gratings by use of sequential writing with a continuous-wave ultraviolet laser source," *Appl. Opt.*, vol. 41, pp. 1051–1056, Feb 2002.

[42] T. Erdogan, "Fiber grating spectra," *Journal of Lightwave Technology*, vol. 15, pp. 1277–1294, Aug 1997.

[43] E. Meyer-Scott, N. Montaut, J. Tiedau, L. Sansoni, H. Herrmann, T. J. Bartley, and C. Silberhorn, "Limits on the heralding efficiencies and spectral purities of spectrally filtered single photons from photon-pair sources," *Phys. Rev. A*, vol. 95, p. 061803, Jun 2017.

[44] T. Schneider, *Four-Wave-Mixing*, pp. 167–200. Berlin, Heidelberg: Springer Berlin Heidelberg, 2004.

[45] I. Jizan, B. Bell, L. G. Helt, A. C. Bedoya, C. Xiong, and B. J. Eggleton, "Phase-sensitive tomography of the joint spectral amplitude of photon pair sources," *Opt. Lett.*, vol. 41, pp. 4803–4806, Oct 2016.

[46] S. Ramachandran, P. Kristensen, and M. F. Yan, "Generation and propagation of radially polarized beams in optical fibers," *Opt. Lett.*, vol. 34, pp. 2525–2527, Aug 2009.

[47] G. D. Marshall, R. J. Williams, N. Jovanovic, M. J. Steel, and M. J. Withford, "Point-by-point written fiber-bragg gratings and their application in complex grating designs," *Opt. Express*, vol. 18, pp. 19844–19859, Sep 2010.

[48] J. Ni, C. Wang, C. Zhang, Y. Hu, L. Yang, Z. Lao, B. Xu, J. Li, D. Wu, and J. Chu, "Three-dimensional chiral microstructures fabricated by structured optical vortices in isotropic material," *Light: Science & Applications*, vol. 6, p. 17011, Jul 2017.

[49] C. Jiang, Y. Liu, Y. Zhao, L. Zhang, C. Mou, and T. Wang, "Helical long-period fiber grating written in polarization-maintaining fiber by co2-laser," in *Conference on Lasers and Electro-Optics*, p. SM2K.2, Optical Society of America, May 2018.

[50] X. Wang, D. Wang, Q. Wang, L. Xian, and L. Li, "Fabrication and characterization of helical long-period fiber gratings in single-mode fibers," *Optics*, vol. 158, pp. 28–32, Apr 2018.

[51] H. A. Haus and W. Huang, "Coupled-mode theory," *Proceedings of the IEEE*, vol. 79, pp. 1505–1518, Oct 1991.

[52] R. Hunsperger, *Integrated Optics: Theory and Technology*, ch. 8.2.2, pp. 157–160. New York: Springer Science + Business Media, 6th ed., Mar 2009.

[53] K. Heshami, D. G. England, P. C. Humphreys, P. J. Bustard, V. M. Acosta, J. Nunn, and B. J. Sussman, "Quantum memories: emerging applications and recent advances," *Journal of Modern Optics*, vol. 63, pp. 2005–2028, Nov 2016.

[54] A. Christ, B. Brecht, W. Mauerer, and C. Silberhorn, "Theory of quantum frequency conversion and type-ii parametric down-conversion in the high-gain regime," *New Journal of Physics*, vol. 15, p. 053038, May 2013.

[55] R. W. Boyd, *Nonlinear Optics*. Orlando, FL, USA: Academic Press, Inc., 3rd ed., Mar 2008.

[56] L. Fang and J. Wang, "Flexible generation/conversion/exchange of fiber-guided orbital angular momentum modes using helical gratings," *Opt. Lett.*, vol. 40, pp. 4010–4013, Sep 2015.

[57] C. N. Alexeyev, B. P. Lapin, and M. A. Yavorsky, "Helical core optical fibers maintaining propagation of a solitary optical vortex," *Phys. Rev. A*, vol. 78, p. 013813, Jul 2008.

Acknowledgements

I am extremely grateful to the grant organisers for making the research stay in Sydney possible - because of you I was having an unforgettable time in Australia full of wonderful experiences!

My biggest thanks go to my first supervisor J.-Prof. Polina Sharapova for her great effort to make the best out of the thesis. I appreciate her kind care and numerous long discussions out of which many derivations have grown. I am also very grateful to Prof. Torsten Meier for the second correction of my thesis, his active encouragements for the organisation of the research exchange and his helpful assistance before as well as after my stay abroad.

Special acknowledgements are due to my supervisor at the Macquarie University in Sydney, Prof. Michael Steel, for finding time for many valuable discussions, fruitful skype sessions and his warm-hearted care. Equally, I thank Mikolaj, my second supervisor in Australia: Thanks for your patient, illustrative and kind manner in explaining physics. You and your smiling face have been a great support during and after my time in Australia.

Looking back, I got to know a lot of people at the Macquarie University in Sydney. Your close community has supported me personally from my first day and I am very grateful for having been a part of it.

Moreover, I acknowledge my valued office mates in Paderborn, Wolf and Alessandro, for the big and numerous help with my thesis. You have been a nice company by having relaxing conversations about all kinds of topics.

Outside the physics department I am sincerely grateful to my family for caring and pushing me in every conceivable situation.

Thanks to all of you!

Declaration

(Translation from German)

I hereby declare that I prepared this thesis entirely on my own and have not used outside sources without declaration in the text. Any concepts or quotations applicable to these sources are clearly attributed to them. This thesis has not been submitted in the same or substantially similar version, not even in part, to any other authority for grading and has not been published elsewhere.

Original Declaration Text in German:

Erklärung

Ich versichere, dass ich die Arbeit ohne fremde Hilfe und ohne Benutzung anderer als der angegebenen Quellen angefertigt habe und dass die Arbeit in gleicher oder ähnlicher Form noch keiner anderen Prüfungsbehörde vorgelegen hat und von dieser als Teil einer Prüfungsleistung angenommen worden ist. Alle Ausführungen, die wörtlich oder sinngemäß übernommen worden sind, sind als solche gekennzeichnet.

City, Date

Signature